BILIARY TRACT DIFFERENTIATION THROUGH USE OF VISIBLE TO NIR HYPERSPECTRAL REFLECTANCE IMAGING

by

ELEANOR F WEHNER

Presented to the Faculty of the Graduate School of

The University of Texas at Arlington in Partial Fulfillment

of the Requirements

for the Degree of

DOCTOR OF PHILOSOPHY

THE UNIVERSITY OF TEXAS AT ARLINGTON

August 2014

Acknowledgements

I would like to acknowledge the many people who made this dissertation possible. In particular, I would like to thank my former mentors Dr. Karel Zuzak and Dr. Edward Livingston for introducing me to hyperspectral imaging and the problem of anatomical differentiation of the common bile duct, respectively. I would also like to thank Dr. Georgios Alexandrakis for graciously taking over my mentorship, even though my project area was not within his area of expertise.

Funding sources for my research include an allotment from the Department of Energy, a grant from Texas Instruments (TI), the National Institute for Standards and Technology (NIST) and the UTA Bioengineering Department.

I am grateful as well to the many people who made data collection possible. Drs. John Mansour, Roderich Schwarz and Edward Livingston for identifying possible common bile duct data collection schemes, and the ever-cooperative Urologists with whom I've co-authored many papers: Drs. Jeffrey Cadeddu, Sarah Best, Chad Tracy, and Ephrem Olweny. I would like to thank the HSI technicians without whom extensive data collection would have not been possible: Van Jackson and Neil Jackson, and my other student colleagues, Robert Francis, Abhas Thapa, Swetha Suresh, and Michael Mangum.

I would also like to thank my fantastic committee members I have not already mentioned, whose feedback on this project has been invaluable: Drs. Hanli Liu and Digant Dave, and a special thanks to Dr. Baohong Yuan for agreeing to be on my committee on short notice.

Finally, I would like to thank Sandra Hackemann and James Wehner, my parents who have always been supportive of my academic pursuits.

August 4, 2014

Abstract

BILIARY TRACT DIFFERENTIATION THROUGH USE OF VISIBLE TO NIR HYPERSPECTRAL REFLECTANCE IMAGING

Eleanor Wehner, PhD

The University of Texas at Arlington, 2014

Supervising Professor: Georgios Alexandrakis

Cholecystectomies are one of the most common surgeries performed in the United States, and most of the complications which arise from these are injuries to the common bile duct (CBD) resulting from a misidentification of anatomy. Reflectance hyperspectral imaging (HSI) offers a low-cost, non-invasive tool to record superficial chemical spectra of a field of view in many surgical applications.

A NIR DLP HSI system is assembled and characterized, and used to gather preliminary CBD reflectance HSI data cubes. NIR hyperspectral imaging (760 nm to 1600 nm) with the DLP HSI system proves ineffectual, so CBD reflectance hyperspectral data collection progresses with the previously characterized visible DLP HSI system (380 nm to 780 nm). 13 human subjects are imaged with the visible DLP HSI system in open surgery. An average spectrum for the CBD is calculated and examined for its usefulness as a spectrum to detect the human CBD in the 13 image scenes.

In order to select hyperspectral analysis techniques to assist in the location of the *in vivo* human CBD, an extensive review of existing hyperspectral analysis literature is performed. 18 out of 51 researched methods are selected for evaluation, and 4 detect the CBD successfully.

The calculation of average tissue spectra is extended beyond the CBD to other tissues previously imaged with the visible DLP HSI system, in order to create a tissue spectral database.

Tissues additionally characterized in this manner include human fat, kidney, gallbladder, liver, renal cyst, and pig kidney. These 5 tissue types, in addition to human CBD are compared statistically to each other with two different metrics: spectral angle distance, which compares two entire spectra at once, and t-tests performed in a wavelength-by-wavelength grouping. These two techniques both agree that the most similar tissue spectra to each other include oxygenated kidney and renal cyst tissue, and human and pig kidney.

The results support the feasibility of using reflectance HSI to differentiate tissues found within a surgical scene and further support the use of pig renal tissue as animal test analogs to human renal tissue. Wavelength-by-wavelength statistical testing for each tissue comparison provides further information on the best spectral windows in which to detect spectral similarity and dissimilarity in biological tissue spectra. This preliminary database should prove easily expandable for future studies and reduce injury risk caused by misidentification of anatomy during surgery.

Table of Contents

List of Illustrations

List of Tables

Chapter 1

Introduction

1.1 The Common Bile Duct: a Quick Study in Anatomy

The common bile duct (CBD) is a vessel in mammalian bodies which carries bile from where it is produced in the liver to where it's stored in the gallbladder and where it is used to aid digestion in the duodenum.

Figure 1 shows a simple diagram of the biliary tree from its beginning in the liver to its end at the duodenum. The common bile duct (CBD) often runs parallel to the hepatic artery and hepatic vein, not shown in the figure. Bile is stored in the gallbladder until it is needed in the beginning of the small intestine for fat digestion.[1] Injury to the common bile duct can allow that bile to leak into the abdominal cavity, causing extensive damage, or block the duct completely, causing liver damage.[2-4]

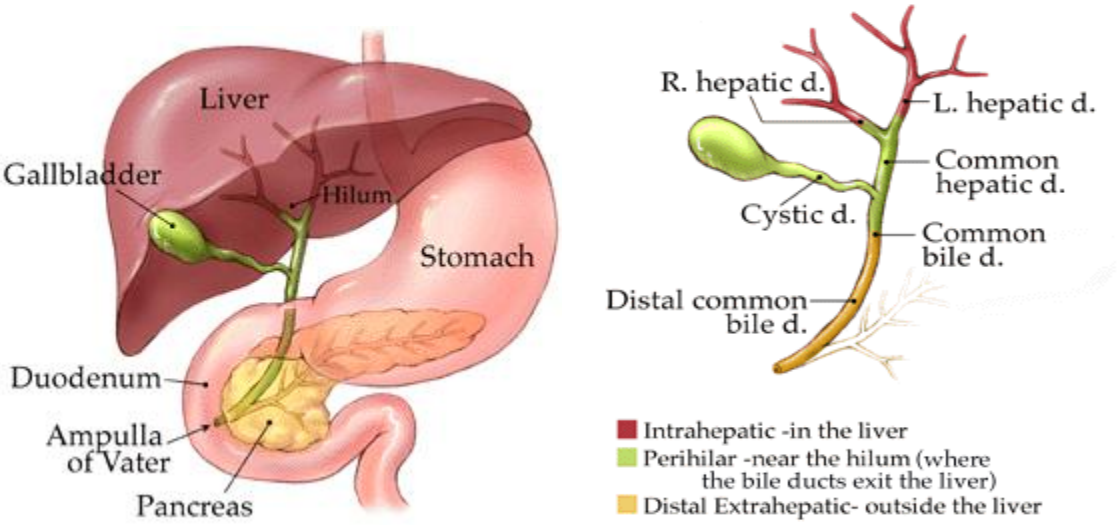

Figure 1.1: A simple diagram of the biliary tract. Bile is excreted from hepatocytes in the liver and collects in the gallbladder until it is needed for digestion of fats in the duodenum.

(http://pathology2.jhu.edu/gbbd/anatphys.cfm)

This anatomy can vary widely from patient to patient with varying length and diameters of the CBD. Some patients have even been observed to have no appreciable CBD at all, and instead the gallbladder empties almost directly into the duodenum.

One of the frequent health problems concerning the biliary system is the development of calcifications in the gallbladder known as gall stones, causing extreme discomfort and digestion issues. The most common treatment for gall stones is the removal of the gall bladder or cholecystectomy. Approximately 500,000 cholecystectomies are performed every year with 0.5% of those surgeries resulting in injury to the common bile duct, usually due to misidentified anatomy. Though this may seem like a small percentage at first, this still means 2500 undergo serious and painful complications from a relatively simple surgery every year, including sepsis, liver failure, and even death if the injury is handled incorrectly.[2-4] Procedures of this nature are further complicated by the fact that the common bile duct doesn't hold a consistent anatomy across every human being, and is often covered by fat and connective tissue, making it much harder to locate.[3,4]

Cholecystectomies are also commonly performed laparoscopically, which removes whatever tactile advantage a surgeon may have to determine anatomy from open surgery. Injury rates to the CBD are consequently higher in laparoscopic surgery than in open surgery.

If a reliable, quick, and accurate method to visualize the specific anatomy of the common bile duct and distinguish it from its surroundings or through the connective tissue can be developed, it could further reduce the risk of injury to the common bile duct during cholecystectomies and reduce the amount of time both the patient and surgeon need to spend in the operating room.

1.2 Introduction to Hyperspectral Imaging

Hyperspectral imaging (HSI) is used to remotely detect the optical spectra of materials. From these spectra, the chemical composition of a scene can be determined. Consequently, HSI yields considerable information about objects imaged in applications ranging from satellite imagery to microscopy and digital pathology.

HSI produces three-dimensional data sets which contain light intensities for hundreds of distinct increments of light for every pixel in an image, resulting in an image "cube" with two spatial dimensions (x, y) and one spectral dimension (λ). HSI has a wide variety of applications including geoscience, astronomical, and biomedical fields. With its growing popularity, investigators have to contend with large data sets that are difficult to analyze. In theory, a single mathematical method should emerge as the most efficient analytical tool, but in practice, different analysis methods are better suited for different applications. In some images feature identification and chemical identity might be important. In other applications, the amount of substance in a structure might need to be estimated. In yet others, the anomalous, low percentage image components may be the most important. Static images can be analyzed off-line, therefore analytic algorithm speed is not as important as it might be for real time analysis as is done for quality control or threat detection applications. Selection of the optimal HSI analytic methodology requires understanding of the basic mathematics for each method as well as knowledge of the continued advances in this field that are occurring at a rapid pace because of increased access to greater computer power.

Analysis of hyperspectral imaging requires 1) identification of what materials are present in each pixel and 2) how much of each material is there. This is complicated by "mixed" pixels in which two or more materials spectra are present in the same pixel. Numerous algorithms are available to solve these problems.

As a starting point, many algorithms require the identification of spectra that are characteristic for a material being studied. These are known as endmembers, or components, and are chosen from a reference library of spectra. Although this can be a subjective process, it is necessary in order to minimize the complexities inherent to the analysis of HSI data. Nevertheless, there is substantial interest in refining algorithms which can work with complete objectivity without user-defined input. Automated objective endmember extraction algorithms are invaluable for accelerating hyperspectral analysis to near real-time rates.

For most images, a pixel's spectrum is a mixture of individual endmember spectra. One of the major analytic challenges is to isolate each individual endmember contained within the total spectrum. The fraction of the total spectrum contributed by one endmember is called its abundance or abundance fraction. The process of determining the abundances of the endmember spectra in a mixed pixel is called spectral unmixing, abundance estimation, or inversion. When the contribution of one endmember in a pixel is so overwhelming that it can be considered the only endmember in that pixel, the pixel can be considered a "pure" representation of the substance that has the characteristic endmember spectrum. Pure pixels do not have to be unmixed, but instead are "classified," and classification of pixels based upon a library of spectra is often the simplest method applied in hyperspectral analysis.

Chapter 2 will discuss many hyperspectral analysis techniques in detail, and Chapter 4 will test a select few algorithms, supervised and unsupervised, on *in vivo* human data.

1.2.1 DMD-Based Hyperspectral Imaging

Many existing hyperspectral imaging systems depend on a filter to separate detected broadband illumination, such as reflected sunlight, into individual bands. These filters are often slow, either implementing a mechanical array of filters or tunable electro-optical filter. Using a digital micromirror device (DMD) chip in conjunction with a spectral grating for illuminating a target eliminates the need for a mechanical filter array or electro-optical filter on the detector side

of a hyperspectral imaging system, instead allowing for active spectral illumination .[5] With the capabilities of a DMD chip, one can cycle trough very narrow bandpass illuminations much faster than a filter, and when the source is synchronized with a camera, images at each illumination wavelength can be captured and quickly sorted into hyperspectral image cubes. This technology, specifically digital light projection (DLP®), allows for rapid collection of hyperspectral reflectance data at speeds previously unavailable to mechanical and electro-optical filter systems where the source was a controllable factor. This speed makes it feasible to collect an image cube with 100-plus frames in less than 30 seconds rather than a minute or more,[6,7] opening up avenues for reflectance hyperspectral imaging in surgical applications where every second can count.

A visible-range DLP® hyperspectral imaging system (HSI) has been previously developed for use in surgery.[5-14] Chapter 3 will explore the characterization of a 760 nm to 1600 nm NIR DLP HSI system. All data discussed and analyzed in Chapters 4 and 5 has been collected with a DLP HSI system either in the 380 nm to 780 nm visible range or 760 nm to 1600 nm NIR range.

Chapter 2

Review of Hyperspectral Analysis Methods

Comprehensive literature reviews are used widely by the medical community for definitive professional reference. Through the work of one or two people cataloguing the methods and results of many different researchers on a specific type of medical procedure, hours of time can be saved for those who make use of the published review. For this chapter, such a literature review was performed for many disparate hyperspectral analysis methods.

This review explores both commonly applied and lesser-known methods used for endmember extraction and abundance estimation in HSI images.

2.1 Basics: The Hyperspectral Data Cube

Hyperspectral data are organized into data cubes with two spatial dimensions (x-y positional) and one spectral dimension (light intensity at each wavelength band).

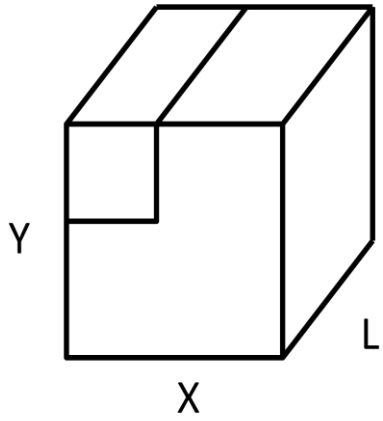

Figure 2.1: A typical hyperspectral image cube. X and Y denote the spatial dimensions with x representing the horizontal pixels and y thte vertical pixels.L represents the spectral dimension (λ). For each pixel in the x,y plane, there are as many data cells in L as there are spectral bands such that each x,y location is associated with an entire spectrum of light.

Each band is a narrow bandpass of light corresponding to a group of wavelengths. For most hyperspectral applications, the number of bands (L) is large, spanning hundreds of wavelengths and incrementing by few wavelengths between bands along the λ direction of the data cube. In order to address the practical problem of data storage and simplification of analysis, many algorithms first use a method to compress or reduce the dimension, meaning the size of the data (dimensionality reduction), either through band selection[15] along the λ direction of the data cube, transformation of the data using specific criteria of interest such as Principle Component Analysis (PCA), Minimum Noise Fraction (MNF), Projection Pursuit (PP),[16,17] or Singular Value Decomposition (SVD),[18] or by removing redundant data points through the use of exemplar vectors.[19]

Some methods for analyzing hyperspectral information are computationally expensive and require dimensionality reduction prior to their use.

2.2 Least Squares (LS)

One of the most commonly used algorithms for analyzing Hyperspectral data is least squares (LS) regression.[20-62] If component spectra contained within an image are known, the observed spectrum can be compared to the known one by minimizing the least square error using regression algorithms. The quantity (abundance) of the reference library spectrum that contributes to the complete spectrum can be estimated from the weighting coefficients of the least square equation. The fit is optimized by minimizing the residuals in a series of iterations that is used to estimate both the endmember spectra and the abundances with which those spectra appear. In the simplest cases, LS uses the Linear Mixture Model (LMM) minimized for the least squares residual:

$$r_i = \mathrm{M}\alpha_i + n_i$$

Where *r* is the mixed data spectrum, M is the matrix containing the reference signatures (endmembers) or signature matrix, α contains the abundance fractions, and *n* represents the

residual. The LMM is represented by a simple weighted matrix problem with additive error. The squared residual to be minimized is[27]:

$$\mathrm{E}(\alpha) = n^T n = (r - \mathrm{M}\alpha)^T (r - \mathrm{M}\alpha)$$

Where a superscript T indicates a matrix transpose. Residual minimization occurs when $\mathrm{E}(r)$ is differentiated with respect to α and set to 0,

$$\left.\frac{\partial \mathrm{E}(\alpha)}{\partial \alpha}\right|_{\hat{\alpha}_{LS}} = 0 \Rightarrow 2M^T r + 2(M^T M)\hat{\alpha}_{LS} = 0$$

Where the optimal LS estimate of α is $\hat{\alpha}_{LS}$.

$$\hat{\alpha}_{LS} = (M^T M)^{-1} M^T r$$

When the abundance fractions are known (which rarely is the case) this same method can be applied to find the endmember matrix (M) instead of the abundance fractions. Using iterative methods, both of these matrices can be found simultaneously, provided there is an initialization matrix prepared for one of the two matrices. For this purpose, it is acceptable to use a randomly generated matrix of appropriate size as an initialization matrix for either endmembers or abundances.

For the least squares method to be effective, the number of bands (described as wavelengths in most hyperspectral cases) contained in the data set must be larger than the number of endmembers to be classified. This is rarely a problem with hyperspectral imaging, where the number of bands routinely number in the hundreds, but it can be problematic for multispectral imaging. In other words, the number of equations must be greater or equal to the number of unknowns, otherwise the system will be ill-defined.

In practice, a number of constraints are imposed upon the least squares solution, so that the results found make physical sense. The most common constraints are 1) non-negativity of the abundance fractions and 2) that the abundance fractions sum-to-one. Non-negativity implies that no substance can have an abundance of less than zero because negative amounts of a physical

substance are not possible. Any calculated abundance violating this constraint is removed or set to zero. Since the measured spectrum is composed of a finite number of components, they all must all sum to one, giving rise to the term "abundance fraction."

$$\propto_i \geq 0\ , \quad \sum \propto_i = 1 \ \text{ for } i = 1, \ldots, N$$

Where *N* is the total number of abundance fractions.

When not all signatures are known, subspace estimation is used to estimate the number of endmembers. PCA, MNF, Hyperspectral Signal Identification by Minimum Error (HySime),[63] Virtual Dimensionality (VD),[63,64] Random Matrix Theory,[64] and Sparsity Promoting Iterated Constrained Endmembers (SPICE)[65,66] are examples of algorithms that can estimate the number of endmembers.

Although conceptually simple, LS estimation (LSE) may not produce optimal results. Consequently, several variations on the least squares method are used. Classical Least Squares (CLS) uses the LS error formulation with a non-negativity abundance constraint. Partially Constrained Least Squares (PCLS) uses the non-negativity or sum-to-one abundance constraints. Usually, non-negativity is applied since it is computationally less intense. Fully Constrained Least Squares (FCLS) uses both non-negativity and sum-to-one abundance fraction constraints. When both the endmembers and the abundance fractions are estimated by LS in an iterative method is used as described above. This alternating process, sometimes called Multivariate Curve Resolution (MCR), is repeated until a specified degree of convergence is met.

Other methods involving LS include Iterated Constrained Endmembers (ICE),[66,67,68] the Alternating Projected Subgradients (APS) optimization technique used for Nonnegative Matrix Factorization (NMF),[69] and weighted least squares, or the Gauss-Markov model,[70] which will be explained in the following.

LSE methods are very popular and are frequently used for endmember extraction and unmixing on real and simulated data.[54,55,71,72] Often when a piece of literature does not specify the

method of unmixing, i.e. Spectral Mixture Analysis (SMA), a LS method is implied.[55] Among its many applications, LS is one of the few to unmix fluorescence samples.[26,41] FCLS is shown to outperform unconstrained and partially constrained versions on real and simulated data in supervised and unsupervised implementations.[51] The unsupervised implementation of FCLS is also shown to produce less accurate abundance fractions, but is still preferable in complexity to using a separate endmember extraction method. FCLS is used often to unmix real and simulated images[42, 49] but can also be used to compress hyperspectral image cubes by separating them into abundance map images.[45] When FCLS is compared to Spectral Angle Mapper (SAM), Spectral Correlation Measure (SCM), and Spectral Information Divergence (SID) in terms of their fitness for spectral matching, SID outperforms the others in terms of correlation and RMSE due to its use of probability mass functions in the objective.[43] Several different versions of LS including unconstrained LS, CLS, rank-matched LS, Total LS (TLS), Bayesian with CLS priors, minimum variance (MV), and constrained MV, are compared to find that Bayesian with CLS priors gives the best estimate.[46] Unconstrained LS is used successfully for endmember extraction on simulated images with a genetic algorithm for abundance estimation.[47] LS unmixing abundance maps are used as a guide for spatial resolution enhancement in low-resolution real and simulated hyperspectral images.[48-50,56,73] CLS unmixing can be used in real-time on real data operating on a pixel-by-pixel basis for endmember detection and image classification.[52, 61] CLS can also be used for unmixing while taking spatial considerations into account, using iterative search windows to aid in mixed pixel classification of real and simulated data.[70,74] CLS is also compared to a method based on finding the SAM minimum of randomly chosen abundance fraction combinations, Iterative Fraction Combination Search (IFCS).[74] IFCS is shown to be more robust to noise than CLS and reduces the chance of getting "stuck" at local minima since it uses several random starting points for its abundance fraction search.

Parallel GPU LS algorithms with the assistance of kernels have been implemented for the unconstrained LS, CLS, and FCLS cases. Tested on real world data, these algorithms show the same accuracy as their serial versions but greatly speed processing time.[60]

2.3 Convex Geometry

The basic principle of convex geometry methods to define a convex space.[75-112] The space's boundaries consist of spectral endmembers. Being convex, the space between the boundaries consists of some linear combination of the boundary spectra, represented by the vertices of the boundary. Assuming an observed spectrum is a linear combination of endmember spectra, projecting in the convex space from the observed spectrum to the endmember facilitates determination of what fraction (i.e. abundance) of the observed spectrum is composed of the endmember. This area can be defined by a geometric simplex (the smallest geometric shape that can connect a given number of vertices).

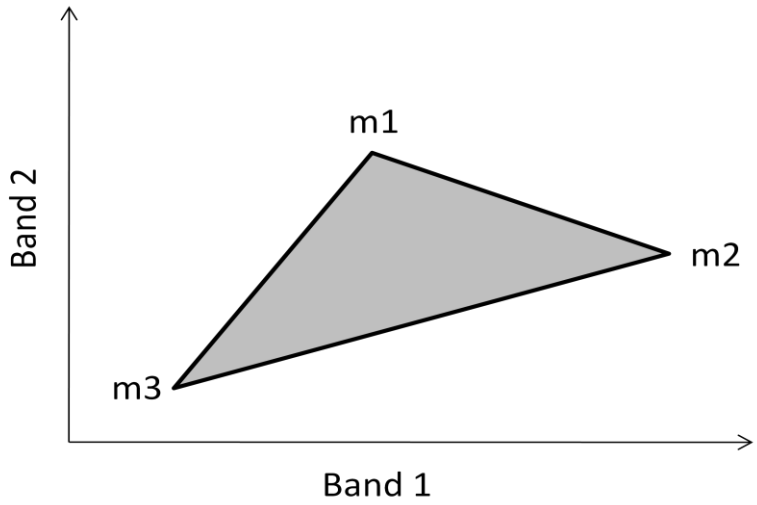

Figure 2.2: Convex geometry diagram illustrating the idea that any data point is a linear combination of the endmembers in a simple, 2-dimensional model. The simplex for a 2-dimensional model is a triangle, and m1, m2, and m3 denote the vertices which represent the endmember spectra.

Being a convex set, every data point should lie within the boundaries of the simplex, a form called the "data cloud." In general there are two groups of methods which find the endmembers using this logic: simplex growing algorithms which initialize a simplex at a point within the data cloud and grow outward to find the endmembers, and simplex shrinking algorithms which initialize their search outside the cloud and reduce the size of the simplex to find the endmembers.

2.3.1 Convex Cone Analysis (CCA)

Convex Cone Analysis (CCA)[38, 78, 113] is a convex geometry method which operates on the principle that the eigenvectors of an observed data cube must exist inside its convex region, which is not necessarily defined by a simplex. CCA finds the boundaries of the convex region with origin at zero (roughly cone-shaped, hence the name) and uses these corner spectra as endmembers for unmixing or target spectra for classification. The convex region contains all positive linear combinations of the boundary spectra. While geometric visualizations are commonly used, vertex spectra are determined algebraically using eigenvectors and eigenvalues in a singular value decomposition (SVD) operation, thus producing unique solutions without need for iterations.

In order to use CCA for best results, the data spectra must be normalized, since this simplifies the calculations. With a matrix of n x m size and b number of bands, the data should be arranged into a nm x b matrix S with rows being full spectra and columns containing all pixels for each spectral band, as shown below.

	Pixel							
Intensity	(x_1,y_1)	i1	i2	.	.	.	ib	
	(x_1,y_2)							
	.							
	.							
	.							
	(x_2,y_1)							
	(x_2,y_2)							
	.							
	.							
	.							
	(x_m,y_n)							
Band		λ_1	λ_2	.	.	.	λ_b	

Figure 2.3: Schematic of the 2-D arrangement of a 3-D hyperspectral data cube.

Where *i* denotes an intensity value, λ denotes wavelength or band number, and x and y denote pixel coordinates.

The data can then be made into a correlation matrix of b x b size, **C**.

$$\mathbf{C}=S^TS$$

Using SVD for diagonalizing a square symmetric matrix, the eigenvectors of **C** can be found.

$$\mathbf{C}=\mathbf{PDP}^T$$

Where **P** is the orthonormal matrix of eigenvectors of **C**, and **D** is a diagonal matrix containing the corresponding eigenvalues. **D** and **P** are the same dimension as **C** and arranged so that the eigenvectors in the columns of **P** are associated with the eigenvalues of the same column in **D**. This is known as the Karthunen-Loève Transform, which is similar to principle component analysis (PCA), except that it uses a sample correlation matrix instead of a covariance matrix.

At this point, the number of components of interest must be known. They must be no greater than the dimensionality of **C** +1, with $c \leq b$. In hyperspectral imaging, this is not usually a

concern, as *b*, the number of spectral bands, is typically much larger than the *c* number of endmembers. The *c* number of eigenvectors with corresponding largest eigenvalues are selected, and the cone boundaries where the linear combinations of eigenvectors produce only nonnegative vectors are found.

$$x = p_1 + a_1 p_2 + \cdots + a_{c-1} p_c \geq 0$$

Where p_i are eigenvectors corresponding to the *c* largest eigenvalues and the a_i coefficients can be scaled to make the coefficient of $p_1 = 1$, thus giving $c - 1$ number of parameters. The p_1 eigenvector is aligned along the axis of the cone, and the coefficient sets found with nonnegative and zero eigenvector elements make up the corners of the convex cone.

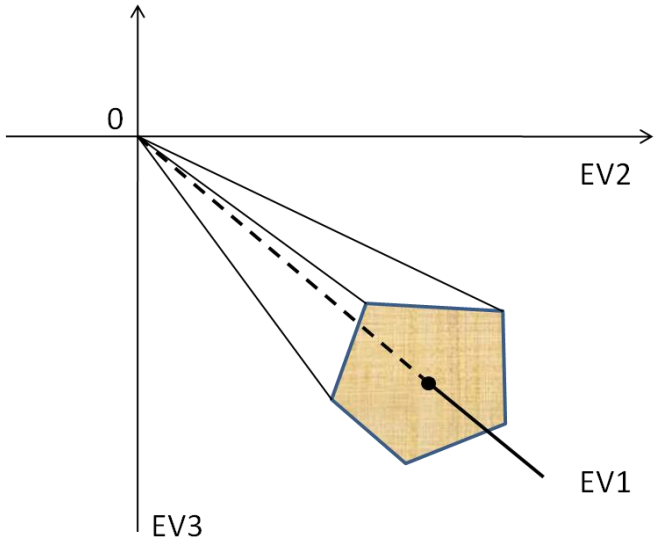

Figure 2.4: A convex cone in the case of *p*=3.

The standardized algorithm takes the above equation and places it into a matrix algebra form where p_i are *b*-dimensional column vectors. The inputs for this algorithm are the first *c* number of eigenvectors, p_1 through p_c, and the outputs are the set of corner vector spectra defining the cone.

With increasing number of components of interest and bands, the possible solutions for this algorithm increase quickly. Dimension or band reduction, multiple processors, and processing large scenes by sections can be useful to cut down computation time.

CCA is used for pattern recognition, turning this endmember extraction method to shape retrieval in real data,[38] compared against ICA and AMMs, where AMMs are found to be more appropriate for the application, but CCA returns adequate results. It's also used for endmember extraction on simulated data[78] and used as a benchmark endmember extraction tool for comparison purposes against Independent Component Analysis and Associative Morphological Memories.[113]

2.3.2 Minimum Volume Transforms (MVT)

Minimum Volume Transforms (MVT)[79,39,93] is a simplex shrinking algorithm, finding a simplex which encompasses all the data before shrinking it to the minimum which will encompass the data cloud. It is used as the endmember extraction portion of the ORASIS process. There are two different, yet equally valid variants of MVT, the dark-point-fixed (DPF) and fixed-point-free (FPF) transforms. The DPF transform involves normalization of data and then the movement of the coordinate hyperplane to use one of the simplex vertices as the origin, while the FPF transform uses coordinates barycentric, or located at the center of mass, with respect to the vertices of a simplex circumscribed in n space. Both of these transforms are potentially storage and computation intensive, therefore data reduction techniques are encouraged prior to processing. One of these techniques, called "data depletion" involves removing points not shared by the convex hull of the simplex. DPF is tested using real-world data with favorable results.[39,93]

2.3.3 Alternating Volume Maximization (AVMAX)

Alternating Volume Maximization (AVMAX)[79,81]) and robust version (RAVMAX) are volume maximization algorithms (based on N-FINDR) which involve an alternating optimization algorithm and record the change in volume of the simplex. If the volume exceeds a threshold, the volumes are updated and the iteration proceeds. Once the volume is considered optimal, the

abundances are calculated. The robust version of the AVMAX algorithm reformulates AVMAX into smaller subproblems so that chance constraints can be applied to second-order convex cone problems in order to adjust for noise. AVMAX was compared to N-FINDR and found comparable.[79] In simulations, RAVMAX was shown to outperform N-FINDR, VCA, and the original AVMAX algorithm.[81]

2.3.4 Minimum Volume Enclosing Simplex (MVES)

Minimum Volume Enclosing Simplex (MVES),[75,82,84] also called Alternating Volume Minimization (AVMIN) is a simplex shrinking algorithm. As part of the process, the data first undergoes an affine transform analogous to a dimension reduction step, where an affine transform is one that preserves collinearity. The algorithm can then be formed as an optimization problem to minimize the volume of the simplex, and the verticies of the optimal minimized volume are defined as the true endmembers.

$$V(\beta_1, \dots, \beta_N) = \frac{|\det(\Delta(\beta_1, \dots, \beta_N))|}{(N-1)!}$$

Where $\Delta(\beta_1, \dots, \beta_N)$ is a matrix of the $\beta_i$vectors to be optimized to find the endmembers with a row of 1's at the bottom and *N* is the number of endmembers. For this method to work, *N* must be known ahead of time, which can be determined through virtual dimensionality (VD) or HySime. The pure pixel assumption is not needed for this method, but constraints for non-negativity, sum-to-one, and the minimum number of bands is greater than N are used.

The above equation can also be reformulated to turn the nonconvex constraints into convex constraints, which results in a problem for partial maximization of the objective function instead of minimization. This formulation eventually results in a row-wise minimization of the volume conducted cyclically.

With creative substitutions, both the endmembers and the abundances can be estimated from this method without conventional inversion processes.

In simulations, MVES performs worse as pixel purity levels increase, but performs better than other benchmark algorithms (PPI, N-FINDR, VCA, APS, MVC-NMF, MVSA, ICE) in many cases.[75] MVES is also tested against VCA, PPI, and APS[75] and against MVSA[82] on simulation data with superior results. MVES reveals EMS in high agreement with ground truth data and retrieves more endmembers than VCA and MVC-NMF, though they are not all the same endmembers and not retrieved with the same confidence.[75]

The robust version of MVES (RMVES) introduces chance constraints to account for noise, as with RAVMAX.

2.3.5 Minimum Volume Simplex Analysis (MVSA)

Minimum Volume Simplex Analysis (MVSA)[75,79,82,114] is another minimum volume algorithm for the purpose of linearly extracting endmembers from hyperspectral data and therefore does not depend on the pure pixel assumption. Initialization is very important with this algorithm, so data is processed with a pure pixel simplex algorithm (such as VCA) and inflated in order to initialize MVSA. Two algorithm acceleration techniques are used, including the discarding of all points inside the pure pixel algorithm initialization, since none of them can be an endmember, and the selection of an appropriate inflation factor for the initialization, which if chosen properly can allow the ignoring of a majority of the constraints.

This algorithm focuses on finding "good" sub-optimal solutions to an optimization problem defined by:

$$Q^* = \arg\max \log|\det(Q)|$$

$$\text{s.t.:} \quad QY \geqslant 0, \qquad 1_p^T Q = q_m$$

Where Q is the inverse of the matrix containing the endmembers, Y is the matrix containing the input data, p is the number of endmembers, and $q_m = 1_p^T (Y_p)^{-1}$. The optimization problem is then solved by solving the respective Kuhn-Tucker equations using sequential quadratic programming (SQP), which accumulates second-order information about the Kuhn-

Tucker equations. The quadratic problems build quadratic approximations of the Lagrangian formulation associated with the optimization problem above, and therefore the gradiant and Hessian of the function $f(Q) \equiv \log|\det(Q)|$ is included in every SQP iteration.

In addition, a method to increase the robustness of the algorithm is suggested, replacing the hard nonnegativity constraint with a hinge-type constraint which can allow for nonnegative abundances, similar to the hinge constraint used in SISAL (described below).

MSVA performance is compared against VCA and NMF-MVT[114] and is shown to perform better than NMF-MVT in both error and time taken, though the time for computation passes NMF-MVT when the number of endmembers to be found exceeds 15. MSVA is also tested with MVES[75,82] (as discussed with MVES) and AVMIN based on MVSA is compared with the AVMAX algorithm.[79]

2.3.6 Simplex Identification via Split Augmented Lagrangian (SISAL)

Simplex Identification via Split Augmented Lagrangian (SISAL)[102] is a recent method which unmixes data through use of hinge-type "soft" constraints whose strength are controlled by regularization parameters instead of the hard constraints of nonnegativity and sum-to-one for the endmembers and abundance fractions. This change offers several advantages, mainly robustness to outliers, noise, and poor initialization and the potential to handle much larger problems than current state-of-the-art algorithms for the same purpose. In addition, when the values of the regularization parameters become large, they approximate the hard constraints.

To implement SISAL, it is understood that the inverse of the matrix M containing the endmembers ($Q=M^{-1}$) is not ideal, therefore not symmetrical or positive definite and therefore not convex, which is a problem for most convex geometry algorithms. SISAL therefore solves a sequence of nonsmooth convex subproblems in order to solve the hard nonconvex optimization problem, using variable splitting to get the soft constraint formulation and then apply augmented Lagrangian techniques. Initial formulation yields the objective function to be optimized:

$$Q^* = \arg\min \; -log|\det(Q)| + \lambda\|QY\|_h$$

$$s.t.: 1_p^T Q = a^T$$

Where Y is the matrix containing the mixed data, p is the number of endmembers (known at the start of the algorithm), $a^T = 1_n Y^T (YY^T)^{-1}$ $\|X\|_h \equiv \sum_{ij} h(|x|_{ij})$, and $h(x) \equiv \max\{-x, 0\}$ is the so-called hinge function. In the above, $\|QY\|_h$ serves as a soft parameter or "regularizer," penalizing negative components of QY proportionally with their magnitudes while λ is the regularization parameter which controls its impact on the overall equation.

Next, a sequence of subproblems is formulated to solve the above objective function, and the minimization step involves use of a variable splitting augmented Lagrangian algorithm. The sequence is initialized with an estimate from VCA, necessarily already reduced in dimension.

When the variables are split, it splits the column vector q (the version of Q with all its columns stacked into one column vector) into (q,z) such that $Aq = z$. The augmented Lagrangian (AL) is then formulated as follows:

$$\mathcal{L}(q, z, d, \tau) \equiv E(q, z) + \alpha^T(Aq - z) + \tau\|Aq - z\|^2$$

$$= E(q, z) + \tau\|Aq - z - d\|^2 + c$$

Where

$$E(q, z) \equiv g^T q + \mu\|q - q_k\|^2 + \lambda\|z\|_h$$

and $d = {}^{-\alpha}/_{(2\tau)}$, g is the negative inverse of q (or the gradient of $f(q) = -log|\det(Q)|$), α holds the Lagrange multipliers, μ is a value chosen at initialization to be greater than 0, k is an index number starting at 0 and progressing until the end of the iterations are reached by some stopping criterion, and c is an irrelevant constant. The AL algorithm then minimizes $\mathcal{L}$ with respect to (q,z) and updates α, eventually converging to a solution. This can be improved upon, however, with block minimizations with respect to q and z separately which are light on computation. The alternating split AL algorithm which minimizes $\mathcal{L}$ is then inserted into the

sequence of subproblems in place of the harder minimization process to produce the SISAL psuedocode formulation.

The relatively simple step-wise process of the SISAL algorithm allows for light computation which can handle a very large number of endmembers and data points. SISAL is compared to MVSA and MVES and was found to be faster and able to handle significantly more endmembers while producing comparable error.[102]

2.3.7 Sparse Regression (SR)

Sparse Regression (SR)[103-105,115] is used in the case when spectral libraries are used to help unmix data. Since there are theoretically very few endmembers present in an image compared to the entire library, the endmember matrix is made up of mostly zeroes, i.e. sparse. When there are more zeroes, the matrix is more sparse.

$$\min_{M} \|M\|_0 \quad s.t. \|r - M\alpha\|_2 \leq \delta$$

Where δ is an error tolerance term and $\|M\|_0$ denotes the l0 norm which counts the number of nonzero entries. This problem is not convex and therefore difficult to solve. Using the l1 norm (the sum of the absolute values of the columns) instead creates a convex problem which can be solved through linear programming and gives the same solution as the l0 norm. Using an error tolerance term allows the pursuit of stable solutions. Furthermore, the nonnegativity constraint may be applied to these matrices for improved unmixing accuracy.

Using the above equation, Constrained Sparse Unmixing via variable Splitting and Augmented Lagrangian (CSUnSAL) can be tailored for each sparsity-promoting variation (with or without error tolerance and with or without nonnegativity constraint). Constrained optimization can be altered to unconstrained by minimizing Lagrangian terms, such as in Sparse Unmixing via variable Splitting and Augmented Lagrangian (SUnSAL).

$$\min_{M} \frac{1}{2} \|M\alpha - r\|_2^2 + \lambda \|M\|_1$$

Where λ is a Lagrangian multiplier. In the λ = 0 case, the solution presented is the LS solution. When the nonnegativity constraint is applied to this equation, the result is nonnegatively constrained LS (NCLS) and imposing the sum-to-one constraint afterwards gives FCLS.

Another method using l_1 norms is called the L_1 estimator,[115] related to the Sparsity Promoting Iterated Constrained Endmembers (SPICE) described later, which instead uses l_2 norms. The l_1 norm has a lower penalty value than l_2 for large errors and therefore a larger tolerance for outliers. The L_1 estimator uses three terms in its iterative objective function.

$$E_{l_1}(M,\alpha) = \|r - M\alpha\|_{l_1}$$

$$E_H(M,\alpha) = \sum_{i=1}^{N}\sum_{j=1}^{P}\rho((r_i - M\alpha_i)_j)$$

$$E_V(M) = \frac{1}{2}\sum_{i=1}^{N}\sum_{j=1}^{N}(m_i - m_j)^T(m_i - m_j)$$

$$E_S(\alpha) = \sum_{k=1}^{N}\lambda_k\sum_{i=1}^{N}|\alpha_{ik}|$$

$$\lambda_k = \frac{\Lambda}{\sum_{i=1}^{N}\alpha_{ik}}$$

where P is the number of bands, N is the number of endmembers, Λ is a sparsity control parameter, and ρ denotes the Huber M-estimator cost function that approximates the l_1 norm.

$$\rho(t) = \begin{cases} \frac{1}{2}t^2, & |t| \le \gamma \\ \gamma|t| - \frac{1}{2}\gamma^2, & |t| > \gamma \end{cases}$$

where γ is a positive constant parameter, and as it approaches 0, the cost function estimator becomes the l_1 norm. The total objective function is then:

$$E = E_H + \beta E_V + E_S$$

E_H computes the error between the pixel input and the reconstruction using the endmembers and proportions, E_V promotes the endmembers which provide a tight fit around the

data with β as a weight coefficient, and E_S uses sparsity promotion with a Laplacian distribution dependent on the number of endmembers. The estimate iteratively updates the abundances, endmembers, and number of endmembers, pruning the endmembers whose abundances are below some threshold.

NCLS, FCLS, CSUnSAL, and SUnSAL all have the same theoretical computational complexity and perform better than techniques without explicit sparseness, such as Orthogonal Matching Pursuit (OMP) on real[103] and simulated data.[103,105] Overall, CSUnSAL and SUnSAL have similar performances,[103-105)] though SUnSAL tends to perform better in the presence of white noise.[104] The most favorable scenarios for these algorithms are the ones in which the endmembers are not coherent with each other and the endmember matrix is very sparse, i.e. the number of endmembers is low ($\leq$10).[103] In fact, the complexity of the algorithm depends more on the size of the available library from which endmembers are chosen than the size of the image, unlike other algorithms.

The L_1 estimator is compared against SPICE and HySime in which HySime underestimates the number of endmembers, and when SPICE estimates the number of endmembers correctly, it gives endmembers with lower variance and lower error between the data and reconstruction than the L_1 estimator does. The L_1 estimator, however, gives more consistently correct estimates of the number of endmembers in simulated data cases.[115]

2.3.8 Orthogonal Matching Pursuit (OMP)

Orthogonal Matching Pursuit (OMP)[103,105] is an optimization technique for use when searching spectral libraries for endmembers. It searches for the endmember in the library which best describes a predetermined residual, the first residual being the first observed pixel in the image data. Once the endmember is chosen, it adds the endmember to the endmember storage matrix, updates the residual, and computes a new abundance estimate. The residual is orthogonalized with respect to the endmembers already selected in order to avoid redundancy in

selection. The process iterates until a stopping criterion is reached, i.e. a predetermined number of endmembers.

OMP is compared to the sparsity-promoting algorithms above (CSUnSAL and SUnSAL) for efficacy in unmixing by chosing endmembers from a library, where it is shown to be more computationally complex and not as accurate on simulated[103,105] and real data.[103]

2.3.9 Vertex Component Analysis (VCA)

Vertex Component Analysis (VCA)[83,88,94] is an endmember extraction technique that exploits two facts: 1) the endmembers are verticies of a simplex in transformed space and 2) the affline transformation of a simplex is also a simplex. Like CCA, it assumes the presence of pure pixels, but unlike CCA it is an iterative algorithm, sequentially projecting data onto a direction orthogonal to the subspace of already determined endmembers. Newly found endmembers are considered to be the extreme of the new projections, and the iterations continue until all possible endmembers are found. This technique is commonly used with dimensionality reduction beforehand, but can also be used on data that has not been previously reduced.

In order to perform VCA, the inputs to the algorithm are *p*, the dimension of the spectral subspace, and the experimental data. The second step determines the dimensionality reduction to use based on the data SNR. The cone initializes a storage matrix for the projection of endmember signatures which is also used to generate projections onto orthogonal space. It outputs an estimation matrix of the final endmember signatures. VCA has been found to be less complex than both PPI and N-FINDR and exhibits better performance accuracy than PPI and comparable accuracy to N-FINDR.

2.3.10 N-FINDR

N-FINDR[18,19,32,42,68,79,85,95-101,116-118,152] is a highly popular geometric endmember extraction algorithm often coupled with constrained least squares unmixing to produce abundance maps. It is classified as a simplex growing algorithm, cycling through every pixel spectrum in a

hyperspectral image in order to find the simplex of maximum volume, starting with a random endmember vector and ending when every pixel option has been exhausted.

As a pre-processing step, the dimensionality must be reduced to the number of endmembers, N, minus one. This is done so that simplex volume may be determined in later steps, and is most often accomplished by orthogonal subspace projection (OSP). While MNF theoretically produces better results, SVD and PCA both work equally well.

To determine simplex volume, an endmember matrix is constructed with a row of 1's in the first row,

$$E = \begin{bmatrix} 1 & 1 & \cdots & 1 \\ e_1 & e_2 & \cdots & e_N \end{bmatrix}$$

Where e_i represents a column vector containing the spectra of the *i*th endmember. The volume, proportional to the determinant of E, can then be written as:

$$V(E) = \frac{1}{(N-1)!} abs(|E|)$$

Where N-1 is the number of dimensions occupied by the endmember data.

N-FINDR then begins a process of nonlinear inversion, starting with a random set of pixels as the initial endmembers. Every pixel in the image is evaluated for purity, and one of the base assumptions of the algorithm is that there is at least one pure pixel in the image scene. Trial volumes are then calculated for every endmember position by replacing that endmember with a new pixel spectrum and recalculating the volume. If the volume increases, the new pixel is considered the new endmember. This procedure continues until no more replacements are possible. This process is essential a non-linear inversion to determine the largest simplex that can be inscribed into the data. If there are no pure pixels for one or more endmembers, a fundamental violation of one of the underlying assumptions, local maxima may exist. The algorithm can, however, be run several times with different random initializers, and the endmember set that returns the largest total simplex volume may be considered the final solution.

The output of the N-FINDR algorithm is a set of images called abundance maps which depict the fractional abundance of each endmember at each pixel in a scene as a gray-scale image. Abundance maps are most commonly formed by non-negatively constrained least squares inversion, where the non-negativity constraint forces the abundance to conform to the idea that one cannot have a negative amount of a physical substance. This is a computationally complex portion of the N-FINDR process, and consequently most computation time is spent on the unmixing portion.

N-FINDR is tested with synthetic data and real aerial data from the well-understood Cuprite, NV site. The endmembers extracted with the N-FINDR algorithm were compared to spectra published by the USGS and found to have a good resemblance.[18] N-FINDR was compared to PPI, ORASIS, and IEA also using real-world data from the Cuprite, NV site, and each algorithm produced similar outputs to each other.[19] N-FINDR was also compared to PPI, VCA, APS, MVC-NMF, MVSA, ICE, and MVES with numerous Monte Carlo simulations where MVES was shown to outperform the other algorithms in most cases.[75]

N-FINDR is shown to have many drawbacks, for all its simplicity, effectiveness, and popularity. For one, there is no provided criterion for finding the number of endmembers present in an image, a number which must be known at the initialization of the algorithm. Secondly, the algorithm is initialized by a randomly generated endmember vector, and different initializers can lead to different final endmembers, which leads to reproducibility issues. Plus, as the number of endmembers becomes large, the computational complexity of finding the simplex becomes much higher. Proposed fixes to these shortcomings include the implementation of virtual dimensionality to calculate the expected number of endmembers, including an endmember initialization algorithm (EIA) to optimize the initializing endmember, or turning the randomness of the algorithm into an advantage by implementing iterative algorithms.[98]

The simplicity of N-FINDR's formulation has led to its use and modification by many sources.[97,98,100,101] Variations of N-FINDR include a "fast implementation,"[97] and two series implementations, Iterative N-FINDR (IN-FINDR) and SuCessive N-FINDR (SC N-FINDR).[98] The "fast" implementation[97] involves several modifications of the base N-FINDR algorithm, including the implementation of virtual dimensionality to find the number of endmembers in a scene 'N.' The algorithm then finds 'N' number of pure pixels in a scene using the classical N-FINDR algorithm with exhaustive search methods, including spectral angle mapping. Classical N-FINDR is then used again to find the final 'N' most pure pixels from the selected pure pixels. This division of the pixels into groups is shown to reduce computation time by 5 times or more, depending on the size of the image, in both simulated and real world data.

IN-FINDR, SC N-FINDR, and their variations which take purely randomized inputs are recent redesigns of the N-FINDR algorithm to turn the random vector initializations of the classical N-FINDR from a drawback to an advantage. IN-FINDR searches for endmembers in two loops, inner and outer, iteratively. SC N-FINDR finds endmembers successively, such that endmembers found earlier in the process are fixed and remain unchanged while the algorithm searches for subsequent endmembers instead of changing them if a more suitable endmember is found. The random versions implement random sets of initial conditions as a single run and the result from a single run is considered a realization of the algorithm. Different runs produce different realizations with the same algorithm, but if the information is important, it is assumed to show up in multiple or all realizations, such as endmembers. These algorithms are able to run with un-compressed data sets (no data reduction), and were tested with real world data.[98] Random SC N-FINDR was found to be the fastest algorithm, with just over a minute of computation time, but none of the four new algorithms were compared to the classical N-FINDR algorithm.

N-FINDR has been implemented in parallel and compared to the original N-FINDR and found comparable, though the non-parallel version is found to perform better on average.[100,116]

Classical N-FINDR is also compared with a different implementation of N-FINDR,[101] which incorporates oprimization to both implementations. Though the optimizations both improve over their non-optimized versions, the different implementations themselves see little difference between each other when accuracy and maximum volume achieved are compared.

2.3.11 Pixel Purity Index (PPI)

Pixel Purity Index (PPI)[19,108-110] is considered a forerunner to the N-FINDR algorithm. Through repeated projections onto randomly oriented lines in an N-dimensional space, PPI seeks to find the purest pixels in a hyperspectral image scene. It requires dimensionality reduction with MNF before randomly generating lines in an N-dimensional space comprising a scatter plot of the transformed data. All points in the space are then projected onto the line, with pixels falling onto the extremes of that line being counted. This process is repeated for many repeated projections onto different lines, and pixels with final counts exceeding a certain threshold are considered "pure". This process results in many redundant spectra, and the final decision concerning which spectra to determine as the true endmembers is dependent on a trained analyst.

Though PPI depends largely on an operator's involvement, it is used for endmember extraction in a great deal of the literature.[56,72,75,83,107-110,118,119,120-128] PPI was compared to N-FINDR, ORASIS, and IEA in terms of endmember extraction accuracy using real-world data, and each algorithm produced similar outputs to each other.[19] In the case of Lasso, it is used to initialize the endmember extraction algorithm by first finding the most extreme vectors.[109] PPI is also notably modified for automatic endmember extraction in order to turn the standard random initialization of endmembers into a strength through cross-correlation of resulting endmembers, outperforming the regular version of PPI.[118]

2.3.12 Optical Real-time Adaptive Spectral Identification System (ORASIS)

Optical Real-time Adaptive Spectral Identification System (ORASIS)[19,32,125] is the first hyperspectral analysis algorithm specifically designed for rapid throughput of data. It requires no

dimension reduction, but instead uses Exemplar Selection in order to thin the data set. Exemplar selection rejects "redundant" spectra by calculating the angle between spectral vectors and discarding vectors which do not exceed a threshold separation angle. Using a Gram-Schmidt process, it then finds a basis set of much lower dimensionality and projects the exemplar spectra onto the basis subspace. It then finds a simplex through MVT and derives the endmembers from the vertices. ORASIS then uses filter vectors for unmixing and producing the fractional abundance maps instead of LS, so the output abundance maps are not subject to the constraint that the contained abundances lie between 0 and 1. This arbitrary scaling of the output endmember spectra and unconstrained unmixing leads to difficulty in comparing the output of ORASIS with other endmember extraction techniques, such as N-FINDR and IEA.[19]

2.3.13 Iterative Constrained Endmembers (ICE)

Iterative Constrained Endmembers (ICE),[67,68] Sparsity-Promoting version (SPICE),[65] and its Robust version (R-SPICE) simultaneously estimate the endmembers, number of endmembers, and abundance fractions in convex regions of a hyperspectral data set. This technique seeks to overcome the problems of noise sensitive MVT and pure-pixel assuming N-FINDR. ICE by itself estimates both the endmembers and abundances through a series of iterated regularized least squares minimizations (residual sum of squares), holding the endmember or abundance values that aren't being optimized at the time constant while the other matrix is updated.

$$RSS_{reg} = (1 - \mu)\frac{RSS}{N} + \mu V$$

Where RSS is over all pixels, μ is a small regularization parameter between 0 and 1 which trades off RSS and V, and V is a measure of the size of the simplex termed "total variance," which is the sum of the variances of the simplex verticies and computationally cheaper than volume.

SPICE adds to the ICE algorithm by adding a sparsity-promoting Laplacian prior on the abundance calculation which allows the algorithm to estimate the number of endmembers. R-

SPICE is an extension of SPICE which differs by weighting each pixel based on its spectral similarity to the other pixels of the data set. This allows for a more stable output over a wider range of parameters and removes outliers.

The objective function to be maximized uses the likelihood of the data given the endmembers and abundances $p(X|A,E)$, a prior on endmembers $p(E)$, and a sparsity-promoting prior on the abundances $p(A)$.

$$\ln\big(\, p(X|A,E)p(E)p(A)\big)$$

$$p(X|A,E) = \exp\left\{\frac{-1}{2}\sum_{i=1}^{N}\frac{w_i}{v}(x_i - \sum_{k=1}^{M} a_{ik}e_k)^{T}\ (x_i - \sum_{k=1}^{M} a_{ik}e_k)\right\}$$

$$p(E) = \exp\left\{\frac{-1}{2\beta}\sum_{k=1}^{M-1}\sum_{l=k+1}^{M}(e_k - e_l)^T(e_k - e_l)\right\}$$

$$p(A) = \exp\left\{\frac{-1}{2}\sum_{k=1}^{M}\gamma_k\sum_{i=1}^{N}|a_{ik}|\right\}$$

Where $w_i = \frac{1}{1+\frac{d_i}{\eta}}$ is the weight assigned to each data point, with d_i being the distance from x_i to the mean of the data set and η being the mean of the d_i values, v is the importance term, N is the number of pixels, M is the number of endmembers, a_{ik} is the abundance of endmember k in pixel i, e_k is the kth endmember, β is a parameter assigning weight to the endmember prior, and $\gamma_k = \frac{\Gamma}{\sum_{i=1}^{N} a_{ik}}$ using abundance values from the previous iteration, and Γ is a constant associated with driving the abundance values to zero.

The objective function is iteratively maximized, alternating between updating the endmembers and abundances using quadratic programming. While one is being updated, the other is held constant, and in the next iteration, they switch which is being updated. Iterations continue in this way until a convergence criterion is met.

To find the number of endmembers, the algorithm is initialized with a large number of endmembers, and abundances associated with unneeded endmembers are driven to zero by the sparsity-promoting prior. When the abundance fraction associated with that endmember fall below a threshold, the endmember is eliminated.

ICE was compared to N-FINDR and ICA on simulated data where N-FINDR performed better since there were pure pixels, though on real data, ICE outperformed N-FINDR.[68] R-SPICE was used successfully to find endmembers, number of endmembers, and abundance fractions on real world data partitioned by PCE.[65] Due to its nature of removing outliers, R-SPICE would not be viable for anomaly detection.

2.3.14 Maximum Distance (Max-D)

Maximum Distance (Max-D)[106,107,129] is an endmember extraction algorithm which uses Euclidean distance calculations and hyperplane projections in order to sequentially select the endmembers in a hyperspectral data set. Max-D first calculates the Euclidean distances of all the points and chooses the two points of maximum Euclidean distance as the first two endmembers. All the points are then projected onto the hyperplane orthogonal to the vector containing those first two endmembers, and the point lying furthest from those is selected as the third endmember. The points are collapsed again, and the process repeated until the requisite number of endmembers are found. This process allows for the selection of a number of endmembers equal to one more than the number of bands.

Max-D is tested on real world data.[106,107] It is used to find the endmembers for the testing of a spectral unmixing method vs. a straight classification method[106] and it is compared against PPI[107] and found to have comparable, but faster output with differences explained by the fact that Max-D derives endmembers from the image data whereas PPI uses a spectral library. As with any unsupervised algorithm, Max-D can erroneously select anomalies or extremes in place of actual

endmembers, so to fix this, it is recommended to run Max-D twice, with the second run after removing the endmembers found in the first run from the data.

2.3.15 Sequential Maximum Angle Convex Cone (SMACC)

Sequential Maximum Angle Convex Cone (SMACC)[109,129-131] is based on the Spectral Angle Mapper (SAM) algorithm, which compares the angles formed between the automatically selected reference endmembers and the image pixel spectra. It is an endmember extraction method which sequentially creates convex cones from existing endmembers and finds new endmembers based on maximum spectral angle divergence from current endmembers.

SMACC is compared in efficacy against basic Linear Spectral Unmixing (LSU) with comparable results on real world data.[130] SMACC is compared against N-FINDR and performs faster, but N-FINDR is in general more accurate in determining endmembers with real world data.[131] Compared to a Lasso-based algorithm and N-FINDR, SMACC is found to be the least accurate of the three, underestimating the number of endmembers present in real and simulated data.[109]

2.3.16 Iterative Error Analysis (IEA)

Iterative Error Analysis (IEA)[19,132] is a sequentially iterative endmember extraction process which creates multiple error images of a hyperspectral scene by LS unmixing. This method takes a full hyperspectral data cube with no dimensionality reduction to the input and uses the mean spectrum of the data as an initial vector. A non-negative constrained or fully-constrained LS unmixing is performed using the initial vector, and an error image is performed. The average of the vectors with the largest error (defined as spectral distance from the first vector) are taken as the first endmember. The image undergoes constrained unmixing again using the first endmember in place of the initialization vector, and another error image is formed. The average of the vectors with the largest error distance from the first endmember are then taken as the second endmember, and the process is iterated as such until a predetermined number of endmembers is found. The

fractional abundance maps are then output with the final unmixed set. This method takes considerable time, as there are many unmixing steps involved.

Improvements to IEA have been made since its inception, including: 1) the replacement of the sum-to-one constraint with a weaker abundance sum-to-one-or-less constraint, allowing for better accuracy when all the endmembers haven't yet been found. 2) Changing the endmember search process from sequential forward selection to sequential forward floating selection, allowing selected endmembers to be discarded if necessary. 3) New endmembers are selected not only on spectral extremity but also capacity to characterize other mixed pixels, as determined by a criterion function which depends on the mean and standard deviation of a residual error image.

The IEA algorithm was compared to PPI, ORASIS, and N-FINDR using real-world data, and each algorithm produced similar outputs to each other.[19] The improved version of IEA is compared with the original, showing better accuracy and better spectral similarity to ground truth of real data.[132]

2.3.17 Piecewise Convex Multiple Model Endmember Detection (P-COMMEND)

Piecewise Convex Multiple Model Endmember Detection (P-COMMEND)[77] is an endmember detection algorithm effective in handling non-convex hyperspectral image data. It estimates endmembers, abundance fractions, and membership values (values which determine the relevance of the piecewise convex region) simultaneously. In order to do this, it iteratively minimizes an objective function

$$J = \sum_{i=1}^{C}\sum_{j=1}^{N} u_{ij}^{m}(x_j - \propto_{ij} E_j)\left(x_j - \propto_{ij} E_j\right)^T + \beta \sum_{i=1}^{C}(M \cdot trace(E_i E_i^T) - 1_{1xM} E_i E_i^T 1_{Mx1})$$

Where N is the total number of pixels, M is the number of endmembers in each convex region, α_{ij} denotes the vector of abundances associated with pixel j with respect to model i, E_i is a Mxd matrix such that each row of E_i, e_{ik}, is a 1xd vector representing the kth endmember with respect to model i, 1_{SxT} notation denotes a matrix of size SxT with all the entries being equal to 1,

u_{ij} are weighting terms for the membership x_j in the ith model, m is the "fuzzifier" term controlling the degree to which the data points are shared among the models, C and β. For this equation, the membership values and abundance fractions are both subject to the nonnegativity and sum-to-one physical constraints. As the iterations progress, the values for the abundances and endmembers are updated from their initial (random) values. Once a membership value for a region falls under a certain threshold, that region is removed from further analysis.

2.3.18 Competitive Agglomeration P-COMMEND (CAP)

Competitive Agglomeration P-COMMEND (CAP)[91] is P-COMMEND using the competitive agglomeration clustering technique to estimate the number of convex regions for the input data set. This method of region number estimation is geometrical in nature, whereas the Dirichlet method used in PCE is a statistical method. CAP has been shown to be comparable to PCE in accuracy of endmember determination but with far less time involved for calculations.

2.3.19 Piecewise Convex Endmember detection (PCE)

Piecewise Convex Endmember detection (PCE)[65,76,91] consists of two steps 1) an endmember distribution detection algorithm and 2) a partition of the input data set into convex regions and estimate of the endmember distributions and abundance proportions for each convex regions. The number of regions in this case is determined by using a Dirichlet process, a stochastic probability distribution process whose domain is a random distribution, effectively resulting in an infinite series of random variables with a given marginal distribution.

The advantages to using endmember distributions instead of endmembers is that it allows the incorporation of spectral variation due to inherent variability or environment into an endmember instead of using a single spectrum. It represents the endmembers as random vectors with unique abundance vectors for each pixel. This technique is especially useful when encountering hyperspectral images with highly mixed pixels.

Using the endmember distribution detection algorithm and assuming Gaussian distributions with mean spectra e_k and known covariance matrices V_k, logically, each pixel is a multivariate Gaussian random variable with a distribution defined by a linear combination of the Gaussian distribution of the endmembers.

$$f(x_j|E,p_j) \propto \exp\left\{-1/2\, R^T \left(\sum_{k=1}^{M} p_{jk}^2 V_k\right)^{-1} R\right\}$$

$$R = x_j - \sum_{k=1}^{M} p_{jk} e_k$$

Where E is the matrix containing the mean endmember spectra, M is the number of endmember distributions, and p_{jk} is the jth point's proportional abundance value for the kth endmember. The joint likelihood of all pixels are then assumed to be a product of the individual likelihoods

$$f(x_j|E,p_j) \propto \prod_{j=1}^{N} f(x_j|E,p_j)$$

By this, all points share the same set of endmember distributions, since the endmember properties themselves do not change, but have unique abundance vectors due to having unique Gaussian distributions.

PCE is a technique very similar to the Dirichlet Process Mixture Model (DPMM), as they both largely follow the same psuedocode and use a Dirichlet process to determine vectors. They differ in several ways, including several computational steps and the underlying principle that in PCE, each data point is a random variable with a unique distribution, whereas in DPMM, each data point is assumed to have the same distribution.

PCE was compared to ICE, SPICE, and VCA algorithms and the USGS spectral library for endmember determination. PCE was shown to be better suited to find endmembers for all the various piecewise regions in a scene.[76] It is used successfully to partition real world data for the

R-SPICE algorithm. Its limitations currently include the fact that it doesn't allow for partial membership of data points between convex regions.[65] All endmember distributions also share a constant covariance which may not be optimal, and there remains a long run time due to the limitation of the Gibbs sampler in its processing functions.

2.3.20 Geodesic Simplex Volume Maximization

Geodesic Simplex Volume Maximization[85,133] is an algorithm which reformulates the N-FINDR algorithm in terms of distance geometry, or geodesic distances. Geodesic distances are defined as the shortest-path distances along a K nearest-neighbor graph in a data set. This process involves nonlinear dimensionality reduction in a linear space of reduced dimensionality.

Where N-FINDR searches for the simplex of largest volume in the data set, the volume V of a simplex can be written in terms of inter-vertex distances using a Cayley-Menger determinant

$$V = \sqrt{\frac{\det\left(C_{1,2,\ldots,p}\right)}{(-1)^p 2^{p-1}((p-1)!)^2}} \tag{1}$$

Where

$$C_{1,2,\ldots,p} = \begin{pmatrix} D^2_{1,2,\ldots,p} & 1 \\ 1 & 0 \end{pmatrix} \tag{2}$$

$$D^2_{1,2,\ldots,p} = [d^2_{ij}]_{i,j=1,2,\ldots,p}$$

$$\det\left(C_{1,2,\ldots,p}\right) = -\left(d_1 C^{-1}_{2,3,\ldots,p} d_1^T\right)\det\left(C_{2,3,\ldots,p}\right) \tag{3}$$

And

$$d_1 = (d^2_{1,2}, \ldots, d^2_{1p}, 1)$$

Where p is the number of endmembers (usually chosen by hand), C= , and d= . With (1) and (3), we can derive the orthogonal distance from a point x_1 to the plane spanned by vertices (x_2, …, x_p) of the simplex. Endmember extraction in this case involves 1) a weighted, symmetrical, and connected K-nearest neighbor graph on a data set, random points as initial vertices and 2) calculation of sortest-path distances to all other points using the Dijkstra algorithm, using equation (1) to determine the volume for that simplex. Then 3) a random point x is chosen, and the new

volume is calculated for when any vertex is replaced by it. If a larger simplex is found, step 2) is repeated and all modified matrix identities in equation (3) are recalculated. These steps are repeated until no larger simplex is found. This algorithm outputs vertices and their geodesic distances to all other points, and the inputs are the number of endmembers, p, and the connectivity constant of the nearest-neighbors graph, K (for which a value of 20 has been determined as a good value).

Unlike most convex geometry algorithms, this one can be used to unmix nonlinear data as well, taking the data manifold into account. Expressing a linear technique in terms of distance geometry results in a direct non-linear unmixing algorithm without heavy computational intensity. The abundance fractions then become a simple matter of dividing a smaller volume by the maximum volume, and with formulation through simplex geometry, positivity of the result is assured. If the point x lies inside the simplex, the sum-to-one constraint is also satisfied.

$$\propto_i = {}^{V_i}/_{V}, \text{ with } V = \sum_i V_i$$

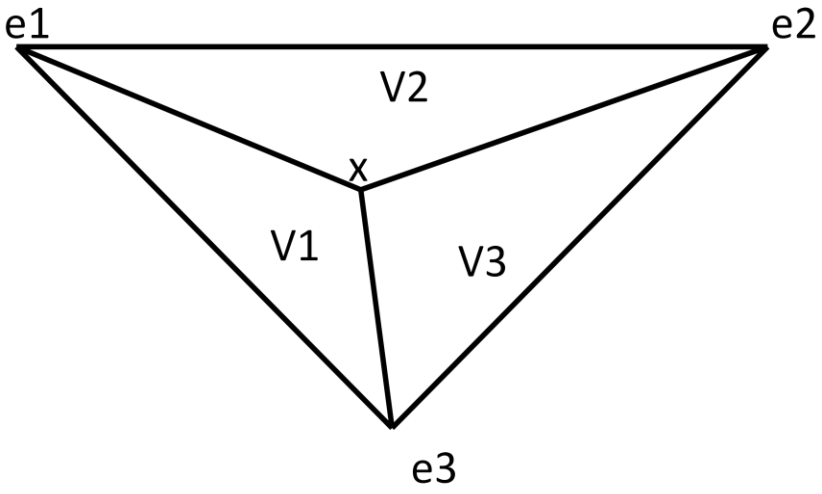

Figure 2.5: Geodesic simplex nonlinear abundance estimation, illustration of dividing smaller volume by max volume when x is chosen as a point inside the simplex formed by 3 endmembers.

The endmembers are represented by e1, e2, and e3, the volumes are represented by V1, V2, and V3, and the arbitrary mixed point is x.

The geodesic simplex nonlinear abundance estimation is less complex compared to other methods such as ISOMAP,[85] only requiring recalculations when a larger simplex is found, and doesn't require segmentation when used on large data sets. It performs better than two-step nonlinear (dimension reduction), then linear (analysis) techniques on real-world data and has fewer computational requirements.

2.3.21 Abundance Guided Endmember Selection (AGES)

Abundance Guided Endmember Selection (AGES)[99] is a technique of endmember detection that calculates pixel abundance fraction values as part of the endmember selection process. Somewhat uniquely, this algorithm considers the non-negativity constraint implicit with so many other linear algorithms to be unnecessary in this case, and excluding that constraint greatly reduces the computation time involved. The first step of AGES involves a PCA transform, and the eigenvectors corresponding to the M largest eigenvalues of the scene covariance matrix are used. A random initial set of pixels are chosen as an endmember estimation S_1, then an image of S is calculated on the reduced PCA space according to

$$\hat{S} = PP^T S$$

The data is then inverted using

$$c_i = u_i - (S^T S)^{-1} 1[1^T (S^T S)^{-1} (1^T u_1 - 1)$$

Where $\hat{S}$ is inserted in place of S, c_i is the additivity-constrained abundance for pixel i, 1 denotes a vector with every entry equaling unity, and u_i is a vector of unconstrained abundances found by

$$u_i = (S^T S)^{-1} S^T x_i$$

Where x_i is the measured spectrum for pixel i. The pixel with the largest magnitude abundance c_{ij} is then found, and if $|c_{ij}| - 1$ is greater than a threshold value, the jth endmember is replaced with image pixel i in the PCA space. This process is repeated from the inversion step if the endmember is replaced until there are no more replacements.

This algorithm can be run multiple times with different initializers, with the largest volume simplex being retained, as with N-FINDR. AGES is compared with N-FINDR with real world and simulated data, and while the quality of results are similar, greater variation is found in the AGES results, but AGES is also found to be computationally faster and cheaper.[99]

2.3.22 Orthogonal Subspace Projection (OSP)

Orthogonal Subspace Projection (OSP)[16,17,27,34,36,57-59,122-124,134-141] is a simple method based on LS principles used for endmember extraction or classification. In classification, OSP breaks down the endmember signature vector into two parts: 1) a desired target spectrum *d* and 2) an undesired spectrum matrix *U*.

$$r = d\alpha_p + U\gamma + n$$

where α_p is the abundance fraction of the target spectrum in a given pixel, n is the noise, and γ is the matrix for the abundances corresponding to *U*. This formulation allows *U* to be eliminated from the signal through use of an orthogonal subspace projector.

$$P_U^{\perp} = I - UU^*$$

$$U^* = (U^T U)^{-1}$$

where U^* is the pseudo-inverse of *U*. When the signal *r* is projected into a space orthogonal to *U*, all contribution *U* makes to the signal is rendered irrelevant, leaving only the desired signature and the noise, which is also suppressed.

$$P_U^{\perp} r = P_U^{\perp} d\alpha_p + P_U^{\perp} n$$

The new signature model is then a standard signal detection problem and can be solved by a simple matched filter in order to create the OSP classifier q_{OSP}^T.

$$MF(x) = d^T x$$

$$q_{OSP}^T = MFP_U^\perp = d^T P_U^\perp$$

The classifier can then be implemented on every pixel to determine the contribution of d.

OSP classification as described requires knowledge of the endmembers, but OSP can also be used for endmember extraction in a separate implementation. Using the method commonly used for representing convex data simplexes, OSP first finds the brightest pixel as the data point farthest from the origin and selects that as the first endmember. The second endmember is the point most orthogonal to the first endmember, the third is the point most orthogonal to both the first and second endmembers, and so on until the expected number of endmembers has been reached.

For Gaussian noise assumptions, MLE and OSP classifiers can be considered identical, with both methods reaching the same conclusion through different mathematics.[134,141] OSP is used for classification on real data with good success.[57,136,137] The same OSP classification method is also used to estimate the number of endmembers by using a residual threshold ratio value as a stopping criterion .[141] OSP outperforms other classification methods and offers greyscale analog images as an advantage to hard classification as with Minimum Distance and Linear Discriminant Analysis (LDA).[136] In endmember extraction, OSP is much faster than N-FINDR.[124] OSP can be coupled with a spatial preprocessing (SPP) algorithm for endmember extraction on simulated data.[139] Compared with other spatial processing techniques, when SPP is used, OSP comes in second to AMEE but better than SSEE on real data.[142] Non-negatively constrained Least Squares (NCLS) is found to outperform OSP for unmixing of chemical and biological spectra,[58] and likewise in parallel implementations of fully-constrained LS (FCLS) on real data.[123]

Projection Pursuit (PP)[16,17] is another major variant of OSP. It functions similarly to PCA, but instead of projecting orthogonal vectors to maximize variance, other "interesting"

vectors are chosen based on a projection index which maximizes the difference between the distribution of the data and a Gaussian distribution.

There are many other related algorithms which use OSP as a base, including the a posteriori Least Squares OSP (LOSP),[136,143] Oblique subspace projection classifier (OBC), desired target detection and classification algorithm (DTDCA), automatic target detection and classification algorithm (ATDCA).[136] Noise subspace projection (NSP) is a noise whitening method related to OSP that can be coupled with methods such as VD for estimation of the number of endmembers.[135] A kernel-based version of OSP (KLSOSP) can also be used to good effect.[138]

Further methods such as Orthogonal Bases Algorithm (OBA) and Self-Modeling Curve Resolution (SMCR) are referenced[90] but unexplained. OBA may be another shorthand for OSP, since the term "base" is used by physicists to mean a component of a mixed spectrum, such as an endmember.

2.4 Hierarchical Decision Processes

2.4.1 Support Vector Machines (SVMs)

Support vector machines (SVMs),[31,144-151] in the simplest form, are pattern recognition devices that use binary decision-makers in pixel classification of hyperspectral images. Unlike Bayesian and neural network methods, SVMs use margin-based geometrical criteria rather than purely statistical methods, allowing higher accuracy for fewer needed training samples and discounting the need to calculate the statistical distributions of the training classes. The outputs to be expected from this method are 1) a probability map of the hyperspectral image and 2) identification of sufficiently “pure” pixels according to a defined threshold. This method uses endmembers expected to be found in a scene as training data to formulate the mathematical decision boundaries.

SVMs can be formulated in two ways, 1) a defined architecture made of binary classifiers or 2) directly as multiclass optimization. Either way, the core of the SVM decision-making focuses on finding an optimal hyperplane between two classes. A hyperplane is a linear surface defined by a vector *w* normal to the hyperplane and a bias *b* to separate both classes without error. The discriminant function associated with a linear hyperplane is:

$$f(x) = w \cdot x + b$$

And it is estimated such that

$$y_i(w \cdot x_i + b) > 0\,, \qquad i = 1, 2, \dots, N$$

Where N is the number of vectors in the training set. SVM finds the optimal hyperplane that maximizes the distance between the closest training sample and the hyperplane that separates the classes. This optimal margin can be written as $1/\|w\|$ if the second equation is scaled such that:

$$\min_{i=1,2,\dots N} y_i(w \cdot x_i + b) \geq 1$$

The optimal hyperplane can then be found with either convex quadratic programming or Lagrangian formation dual problem programming. The discriminant function for the optimal hyperplane then depends on the Lagrangian multipliers and training samples:

$$f(x) = \sum_{i \in S} \alpha_i y_i (x_i \cdot x) + b$$

Where S is the subset of training samples which corresponds to nonzero α_i's. The Lagrange multipliers in this case essentially weight the importance of the training sample to determining the discriminant function. The training samples with nonzero weights are termed "support vectors" and lie at a distance of $1/\|w\|$ from the optimal hyperplane.

In the case that the data is not nicely linearly separable as implied above, the math must be generalized further to include error minimization so that false classification is penalized. The cost function is reformulated as follows:

$$\Psi(w,\xi) = \frac{1}{2\|w\|^2} + \mathrm{C}\sum_{\mathrm{i}=1}^{\mathrm{N}} \xi_{\mathrm{i}}$$

Where ξ_{i}'s are "slack variables" representing nonseparability of classes and C is a constant regularization parameter for error penalization such that when C increases, the penalty to miss-classified samples also increases. In this case, there are 2 types of support vectors which exist: margin support vectors which lie on the hyperplane margin and non-margin support vectors lying on the "wrong" side of the margin.

Nonlinear Kernel SVMs: In the case where the discriminant can't be linear, kernel functions are used. These allow the data to be mapped through a nonlinear transformation in to a higher-dimensional feature space to find the optimal hyperplane defined by a vector and bias as described earlier. Kernels used must conform to Mercer's condition (where the double integral of the function must be greater than or equal to zero) to correspond to some type of inner product in the transformed dimensional space:

$$K(x_i, x) = \Phi(x_i) \cdot \Phi(x)$$

Where $[\Phi(x_i) \cdot \Phi(x)]$ are used to denote the higher-dimensional space instead of $(x_i \cdot x)$. Using the kernel method avoids messy computation of internal products in transformed space and results in an expression in terms of the original lower-dimensional terms:

$$f(x) = \sum_{i \in S} \alpha_i y_i K(x_i, x) + b$$

The shape of the discriminant is then based on the kernel used, which must satisfy Mercer's condition. Examples include the Gaussian radial basis function and the polynomial function of order *p*. Parameters for which kernel function and C must be chosen, though there are optimization methods to estimate these parameters which 1) maximize the margin and 2) minimize the generalization error.

Multiclass SVM strategies allow for simultaneous discrimination of numerous classes, and there are two steps in the general approach to doing so: 1) definition of a set of binary classifiers, and 2) combination of the classifiers in an architecture according to the experiment's decision rules. Two main multiclass approaches exist, parallel and hierarchical tree methods.

Parallel approaches involve each SVM solving a 2-class problem defined by one class against all others or generating all possible class pairs and comparing them at once. Using a binary hierarchical tree (BHT) based approach breaks the decision process into nodes where each individual decision is made, thus reducing the overall number of decisions and the computation time needed versus parallel methods.

2.4.2 Neural Networks (NN)

Neural Networks (NN),[23,49,56,113,120,121,149,152-159] also referred to as Artificial Neural Networks (ANNs), could be considered a familiar concept to anyone with knowledge of physiology. As in the nervous system of any living being, ANNs are composed of small units called neurons, or nodes, linked together in a specific topology or framework. In this case, the neurons are low-level mathematical equations or processes instead of cells, arranged in a minimum of three layers: one for the input, one for the output, and at least one hidden layer. Links between neurons from one layer to the next can be assigned weights in order to control the impact of values from one unit to another. ANNs can be general-purpose and scale better than many other methods due to the low complexity of each neuron. They are learning methods that can avoid parametric models where the parameters need to be known ahead of time. As such, often prior knowledge of a specific HSI image isn't needed, and the ANN figures out whatever it needs as it learns. The learning process can streamline the ANN algorithm from the initial framework, turning off or discarding unneeded neurons and making subsequent uses of the algorithm faster for the same sort of data set. ANNs are extremely customizable and are often used in conjunction with other algorithms for all different parts of the HSI analysis process. There

are many types of ANNs, and only a few are covered here as examples of what is currently reported in HSI literature.

A subset of NN is Adaptive Neural Networks, which contain nodes that depend on parameters (adaptive nodes) in addition to ones which require no parameters (fixed nodes). In networks like these, initial parameters can be set, then updated later by a backpropogation method according to a learning device such as least squares estimation and gradient descent.

Adaptive-Network-based Fuzzy Interface Systems (ANFIS) is an adaptive NN technique which takes advantage of fuzzy systems easy interpretability and ANN learning and minimal parametric requirements for a Neuro-Fuzzy technique which produces more meaningful answers than ANN alone. It contains five layers of ANN, including fuzzification and de-fuzzification processes.

Use of Gaussian functions as synapses instead of simple sigmoidal functions to connect one layer to the next allow for more efficient network formation. Gaussian and other radial functions are usually used as basis or activation functions, which constrains those networks to linear regression and optimization of the synapse weights. Networks with Gaussian functions as synapses are trained to recognize only one endmember and ignore any others, discarding irrelevant nodes instead of deactivating them. Training ANNs with Gaussian synapses takes longer than building other ANNs, but the subsequent analysis rates are faster because there are no unnecessary nodes to compensate for irrelevant information. They're related to multiple layer perceptron filters, except the hidden and output layers are different. Three layers are generally sufficient, provided there are enough nodes. The size of the input layer typically corresponds to the number of bands, and the size of the output layer corresponds to the number of endmembers.

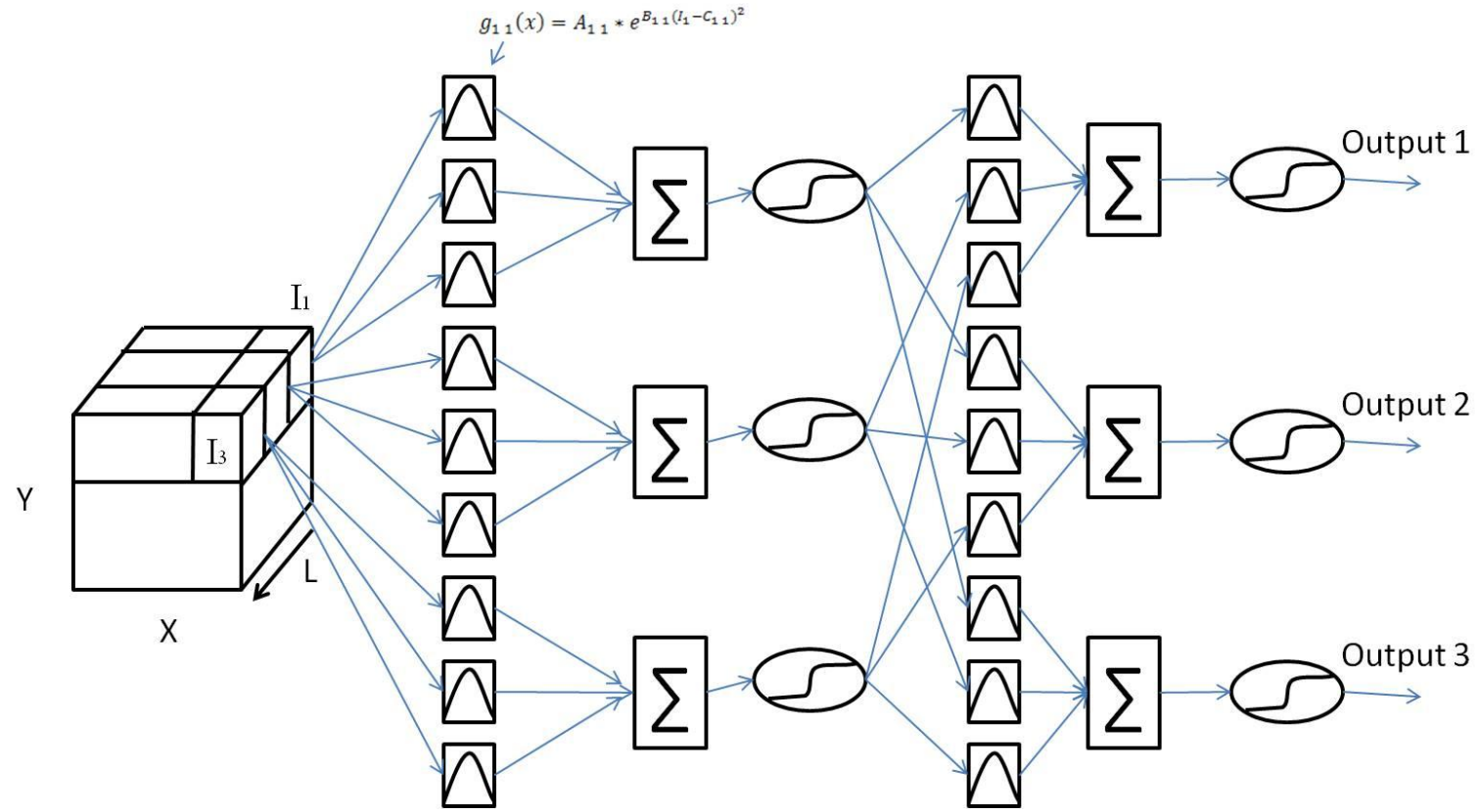

Figure 2.6: Schematic of a sample ANN with Gaussian synapses and sigmoidal activation functions. Nodes are summations.

The Gaussian synapses are determined by three parameters: center (C), amplitude (A), and variance (B).

$$g(x) = A * e^{B(x-C)^2}$$

Using this synapse equation for Gaussian Synapse Backprojection (GSBP), the gradients and variation error with respect to A, B and C must be found, and traditional recursive backprojection follows, such as with gradient descent.

Lagrangian-Hopfield ANNs (LANNs) share the sum-to-one constraint that constrained LS uses, but that constraint is relaxed through the use of Lagrangian multipliers. LANNs are used for the blind source separation problem, i.e. when both the endmembers and their abundance fractions in a pixel are unknown. These 4-layered ANNs use Lagrangian multipliers and the constant maximum entropy of the data (derived from the endmembers) to make measurements like the Hopfield energy function. Since there are two unknowns, this network involves two recursions, iterating one after the other, much like ICA.

The largest disadvantage to ANNs is that they are learning algorithms, and as such they need a training set for the data. Advanced ANNs may only require an unrelated image with the necessary endmember information, but others require more specific information. This is a problem when there is a lack of prior information about a data set, as such prior knowledge is often nonexistent. In this light, it is advantageous to use ANN algorithms which only require very small training sets.

ANNs are used to identify endmembers so that another process can unmix them.[160] The hybrid ANFIS is used in multispectral imaging to produce very accurate bathymetry results superior to other techniques used on the same data.[153] Gaussian synapses are used to aid in network formation through training in order to segment real hyperspectral and multispectral images into pure-pixel and mixed-pixel areas.[154] Gaussian synapse ANN are expanded to quantify endmembers in spectral unmixing,[155] and further to detect those EMs while unmixing them.[158]

ANNs can also be used for image classification using bands selected by a genetic algorithm.[120] ANNs are also used to enhance the resolution of real and simulated images after endmember extraction and unmixing, respectively.[49, 56, 121, 159] Lagrangian-Hopfield ANN (LANN) are used for subpixel classification in real images, with some speculation it could be used for anomaly detection as well.[23]

2.4.3 Evolutionary Algorithms

Evolutionary Algorithms[160] happen when math meets Darwinism. They evolve solutions to complex math and pattern recognition by taking existing algorithms and randomly interchanging equivalent internal logic the way DNA exchanges genetic material upon cell replication. When the resultant generation is evaluated with a user-defined cost function, the failures are discarded, leaving only the successes for a survival of the fittest paradigm. The overall best algorithm is tracked through a set number of generations, eventually becoming the optimal algorithm. In these ways, Evolutionary Algorithms use concepts from various other methods including Genetic Algorithms, Genetic programming, and ANNs.

Evolutionary Algorithms have seen use in the spectral unmixing problem of hyperspectral imaging to replace standard unmixing methods. Advantages include the ability to handle many model types, including linear and nonlinear, broader adaptability than the gradient descent approach, fine level discrimination between highly correlated spectra, and easy scalability for large numbers of endmembers, among others. There are several disadvantages as well, including the need for training data and user-defined input for things such as cost functions. They also require a preprocessing step to calibrate and normalize the data as well as a trained ANN (or similar function) process to identify the endmembers, so as of yet cannot handle the entire endmember identification and spectral unmixing process without aid.

Evolutionary Algorithms are used in conjunction with signal preprocessing to normalize and smooth the signal and an ANN identification subsystem to find endmembers.[160] The

Evolutionary Algorithms present good solutions to real data for conditions as disparate as airborne geological remote sensing and biological tissue as viewed through microscopes.

2.5 Statistical Methods:

2.5.1 Independent Component Analysis (ICA)

Independent Component Analysis (ICA)[38,68,113,118,133,161-167] assumes that abundances are random signal sources instead of fixed constants as other methods do. It differs from PCA in several regards, including the use of higher order statistics than 2nd order, the components are not necessarily orthogonal, it needs a linear model to describe the data, and independence is a stronger statistical condition than non-correlated. The algorithm itself when used for spectral unmixing solves for random abundance fractions and doesn't require prior knowledge of the endmember matrix. It follows the assumptions that 1) the endmembers are linearly independent, 2) the number of endmember abundance fractions are mutually statistically independent, and 3) only one of the endmembers can possess a Gaussian distribution. As a result of the minimal information that ICA works with, it doesn't estimate the signal strength, making it useful for signal detection or classification, but not for quantification.

In order to estimate the abundances, ICA finds a separating matrix of a size corresponding to the number of endmembers by the number of bands used.

$$\hat{\alpha}(r) = Wr$$

Where W is the separating matrix or psuedoinverse of M, r is the hyperspectral data signal, and $\hat{\alpha}(r)$ is the estimated abundance vector based on r. W is not the exact inverse of the endmember matrix and is difficult to calculate, therefore it is estimated through variable methods. The end result is an iterative algorithm to update the W matrix by optimizing a cost function, such as a contrast function to simplify the infomax criterion[161] (maximizes higher order statistics), a

neural network learning algorithm,[162] a negentropy estimation maximization,[163,168] or minimizing mutual information.[165]

Variations of ICA have been developed such as FastICA,[163,168,169] contextual ICA (cICA),[162] and a parallel implementation of ICA (pICA).[169] FastICA is currently the fastest ICA method, breaking the algorithm into two processes: a decorrelation process which keeps the different weight vectors from converging to the same maximum and a unit process which estimates the individual weight vectors.

The drawbacks of ICA include long computation times, many iterations, no quantification of signals, and reduced accuracy the lower the SNR or lower the number of endmembers. Real and simulated data testing show that ICA doesn't unmix all abundances correctly, though it is found that the algorithm performs better with high SNR and high number of endmembers.[161,163]

Spectral screening by use of spectral angle distance (SAD) has been shown to increase the speed of ICA without compromising accuracy.[164] This method reduces the data volume by removing extraneous spectra and forming a subset in which no two vectors are similar according to a threshold value, thereby reducing data that needs to be passed through the algorithm. The results from the data subset can then be applied to the whole data cube. This method was tested and found to work on real data with a threshold value that corresponds to previous similar work with PCA.[164]

Adding the nonnegativity and sum-to-one constraints to ICA produces constrained ICA (CICA) and changes the goal from maximizing independence to maximizing uncorrelation.[165] This method is compared with HOS-ICPA, VCA-FCLS, and MVC-NMF with simulated data where it is found to converge rapidly with relatively few iterations and perform better than the other algorithms. When tested on real data, the CICA algorithm results coincided well with the true endmembers.

As with PCA, ICA can also be used for dimensionality reduction through similar methods to PCA or by guiding band selection.[169]

2.5.2 Complexity Pursuit

Complexity Pursuit[166,167,170] is essentially a simplification of ICA, but instead of maximizing the independence of a hyperspectral data set, it seeks to minimize the complexity. Due to the violation of the inherent source signal (in this case abundance fractions) independence assumption of ICA by the sum-to-one physical constraint, some authors[166,167,170] postulated that this made ICA unsuitable for hyperspectral unmixing. Instead, seeking to minimize the complexity of the signal sources by maximizing their predictability is more feasible and does not violate the sum-to-one constraint. The statistics used are also simpler and easier to implement, involving variance calculations. In addition, since the predictability of source signals lies between the greatest and least of the predictability of all source signals, and as the number of mixtures increases, the difference between the extreme values decrease, this makes it easier to unmix a signal with larger data sets. In cases where the number of bands is far greater than the number of endmembers, this turns the size of the data set into an advantage, hence no dimensionality reduction required.

Complexity pursuit is shown to produce smaller errors in unmixing vs. ICA for real data.[166] Two complexity pursuit algorithms have been established, one that examines spatial complexity from pixel to pixel (spatial complexity BSS, SCBSS), and another that examines both spectral and spatial complexity (spectral and spatial complexity BSS).[167] Spatial complexity characterizes how smoothly one endmember transitions to another over the physical space imaged, using MRF neighbor maps to address correlation. Spectral complexity characterizes the smoothness of the component spectra. Compared against ICA, VCA and CNMF, both algorithms show comparable or better results in simulation and better accuracy with real data.

Disadvantages of complexity pursuit include possible over-smoothing when there may be small targets of interest in the field and the lack of the two major physical constraints normally applied in hyperspectral analysis. Variable neighborhood size is proposed for spatial correlation to address the small target issue and the application of the sum-to-one and nonnegativity constraints to complexity pursuit.[170]

2.5.3 Hierarchical Bayesian Method

Hierarchical Bayesian Method[171-178] uses Bayesian statistics to describe the likelihoods and probabilities that form the abundance matrix in cases where the endmember matrix is assumed known (or derived from an endmember extraction algorithm). In short, the Bayesian subset of statistics infers subsequent events based on previous evidence. For example, if a fisherman wants to find a specific type of fish, he will travel to bodies of water in which he has previously found that type of fish. In order to form the complicated hierarchical function to describe the abundances and their corresponding variances, one starts with a prior probability (prior for short) $p(v)$, which contains information about a vector. The prior is then combined with a likelihood $p(x|v)$ in order to compute a posterior probability, which describes the probability of a vector given the previous information.

$$p(v|x) \propto p(x|v)p(v)$$

If v in turn depends on a variable or vector φ not mentioned in the likelihood, the prior $p(v)$ is replaced by a likelihood $p(v|\varphi)$ and the prior $p(\varphi)$ is found. The hierarchical posterior is then represented as

$$p(v, \varphi|x) \propto p(x|v)p(v|\varphi)p(\varphi)$$

If φ then depends on another variable, $p(\varphi)$ is in turn replaced by another prior and likelihood, and so on.

When applying hierarchical Bayesian statistics to hyperspectral imaging, a posterior joint distribution is generated based on the LMM to describe the abundance matrix and the variances

for each coefficient. A Gibbs sampler is then used to generate samples according to this posterior distribution in an iterative fashion, and the abundance vector is estimated by empirical averaging using minimum mean square error (MMSE).

The likelihood function for y, the full mixed signal, generated in this way is

$$f(y|\alpha^+, \sigma^2) = \left(\frac{1}{2\pi\sigma^2}\right)^{L/2} exp\left[\frac{-\|y - M^+\alpha^+\|^2}{2\sigma^2}\right]$$

Where L is the number of wavelength bands of the data, the + superscripts denote that the physical constraints (non-negativity and sum-to-one) have been applied, and $\|x\|^2 = x^T x$, the standard L^2 norm. Different prior distributions for α can be selected, such as a normal multivariate distribution truncated to encompass the simplex space, a uniform distribution, or a Dirichlet distribution, so long as they take the nonnegativity and sum-to-one constraints into account. A prior is also chosen for σ^2 (such as the inverse gamma distribution) which uses two hyperparameters γ and ν, one adjustable and one constant, which can then be integrated out toward the posterior distribution.

$$\sigma^2 \sim \mathfrak{IG}\left(\frac{\nu}{2}, \frac{\gamma}{2}\right)$$

Where γ and ν also have their own priors ρ and φ which are kept purposely vague and adjustable in calculation because not much is known about them.

The posterior distribution of the unknown vector $\{\alpha, \sigma^2\}$ can then be computed from the hierarchical structure

$$f(\alpha, \sigma^2|y) = \int f(\alpha, \sigma^2, \Phi|y)d\Phi \propto \int f(y|\alpha, \sigma^2)f(\alpha, \sigma^2|\Phi)f(\Phi)d\Phi$$

$$f(\Phi) \propto \frac{1}{\gamma}\left(\frac{1}{\sigma_0^2}\right)^{\frac{\rho}{2}+1} \exp\left[\frac{-\varphi}{2\sigma_0^2}\right] 1_{\mathbb{R}} + (\gamma)$$

Assuming α and σ^2 are independent from each other, the hyperparameters σ_0^2 and γ can be integrated out from the multivariate (a.k.a. "joint") distribution, leaving

$$f(\alpha, \sigma^2|y) \propto \left(\frac{1}{\sigma^2}\right)^{\frac{L}{2}+1} \exp\left[\frac{-\|y - M^+\alpha^+\|^2}{2\sigma^2}\right] x[\varphi + \|\alpha\|^2]^{-\frac{\rho}{2}} 1_{\mathbb{S}}(\alpha)$$

The Gibbs sampler, a special case of the Markov Chain Monte Carlo Metropolis-Hastings algorithm which generates samples from a probability distribution of 2 or more variables (a joint distribution), can then generate samples according to this posterior joint distribution. Once this is done, the abundance vector can be estimated by using the minimum mean square error

$$\hat{\alpha}_{MMSE} = \frac{1}{N_r} \sum_{t=1}^{N_r} \alpha^{(N_{bi}+t)}$$

Where $N_{bi}$and N_r are the number of iterations for burn-in initialization and computation, respectively. Appropriate values for N_{bi} are chosen based on the convergence of an MCMC algorithm with different iterations. Once N_{bi} is chosen, N_r can be estimated as the value of the number of iterations that ensures the mean square error of the estimated α compared to a calculated reference $\hat{\alpha}$ is below some threshold.

Hierarchical Bayesian statistical methods are used on both real and simulated data with good agreement to spectrometer-measured ground truth.[171, 173] The method is modified to compensate for noise modeling which unmixes simulated data with greater accuracy than the method which does not take noise into account.[172] The algorithm is further modified to incorporate a reversible-jump MCMC method to estimate the number of endmembers in real data.[173,177] The hierarchical Bayesian method is extended to perform endmember extraction as well as abundance estimation, turning it into a BSS solution and providing the additional advantage of confidence intervals to the endmember matrix. This method is found to be more accurate than two pure pixel endmember extraction methods (N-FINDR and VCA) and achieves good agreement with FCLS.[174]

The Normal Compositional Model (NCM) is an alternative linear model which describes how the data blends together in addition to finding both the endmember spectra and their

abundances.[175-177] The NCM assumes that the pixels are linear combinations of random endmembers with known means as opposed to being deterministic with the LMM. The hierarchical Bayesian model is then re-formed with the new mixture model in mind, and its robustness to the lack of pure pixels in a simulated scenario allows it to perform better than the Bayesian LMM method, FCLS, MVC-NMF, and non-negative ICA. This method can be coupled with a reversible-jump MCMC method to estimate the number of endmembers (signal subspace), and the method performs better than several other subspace size estimators, such as HySime, PCA, and random matrix theory (RMT) among others.[177]

The generalized bilinear model (GBM) is another alternative nonlinear model which accounts for the presence of multiple photon interactions within the terms of the LMM. The Bayesian algorithm is reformulated to reflect the GBM and outperforms the LMM-derived Bayesian method in real and simulated data, with the drawback of added computational complexity.[178]

2.5.4 Markov Random Field (MRF)

Markov Random Field (MRF)[179,180] is a method that models spatial correlations between pixels and unmixes with a hierarchical Bayesian method.[179,180] It is an excellent tool for modeling neighborhood dependence between image pixels, assuming the content of one pixel is related to the content of its surroundings. It is used for characterizing spatial relationships[166] and to assist with spatial complexity BSS.[180]

MRF is closely related to the Markov Chain Monte Carlo (MCMC)[179,180] method which generates samples asymptotically according to a joint posterior distribution of interest. MCMC can jump easily between different subspace sizes, a technique useful for when the number of endmembers is unknown, so samplers must guess the endmember matrix and abundance matrix sizes. It then iterates to match the correct dimensions to the data. MCMC is also called hybrid Gibbs, since it uses a Gibbs procedure to calculate distributions.

MCMC consists of four steps, updating the endmember matrix means, updating the abundance vector, updating the variance, and updating a hyperparameter used in the variance calculation. Step 1) increases or decreases the number of endmembers based on "birth" and "death" probabilities or replaces one spectrum in the endmember matrix with another from the library according to a "switch" probability. Acceptance probabilities of this step depend on the probability density functions (pdf) of a beta distribution added to the full abundance vector and the number of endmembers. Step 2) is a logical proceeding from the Bayes' theorem.

$$f(\alpha|y,R,\sigma^2,M) \propto \frac{1}{[\sigma^2 c(\alpha)]^{1/2}} \times \exp\left(-\frac{\|y-\mu(\alpha)\|^2}{2\sigma^2 c(\alpha)}\right) 1_{\mathbb{S}}(\alpha)$$

Where α represents the abundances, y is the mixed input, σ^2 is the variance, M represents the endmembers, and μ represents the endmember means from step 1). Step 3) updates the noise variance using a conditional distribution with an inverted Gamma distribution.

$$\sigma^2|y,R,\alpha,M,\delta \sim \mathcal{IG}\left(\frac{L}{2}+1, \frac{\|y-\mu(\alpha)\|^2}{2c(\alpha)}+\delta\right)$$

Step 4) updates the hyperparameter using a Gamma distribution, where the first entry in the distribution function is the shape parameter and the second is the scale parameter.

$$\delta|y,R,\alpha,M,\sigma^2 \sim \mathcal{G}\left(1, \frac{1}{\sigma^2}\right)$$

This formulation of MCMC was tested on simulated data[179] with promising results. Of note, for that situation, the LMM model was deemed inappropriate, so a normal compositional model (NCM) was used.

2.5.5 Expectation Maximization and Maximum Likelihood

Expectation Maximization and Maximum Likelihood (ML or MLE)[134,181,182] are statistical tools often used in conjunction for a number of hyperspectral algorithms including Stochastic Expectation Maximization (SEM), Expectation Maximization Maximum Likelihood (EMML), and Dependent Component Analysis (DECA). Expectation Maximization determines the

estimates of hidden parameters, such as maximizing an expectation equation based on a probability, while ML finds exactly what it sounds like it would find: the maximum of a likelihood based on a probability.

Used with the stochastic compositional model (a generalization of LMM and GMM which describes each observation vector as a linear combination of normally distributed random vectors), these methods may be employed for specific target or anomaly detection and are shown to have a lower false alarm rate those based on LMM and GMM.[182]

2.5.6 Dependent Component Analysis (DECA)

Dependent Component Analysis (DECA)[102,183] is a method based on ICA meant for highly mixed data in which it is not possible to find a minimum volume simplex. This statistical method is based around the abundance fractions modeled as mixtures of Dirichlet probability densities which by their nature enforce the physical nonnegativity and sum-to-one constraints.

2.5.7 Gaussian Mixture Model (GMM)

Gaussian Mixture Model (GMM)[22,182] is a technique used to identify anomalies within a hyperspectral image, pixels which share little to no spectral similarity with the pixels surrounding it. It models the background (non-anomalous) area of the image by a summation of weighted Gaussian distributions as

$$p\big(s(x)\big) = \sum_{c=1}^{C} \omega_c N_{\bar{s}_c, V_c}(s(x))$$

where s is the measured spectrum, $\bar{s}$ is the mean spectrum, and V is the spectral covariance matrix. It uses Stochastic Expectation and Maximization (SEM) clustering to estimate the , V_c, $\bar{s}_c$, and ω_c parameters. This model is not very robust and can fail to provide any solution.[22]

2.5.8 Associative Morphological Memories (AMMs)

Associative Morphological Memories (AMMs)[38,113,156,157,184] or Autoassociative Morphological Memories is a learning pattern recognition technique related to ANNs. In hyperspectral imaging, it is used to segment images and determine endmembers, including the number of endmembers present, with the assumption that the endmembers in a convex data set are morphologically (spectrally) independent. In cases where shape of target in an image is important, AMMs can also be used for shape detection. AMMs is based upon Hopfield Neural Networks, using a lattice structure framework instead of an algebraic structure.

AMMs is selectively sensitive to noise. When noise is of a dilative nature, increasing the observed signal versus the original, or an erosive nature, decreasing the observed signal versus the original signal, the patterns can be defined, stored, and extracted for use later. If noise is a mixture of erosive and dilative, the pattern cannot be retrieved. Fixes to robustness have been proposed including kernel methods.

Endmembers that have already been detected are used to build erosive and dilative memories. Each spectral vector is examined, and if the new vector is not related to any of the stored endmembers, the new vector becomes a new endmember and is stored for reference. True endmembers will be morphologically independent in both the erosive and dilative senses simultaneously.

AMMs is compared to ICA and CCA for shape recognition and proven superior.[38] AMMs is commonly used for endmember extraction and estimation of the number of endmembers in real[156, 157, 184] and simulated[113] hyperspectral images, showing an aptitude for discriminating spectrally similar materials, such as different types of vegetation.[184] AMMs is compared with CCA[113,157] and ICA[113] where it consistently outperforms CCA and outperforms ICA because the simulated images are Gaussian, therefore ICA can only find one endmember. Such a scenario is highly unlikely in real images.

2.5.9 Nonnegative Matrix Factorization (NMF)

Nonnegative Matrix Factorization (NMF)[69,119,129,185-196] or Positive Matrix Factorization (PMF) is a simple concept heavily based on the linear mixture model. It takes the positive signal matrix, the collected hyperspectral data cube without noise, and decomposes it into the product of two positive matrices, i.e. the endmember matrix and abundance fraction matrix. In the standard NMF procedure, only the nonnegative constraint is implied, but in the variation of constrained NMF (CMNF) the sum-to-one constraint is also imposed on the abundance matrix. NMF is often formed as an optimization problem which can be used by different optimization algorithms. The several optimization techniques can be used, including the Gauss-Sidel method or Lim-PG, but in general they alternate which matrix they solve and which it is holding constant, first holding the endmember matrix constant while using FCLS or PCLS to solve for the abundances. They then hold the abundance matrix constant while the endmember matrix is updated using multiplicative updating rules of positive matrices or simply another PCLS.

$$\hat{S}, \hat{A} = \arg \min_{S_{ij} \geq 0, A_{ij} \geq 0} \|X - SA\|_F^2$$

Where $\| \quad \|_F$ indicates the Frobenius norm, X is the signal matrix, S is the endmember matrix, and A is the abundance matrix. The optimization continues until some stopping criterion is reached, estimating both the endmembers and abundances in a simultaneous output. CNMF is tested against PPI and found to perform better, finding non-pure-pixel endmembers as well as the ones in pure pixels.[119]

While NMF is simple in concept, it has a few drawbacks, including degenerated solutions and nonconvexity limitations as well as sensitivity to endmember initialization. Several methods have been implemented to improve the NMF algorithm, most of which include some sort of regularization or novel optimization to improve accuracy or robustness. These methods include higher order estimations with nonnegative Tucker decomposition (NTD or high order NMF, HONMF) which are tested on real and simulated data successfully.[186] Particle swarm

optimization[185] is tested with CNMF in between iterations, and it performs better than CNMF on its own with random initialization or VCA estimate initialization.

Minimum Volume Constrained NMF (MVC-NMF) is a formulation of NMF (explained later) which uses minimum volume of the data simplex as a regularization term. It is compared versus smoothness constrained NMF (SCNMF) and projected gradient NMF (PGNMF) as well as VCA paired with FCLS on synthetic data.[190] Of the tested algorithms, MVC-NMF produces the most stable and accurate estimates. When tested on real world data, MVC-NMF is shown to extract highly mixed endmembers, even if they are present in only a small area of the data image.

Dispersion is suggested as a regularization function and Lin-PG for optimization in an algorithm called minimum dispersion constrained NMF (MiniDisCo) which solves the problem such that the endmember spectrum output has minimum variances with peaks and sharp variations preserved.[187] It compares MiniDisCo against DECA and three other formulations of NMF using different regularization including MVC-NMF, and was found to perform better in simulations and comparable to a VCA-initialized MVC-NMF for real world data. It is also found to be more robust to the estimated number of endmembers, finding flat spectra, and a low number of observed pixels.

MiniDisCo acquires a spatial regularizer in addition to its spectral constraint for an algorithm called MDMD-NMF.[188] Unlike other NMF algorithms, MDMD-NMF estimates the number of endmembers in its process, so that information is no longer a required input or source of error. It is compared to MiniDisCo, VCA, and MD-NMF which uses only the spatial regularization, with simulated data and favorable results.[188]

2.5.10 2-Dimensional Wavelet Transform (2-DWT)

2-Dimensional Wavelet Transform (2-DWT)[29,63,197-202] is a data compression technique (such as with JPEG images) used in hyperspectral imaging to break a full data cube down into a smaller number of blocks represented by coefficients that are easier to process than the full data

cube. The blocks can then be searched for desired targets and unmixing can be performed on the wavelet coefficients created. The wavelet transform can then be reversed to find the exact position of the target in the original image. Wavelet decomposition can also be considered for estimation of the number of endmembers, also called subspace identification.[63]

Expanding the two-dimensional method to three dimensions, the Hyperspectral Discrete Wavelet Transform (HSDWT) can be used to target recognition and extraction or simply data compression[198] before use with some other algorithm such as ICA.[197] HSDWT, a variation on the three-dimensional DWT, reasonably assumes the spatial dimensions are independent of the spectral dimension and therefore transforms the spatial and spectral dimensions separately.

There are many types of wavelet transformations which can be used with hyperspectral data including the Haar transform (integerized version being the S transform for "sequential),[199,200,202] generic lifting transforms,[200] high-pass coefficients, low-pass coefficients, and Walsh (or Haar wavelet packet) functions.[29] Different packets have shown to be useful in different situations,[29] and all wavelet transform methods mentioned above have been shown useful in simulated sparse data.

Implementation of the S transform in one dimension is fairly simple and can be generalized to more dimensions. A signal of length N is taken and separated into even and odd numbered sequences where $x_0[n_1]=x[2n]$ and $x_1[n_1]=x[2n+1]$. Low-pass and high-pass filtered coefficients from $n_1=[1..N/2]$ are produced as follows.

$$y_1[n_1] = x_1[n_1] - x_0[n_1]$$

$$y_0[n_1] = x_0[n_1] + \left\lfloor \frac{y_1[n_1]}{2} \right\rfloor$$

Where $\lfloor a \rfloor$ is the largest integer smaller than a, or floor operator and the x values are components of the known data matrix. Expanding the 1-D transform to hyperspectral data involves performing 1-D transformation on the spectral dimension, then 2-D transformation on

each 2-dimensional image for each band. The data to be evaluated then goes from a size of M x N x L for the original data cube dimensions to $M/2^m$ x $N/2^m$ x $L/2^n$ for the created subset. Inverting this process simply involves solving the equations above in reverse order for $x_0[n_1]$ and $x_1[n_1]$ and results in the location of the y coefficients of interest. In particular, $y_1[n_1]$ coefficients will be large where the original signal sees sharp discontinuity, denoting an anomaly or target of interest in hyperspectral applications.

While wavelet transforms may be fast, simple to implement, and allow reversible data compression, they still need signature libraries and generally use least squares for unmixing. The main applications of wavelet transforms are to simplify data for use by other algorithms or detecting and locating known targets as with the hyperspectral dimensional wavelet transform (HSDWT) used to good effect to unmix simulated images[199,200,202] These transforms also perform better with higher resolution data sets (16-bit and higher).

2.5.11 Matched Filtering (MF)

Matched Filtering (MF)[110,111,203,204] is a simple method which creates abundance maps through partial unmixing. Using reference spectra, it searches for only target endmembers while covariance statistics of the data cube are calculated in order to suppress the background of the image, or everything that is not the endmembers of interest. Each pixel is then compared to the reference spectra, outputting a grayscale image for each endmember corresponding to the relative abundance found in the data. This is the unmixing method used in the ORASIS method. It is good for quick recognition and classification, but not for quantification.

Mixture tuned matched filtering (MTMF) is a variation of MF which adds an infeasibility score and image to MF, where high infeasibility corresponds to the mixture between the background and target spectra being unlikely.[203] This method serves to reduce false positives from the MF abundance maps alone. A correctly matched pixel would have a high MF score

(abundance) and a low infeasibility score. This method requires dimensionality reduction on both the data and reference spectra, specifically MNF.

A simpler variation of MF, Spectral feature filtering (SFF)[111,203] specifies a range of wavelengths within which a unique spectral absorption feature exists. It then compares every pixel of a hyperspectral image to the reference spectra in a least squares sense, allowing the recognition of a spectrum by its shape and location of its peaks.

Due to its simplicity and non-iterative nature, MF lends itself very well to parallel processing on massive scales, such as time-resolved flash hyperspectral astronomical data.[204] MF and MTMF are compared against simple normalized difference imaging (NDI) and spectral feature filtering.[203] NDI, while simple, is largely only useful for spectral screening, since it only takes two bands into account. Since only one endmember was of interest in this case, the method with the least computation involved, SFF, was determined to be the most efficient,[203] but MNF-using methods were able to determine the location of anomalous targets. It is apparent that the number of endmembers to be searched for is important. When only searching for a few out of many, MTMF is useful, but with complete unmixing, LS and SAM outperform it.[111]

MTMF can also be used in a co-registration process between hyperspectral imaging and multispectral imaging to create images with high spatial and spectral resolution.[110] Unfortunately the availability of multi- and hyperspectral imaging of the same areas prohibits this usefulness.

2.5.12 Kalman Filtering (KF)

Kalman Filtering (KF)[205-208] is an adaptive linear filtering method which can be applied to several areas of hyperspectral analysis, including abundance estimation and endmember extraction, though not in a simultaneous process. KF by itself is a minimum mean square estimator with two specific features: 1) a state-space concept which allows processing a system as a whole instead of individual components in series, and 2) a recursive nature which updates the current estimate of the state based on the current input data and estimate. This necessitates the use

of two equations: a measurement equation to output the desired values and a state equation which tracks changes in the vector and predicts new state vector values.

This state vector can't be observed directly, so must be estimated. The Linear Unmixing Kalman Filtering (LUKF or KFLU) method estimates the abundance *a* as the state vector

$$a(n+1) = \Phi(n+1, n)a(n) + v(n)$$

where $\Phi(n+1, n)$ is an MxM transition matrix using a Gauss-Markov model, assumed as the identity matrix, and $v(n)$ is a zero-mean white process representing state error. This means that $a(n+1)$ is based solely on $a(n)$ in this model. The noise is not ignored, however, as estimating it correctly in both the state and abundance equations can change the stability of this solution.

The abundance measurement at time *k* can then be estimated

$$\hat{a}(k|k) = \hat{a}(k|k-1) + K(k)[r(k) - S\hat{a}(k|k-1)]$$

Where $r(k)$ is the observed data point at time *k*, S is the nxm matrix which represents the relation between the observed value $r(k)$ and state value $a(k)$ (i.e. the endmember matrix), and $K(k)$ is the Kalman gain.

$$K(k) = [P(k|k-1)S^T][SP(k|k-1)S^T + R(k)]^{-1}$$

where $P(k|k)$ is the error matrix at time *k*

$$P(k|k) = [I - K(k)S]P(k|k-1)$$

In this process, the initial conditions for $\hat{a}$ and P are defined, the measurements for $K(k)$, $\hat{a}(k|k)$, and $P(k|k)$ updated, and then the abundance updated. The predictions for the next time point are then updated, including the abundance state and the covariance matrix for the error term, which plays a part in $\Phi(n+1, n)$, the Gaussian-Markov process term.

Kalman Filter-based Spectral Signature Estimator (KFSSE) uses similar principles to LUKF, but operating along a different dimension of the data cube. Whereas LUKF operates pixel-

by-pixel along *x* and *y* to determine abundance, KFSSE operates along the band or wavelength direction to examine one-dimensional endmember signatures.

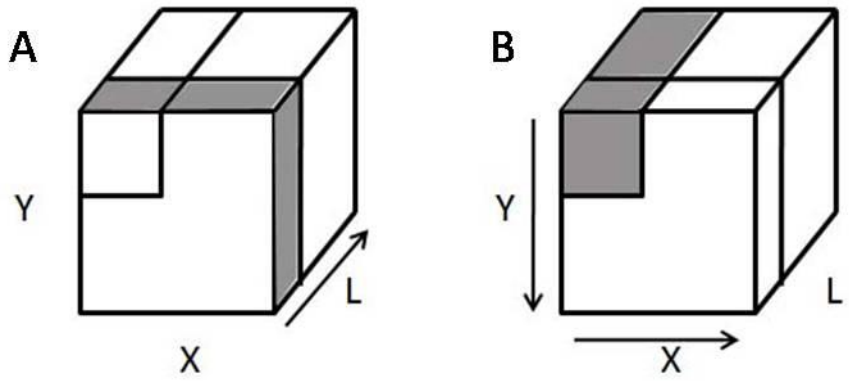

Figure 2.7: Methods for processing with Kalman Filters. A) describes the wavelength-based technique which proceeds along the L direction (KFSSE) and B) describes the pixel-by-pixel abundance analysis method which proceeds along X and Y (LUKF).

KFSSE uses the observed spectral signature values of the pixel vector for its measurement equation and the true spectral signature in the state equation. The measurement and state equations, respectively, are then:

$$r_l = c_l t_l + u_l$$

$$t_{l+1} = \Phi(l+1, l) t_l + v_l$$

where t_l represents the unobservable "true" spectral signature, r_l represents the observable signature, c_l is the relationship vector between *r* and *t*, and u_l and v_l are the measurement and state error. Subscript *l* denotes the wavelength index number. The relationship between one wavelength value to the next is modeled as the $\Phi(l+1, l)$ Gaussian-Markov process term. This Kalman Filter method can also be called Kalman Filter-based Hyperspectral Signature Estimation (KFHSE).[207] Another variation of KFSSE is Kalman Filter-based Spectral Signature Identifier (KFSSI)[208] where the true signature vector is replaced with an auxiliary signature vector from a spectral library which enables signature matching with unknown signatures.

Kalman Filter-based Spectral Quantifier (KFSQ) is a quantification method that can be used in conjunction with KFSSE or KFSSI to find the abundance fractions of the endmembers determined with KFSSE. Essentially, it is LUKF performed with results from KFSSE. KFSQ takes the spectral estimates from KFSSE (*t* vector) as inputs to the measurement equation, and the state equation quantifies the abundance fractions. For this, *t* and *c* in the state and measurement equations for KFSSE are replaced with α_l and the $\Phi(l+1, l)$ term set to 1, resulting in new measurement and state equations respectively:

$$r_l = \alpha_l t_l + u_l$$

$$\alpha_{l+1} = \alpha_l$$

Additionally, spectral discrimination measures can be made based off KFSSE such as Kalman Filter-based Hyperspectral Signature Discriminator (KFHSD) and a ratio-using version, Kalman Filter-based Hyperspectral Signature Ratio Discriminator (KFHSRD). These two techniques use techniques derived from KFSSE in order to measure how different spectral signatures are from one another, much the same way Spectral Angle Mapper (SAM) and similar methods do, but with the capability to determine spectral difference wavelength by wavelength. KFHSD uses the following equations for measurement and state, respectively.

$$t_l = s_l + u_l$$

$$s_{l+1} = s_l + v_l$$

Where *t* is the observed signature and *s* is the matching signature. In this case, the two signatures being compared are *t* and *s*, where the input spectrum is *t* and the output is the estimate of *s*. The least squares error (LSE) is used to determine the closeness of fit between *s* and its estimate $\hat{s}$. Likewise, *t* and *s* can be swapped in the equations in order to gain an estimate for *t*. The LSE for *t* versus $\hat{t}$ added to the LSE for *s* versus $\hat{s}$ determine the discriminatory power of the system. If the discriminatory power is large, this means *s* and *t* are very different from each other. KFHSRD operates in a similar manner, introducing a new variable τ_l to generate a new state

variable $x_l = \tau_l / s_l$. The advantage of this is that the state variable x_l can be immune to the effect of the state error *v*.

LUKF is demonstrated with good, robust results on real and simulated data including hyperspectral and multispectral real data.[205] KFSSE and KFSQ are demonstrated on simulated and real data with good results.[206,208] KFSSI is also demonstrated with real and simulated data.[208] KFHSD and KFHSRD are demonstrated successfully for simulated data.[207]

2.5.13 Kernel

Kernel[24,138,149,209] methods can be applied to any algorithm which uses LMM in order to allow the algorithm to use a nonlinear mixture model by implicitly mapping to a higher dimensional feature space. Nonlinear models are often more accurate than LMM since LMM assumes negligible scattering which a nonlinear model can take into account, enabling it to model a scene more accurately.

In itself, a kernel is simply a small mathematical term which can be substituted for another term in larger algorithms. They are used with LS, OSP, SVM, and other methods. Commonly used kernel types are the polynomial learning machine,

$$(1 + x^T y)^P$$

Radial basis function neural network,

$$\exp\left(\frac{-1}{2\sigma^2}\|x - y\|^2\right)$$

And two-layer perceptron

$$\tanh\left(\beta_0 + \beta_1 x^T y\right)$$

A kernel that identifies the mixture type and performs appropriate unmixing on simulated data has been developed.[209] Also, KLSOSP, KNCLS, and KFCLS kernel methods improve upon their non-kernel counterparts for low-resolution real world data but show no improvement on high

spatial resolution data.[24,138] Meanwhile in various SVMs applications,[149] kernels are used to allow for accurate nonlinear modeling.

2.5.14 Least Absolute Shrinkage and Selection Operator (Lasso)

Least Absolute Shrinkage and Selection Operator (Lasso)[109] is a model-building technique used mainly for finding endmembers, but may also be used for spatial pattern recognition.[244] Lasso is implemented via Least Angle Regression (LARS) which can be thought of as a less computationally intense version of the forward selection search technique. It seeks to minimize the squared error between the true observed spectra and their estimated counterparts, providing desired model terms and coefficients. It starts with two sets of variables: an inactive set populated with all the possible model terms, and an active set which starts empty. Given the observed pixel r, the member of the inactive set which forms the largest squared dot product with r is added to the active set. After this first entry,

$$\hat{r}_k = \hat{r}_{k-1} + \gamma(\hat{r}_k - \hat{r}_{k-1})$$

where $\hat{r}_k$ is built from the unique active member set. The problem then becomes how to determine γ.

$$y_k(\gamma) = r - \hat{r}_k(\gamma)$$

γ must be found so that

$$\left[x_j^T y_k(\gamma)\right]^2 = [z_1^T y_k(\gamma)]^2$$

where z_1 is a member of the active set. An entry of the inactive set that results in the smallest γ is added to the active set. The new LARS estimate is the linear combination of the elements of the active set. This process is repeated until nothing can be added to the active set.

Lasso has one further restriction to LARS so that the sum of the abundance fractions is less than or equal to a value s ($\sum \alpha \leq s, s > 0$). This modification of LARS allows the same computational complexity as a simple LS fit instead of its normal higher complexity. The Lasso condition implies that the jth abundance fraction α_j sign must agree with the correlation between

the jth endmember term m_j and the current residual, checking by seeing if the abundance changes during the current step. If it does, the abundance is interpolated to zero, and no new term is added. Lasso is continued until $\sum \alpha \geq s$ or no terms can be added to the active set.

For the case of positive Lasso, ordinary dot products are used instead of square values, so that

$$x_j^T y_k(\gamma) = z_1^T y_k(\gamma)$$

Lasso is incorporated into a constrained unmixing scheme called Progressive Optimal Regression with Constrained Unmixing of Pixels N-dimensional Energy (PORCUPiNE) where PPI is used to identify potential extreme endmembers, effectively initializing Lasso.[109] It is compared to N-FINDR and SMACC on simulated and real data where Lasso and N-FINDR detect all the endmembers and SMACC miss a few. Lasso also gives the results with the smallest residual.

2.5.15 Genetic Algorithms (GA)

Genetic Algorithms (GA)[47,120] apply genetic concepts from biology to hyperspectral imaging. It is initialized with the generation of a number of "chromosomes" which then undergo selection based on their fitness, crossover based on a probability, and mutation based on a smaller probability than crossover. When an individual from the new generation shows better fitness, it replaces its predecessor in the chromosome set. This process iterates until a stopping criterion is reached.

GA can achieve great accuracy and robustness to noise, but the computation costs are high.

GA is used in parallel with a LS endmember estimation algorithm to determine the fitness of selected abundance fractions in simulated images.[47] GA can also be used for endmember selection with success.[120]

2.6 Spatial-Spectral Associations:

In hyperspectral imaging, most analysis techniques treat the pixels as individual spectra with no association apart from mixing to form a mixed spectrum out of several endmember spectra. Few algorithms make use of the idea that spatially adjacent pixels generally have a higher chance of sharing components than pixels which are not adjacent. This idea can be used for improving the resolution of hyperspectral images, such as with back-propagation ANNs (BPNN)[159] and for extracting endmembers as with SPP, AMEE, and SSEE described below.

Most spatial-spectral techniques search for spectral similarity between pixels, but this search can be reversed to find anomalous spectra which have little or no relation to the surrounding pixels.[22, 210] Many anomaly detection algorithms use this idea, though usually at the expense of other features in the image scene.[22]

2.6.1 Spatial Preprocessing (SPP)

Spatial Preprocessing (SPP)[139,142,210-213] is a preprocessing step to weight the importance of spectra in an area according to its spectral distance from other spatially close pixels, typically a 2-3 pixel radius. It is an independent module that can be applied to a hyperspectral data set prior to endmember extraction algorithm without altering the algorithm itself, guiding the extraction to spectrally homogenous areas and away from anomalous spectra which by definition have no relation to the spectra spatially surrounding them.

In a mathematical sense, the scalar spectral weighting process may be carried out as follows.

$$a(i,j) = \sum_{r=i-d}^{i+d} \sum_{r=j-d}^{j+d} \beta(r-i, s-j) \cdot \gamma(r-i, s-j)$$

$$\gamma(r-i, s-j) = \gamma(X(r,s), X(i,j))$$

$$\beta(i,j) \propto \frac{1}{(i^2 + j^2)}$$

$$\rho(i,j) = (1 + \sqrt{a(i,j)})^2$$

$$X(i,j)' = \frac{1}{\rho(i,j)}(X(i,j) - I) + I$$

Where $a(i,j)$ is the scalar weight, $\gamma(r-i, s-j)$ is the spectral similarity measure between pixels in a certain window size from which r and s are derived, $\beta(i,j)$ is a scalar weight to adjust γ, $\rho(i,j)$ is the per-pixel weighting factor, $X(i,j)'$ is the weighted pixel vector output, and I is the centroid of the data cloud. In terms of convex geometry, SPP alters the simplex for EM detection, with each EM candidate shifted toward the centroid of the data cloud. The spectral similarity measure γ is chosen by the original authors to be spectral angle distance (SAD), though others could potentially be used.

The above is not the only mathematical technique which can be used in SPP. The Watershed Transformation, a topographical technique which views the data in terms of catchement basins (minima/maxima) and watershed lines, has also been explored with simulated data.[213] In hyperspectral imaging terms, pure or homogenous pixels exist in the catchement basins, and mixed pixels are found at the transition areas around watershed lines. In order to use this technique, dimensionality and noise reduction must be used.

Though no literature yet explores it,[210] the weighting towards homogenous pixels used in SPP could also be used to weight for the opposite and find anomalous pixels.

For example, SPP with homogenous clustering is used to enhance OSP on simulated data.[139] SPP is used before implementing OSP, VCA, and N-FINDR for real and simulated data in several applications,[210-212] with all the algorithms experiencing an increase in endmember accuracy. SPP is found to only add 30 sec of computation time to those three endmember extraction algorithms, with the window size parameter affecting it very little.[211] SPP is used with OSP, VCA, N-FINDR, AMEE, SSEE and compared to those techniques without SPP based on SAD between the original image and the reconstructed image, using optimal parameters for each

algorithm.[142] OSP alone is found to be the most accurate closely followed by SPP-OSP, and more distantly by SPP-VCA, SSEE, AMEE, N-FINDR, and SPP-N-FINDR on simulated data. On real data, AMEE is found to be the most accurate followed by SSEE and SPP-OSP. This indicates that not all endmember extraction algorithms benefit by weighting pixels by their spatial association to other nearby pixels, contrary to the two previous SSP-centric articles.

2.6.2 Automated Morphological Endmember Extraction (AMEE)

Automated Morphological Endmember Extraction (AMEE)[59,125-127,142,211,214] is a spatial association technique that uses the morphological principles of erosion and dilation as a way to determine the most pure and most mixed pixels in a given neighborhood. Dilation operators find the purest pixels, while erosive operators find the most mixed. The purest pixels are then assigned an eccentricity value based on the value of spectral distance between that and the most mixed pixel of the neighborhood. This process is repeated iteratively for progressively larger neighborhood areas up to a predetermined stopping size. As with PPI, truly pure pixels are found multiple times. The final set of endmember candidates is found by thresholding a grayscale image produced with the eccentricity values, and growing algorithm is performed to include the regions around the purest pixels to form a median spectrum selected as the endmember. An OSP method may also be used to extract the endmembers from the purest pixels.

AMEE is compared with PPI for endmember extraction on real data.[125] Resulting spectra are found to be comparable, but AMEE holds the advantage in that it is an automated technique, therefore more repeatable and requires less time, which would be particularly advantageous for large datasets. AMEE can be expanded in order to perform parallel implementations of its morphological principles for dimensionality reduction, endmember extraction, and spectral unmixing.[126] The dimensionality reduction is found to be lest distorting than PCA, the endmembers extracted are found to be comparable to PPI and N-FINDR, and the spectral unmixing is found to be accurate, all for real data. AMEE is found to outperform OSP, N-FINDR,

VCA, and SSEE on real data as measured by SAD between the original and reconstructed images,[142] and it is shown to be the fastest of those algorithms on real and simulated data.[211] The impact of vector ordering strategies on spectral unmixing with endmembers extracted by AMEE is explored,[214] finding ordering by cumulative spectral distance between components of each endmember to produce the most accurate results. AMEE is compared with SSEE and a non-spatially associated method of OSP,[59] outperforming both methods on real data. Processing time for AMEE can greatly decrease (by 25x) when implemented on a GPU.[127]

2.6.3 Spatial-Spectral Endmember Extraction (SSEE)

Spatial-Spectral Endmember Extraction (SSEE)[59,142,211,215] is a spatial association technique that uses spatial constraints to improve relative contrast of highly spectrally related endmembers based on their location in an image, reducing the chance of misidentification of spectrally similar materials if they are far away from each other. SSEE uses a spatial search window around every pixel and four mathematical steps: 1) an SVD transform is applied to produce eigenvectors that describe most of the spectral variance. 2) The image data is projected onto the eigenvectors in order to determine a set of endmember candidate vectors. 3) Spatial constraints are used to combine and average spectrally similar endmember candidate pixels by testing to see which similar pixels exist in the surrounding area. 4) The OSP endmember extraction technique is used to finalize the endmember set by testing orthogonality.

SSEE is shown to extract endmembers with subtle spectral differences apart from similar endmembers in a completely different spatial location in real and simulated data.[215] SSEE is also used successfully on real and simulated data where it is found to be less accurate than AMEE, but more accurate than methods which take no spatial information into account in.[59,142,211] SSEE also has the slowest processing time out of those tested algorithms.[211]

2.6.4 Multi-Level Detection (MLD)

Multi-Level Detection (MLD)[33,62] is a complicated strategy with a similar spectral-spatial association paradigm used in multispectral imaging. It involves several steps of target and background clustering via K-means, classification, and unmixing for pixels passed over in the classification stage, but part of the goal of MLD is to reduce the number of endmembers to a value less than the number of multispectral bands, therefore it is impractical for hyperspectral imaging.

MLD is tested for many different target sizes and background types,[33] where a background is the spectra which do not contain any of the target spectra. An adaptive version of MLD allows relaxed conditions for inclusion of spectra into background endmembers and target endmember clusters.[62] Both methods are tested on real and simulated data successfully.

2.7 Anomaly Detection[22,32,94,95,122,133,199,216-221]:

Anomaly detection (AD) is a unique subset of hyperspectral image analysis which searches for anomalous pixels, defined as pixels which do not fit with their surroundings. In hyperspectral images, a pixel can be anomalous in a spectral sense, spatial sense, or both. AD is generally held to be an offshoot of spectral unmixing, as unmixing is usually needed before determining the anomalous nature of the pixel.

There are three major ways of determining a spectrally anomalous pixel.[217] The first method is derived from simplex analysis, where any sample outside the simplex of possible mixtures is an anomaly. The second requires the background to be represented with a Gaussian distribution over the entire image, and anomalies would deviate from this distribution by a certain threshold. The third way is to calculate the statistics of the background in a small region surrounding a pixel of interest (localized detection), where an anomaly would deviate significantly from its immediate surroundings. In general, the Gaussian method is less accurate than using convex geometry, since mixtures of Gaussian distributions aren't Gaussian anymore. Localized

anomaly detection has a major advantage over image-wide Gaussian or convex geometry approaches in that there is little likelihood of a uniform distribution over an entire real image. This would, however, require prior identification of pixels of interest, which may be unnecessary for the other two.

2.7.1 Cueing Hyperspectral Anomalies using Mixture Proportions (CHAMP)

Cueing Hyperspectral Anomalies using Mixture Proportions (CHAMP)[217] combines parts of existing techniques and includes statistical modeling of the endmembers and mixing distributions. It operates under three assumptions: 1) a random vector of abundances follows Dirichlet probability, 2) abundance and endmember vectors are independent, and 3) noise is zero-mean white Gaussian. These three assumptions uniquely determine a probability density function (PDF) of the data with unknown parameters (means and Dirichlet parameters) and known covariance matrices. Using concentric boxes, where the inner box is the pixels being tested and the outer is used to establish a Dirichlet local parameter, the PDF is evaluated for each pixel using numerical integration.

CHAMP is found to produce reliable and accurate performance with very few false alarms and the ability to detect subtle anomalies.[217]

2.7.2 RX algorithm

RX algorithm[122,218,219] is the benchmark for anomaly detection. It compares the spectrum of a pixel with its immediate spatial surroundings, estimating the mean and covariance matrix within an arbitrarily chosen window defining the neighborhood of every observed pixel. The Mahalanobis distance of the pixel spectrum from the center of the pixels in its neighborhood is calculated,

$$\delta_{RX}(r) = (r - \mu_r)^T U^{-1} (r - \mu_r)$$

where r is the pixel reflectance, μ_r is the mean of the pixel vector, and U is the covariance matrix.

A nonlinear version of RX can be achieved called kernel PCA (KPCA), based on PCA and higher order statistics. It maps data to higher feature space, choosing the most effective component for anomaly detection based on high order statistics in a local sliding window. This chosen component is used as the input for the RX detector, and a radial basis function is used for a kernel.

KPCA gives clean anomaly detection maps, but misses targets with no false alarms[219] while RX by itself gives quick results but with worse detection than SOM.

2.7.3 Spectral Unmixing Adaptive Feature Extraction (SAFED)

Spectral Unmixing Adaptive Feature Extraction (SAFED)[133] uses extracted endmembers for a matched filter (MF) set. SAFED is a complete endmember extraction and unmixing algorithm set (with GSVM and ICA) which extracts the target and background from an unmixing result using the endmember set statistics. Viewing the statistics as histograms, target-like spectra tend to have spiky histograms and high kurtosis while background endmembers are more complicated with multimodal behavior. Threshold criteria statistics for the endmember abundances can include kurtosis, mean, variance, full-width half-maximum of the histogram, etc. Any of these criteria allow automatic sorting. Anomalies are located from target-like endmembers and their signals are extracted for MF detection. It's less sensitive to unmixing error since the filter only uses part of the information from the data, but it is critically dependent on the unmixing technique. SAFED gives high detection accuracy with negligible false alarms on simulated data.[133]

2.7.4 Cluster Based Anomaly Detection (CBAD)

Cluster Based Anomaly Detection (CBAD)[218,219] is a broad term used to describe several anomaly detection algorithms which function by grouping pixel spectra into clusters of various classes. CBAD assumes clusters of various classes in an image are represented by several

Gaussian distributions. CBAD techniques tend to overlook subpixel anomalies, so only anomalies of one pixel or more in size can be detected.

Self-Organizing Map (SOM)[218,219] is a CBAD algorithm which considers pixels anomalous when they're not part of any background clusters. It has been used for endmember extraction of background clusters in simulated data, and the anomalies were detected afterward with LMM unmixing.[218] The background classes are searched by robust clustering of a small, randomly chosen subset of image pixels with the assumption that any randomly-picked small percentage of pixels will contain many more background-class pixels than target-class pixels.

Compared to RX, SOM provides better detection with lower false alarm rate, but more slowly.[218] SOM with nonnegative constraints gives better results than KPCA with few false alarms.[219]

Maximum Likelihood and Expectation Maximization may also be used in conjunction with a stochastic compositional model for anomaly detection.[182]

2.8 Summary

To summarize the information presented in the preceding text of this chapter, Table 1 summarizes the algorithms covered and the uses presented in the literature. Satellite/Aerial data is real data taken from an airplane or satellite. Simulated data usually means computer simulated mixture of a field of view using a library of known endmembers, or a physical phantom model, both designed to test the accuracy of unmixing algorithms. Anomaly Detection algorithms are those used to find target spectra which are unexpected in the field of view, and could use either real or simulated data input. If the algorithm has been used previously in a biological application, including tissue phantoms their application is stated in the "Used" column. If the algorithm shows promise for the in vivo CBD application of this study, that is denoted by an "X" marked in the "Potential" column. Important biological references are denoted in the last column. Potential algorithms highlighted in gold are those used subsequently in this study to good effect in order to

differentiate the CBD from its surroundings. More individual variations of algorithms, such as FCLS or the many variations of N-FINDR are not included in this table.

Table 1: Algorithms, their reported uses, and potential for biological applications. Algorithms which show potential for CBD detection and meet with experimental success in subsequent chapters are highlighted in yellow.

	Algorithm Uses			Biological		
Algorithm	Satellite/Aerial	Simulation	Anomaly Detection	Used	Potential	Important References
LS	X	X	X	Human Umbilical Cell Fluorescence Microscopy, Simulated Mixture	X	20-37, 39, 41, 51, 58
CCA	X	X				78, 113
MVT	X					39, 79, 93
AVMAX		X				79, 81
MVES	X	X				75, 82
MVSA		X				114
SISAL		X				102
SR	X	X				103-105
OMP	X	X				103-105
VCA	X	X				83, 88, 94
N-FINDR	X	X	X			18, 19, 99
PPI	X	X				19, 108
ORASIS	X					19, 32
ICE	X	X		Animal ex vivo fluorescence		65-68
MAX-D	X					106-107
SMACC	X	X			X	107, 130
IEA	X					19, 132
P-COMMEND		X				77
CAP	X					91
PCE	X	X				65, 76,91
GSVM	X					85, 133
AGES	X	X				99
OSP	X	X		Simulated Mixture		137
SVMs	X	X			X	144-151

(Continued from Table 1)

NN	X	X	X		X	153-158
EA	X			Cancer Microscopy		160
ICA	X	X				161-169
CP	X	X				166-167
Bayesian	X	X				171-178
MRF		X				179-180
EM/ML	X	X	X			222-224
DECA						90
GMM	X					22, 182
AMMs	X	X				156-157
NMF	X	X		Fluorescence, Tissue Phantom	X	119, 185-196
2-DWT		X	X			197-200
MF	X	X	X		X	137, 203
KF	X	X				205-208
Kernel	X	X				138, 209
Lasso	X	X				109
GA		X				47, 120
SPP	X	X	X			211, 212
AMEE	X	X				59, 125
SSEE	X	X				59, 211
MLD	X	X				3, 62
CHAMP	X		X			217
RX	X	X	X			122, 218
SAFED			X			133
CBAD	X	X	X			218, 219
SAM	X	X		Simulated Mixture	X	58, 74
SID	X	X		Simulated Mixture	X	58, 225

Of the 51 algorithms listed in the above table, only 7 of them have previously been used in biological applications, and only one of those in macroscopic, real data collection environments, where instead of just hyperspectral imaging, it was aided by fluorescence. Despite this, several analysis algorithms in addition to those used in previous examples show promise for quick, timely analysis of biological data in which not every endmember is immediately known. These

algorithms can either calculate the endmembers present in the image (such as SMACC) or take a specified library of non-"pure" spectra and calculate the abundance or indicate the presence of those specified spectra. In particular, SVMs and NNs, though not used before for biological applications were seen to have promise based on their hierarchical decision-making similarity to EA, which has been used before but proved unable to unmix biological data properly without aid. Also MF and its variation MTMF are known to be able to seek a specific spectrum without knowledge of the other spectra in the field of view, which could be very advantageous in a biological setting, but have not been demonstrated on tissue subjects as of yet. SAM and SID are classification metrics of low computational complexity that can also target one or several spectra also without knowing all the spectra in an image and have been used before to determine difference in biological spectra.

Chapter 3

Characterization of a NIR DLP® Hyperspectral Imaging System

Past studies have characterized and tested a DMD-based hyperspectral imaging system in the visible 380 nm to 780 nm range in terms of illumination and detection.[228-230] This chapter illustrates the source and detector characterization of a NIR 760 nm to 1600 nm DMD-based hyperspectral imaging system.

3.1 System Description

In many multispectral and hyperspectral systems that use a CCD or other digital detector, the spectral discrimination is performed through use of narrow bandpass filters in front of the camera lens, whether the filters consist of a mechanical filter wheel or an electro-optical tunable filter such as LCTF or AOTF. The DLP light source enables the narrow bandpass discrimination of light without need for a filter. Instead, light from the 500 W Xenon lamp passes through a slit and is dispersed by a grating, resulting in a rainbow illuminating discrete columns of micro-mirrors on a DMD chip.

Figure 3.1 shows the light path of a DLP hyperspectral imaging system from a broadband lamp to its reflection off an imaging sample and collection by a computer system.

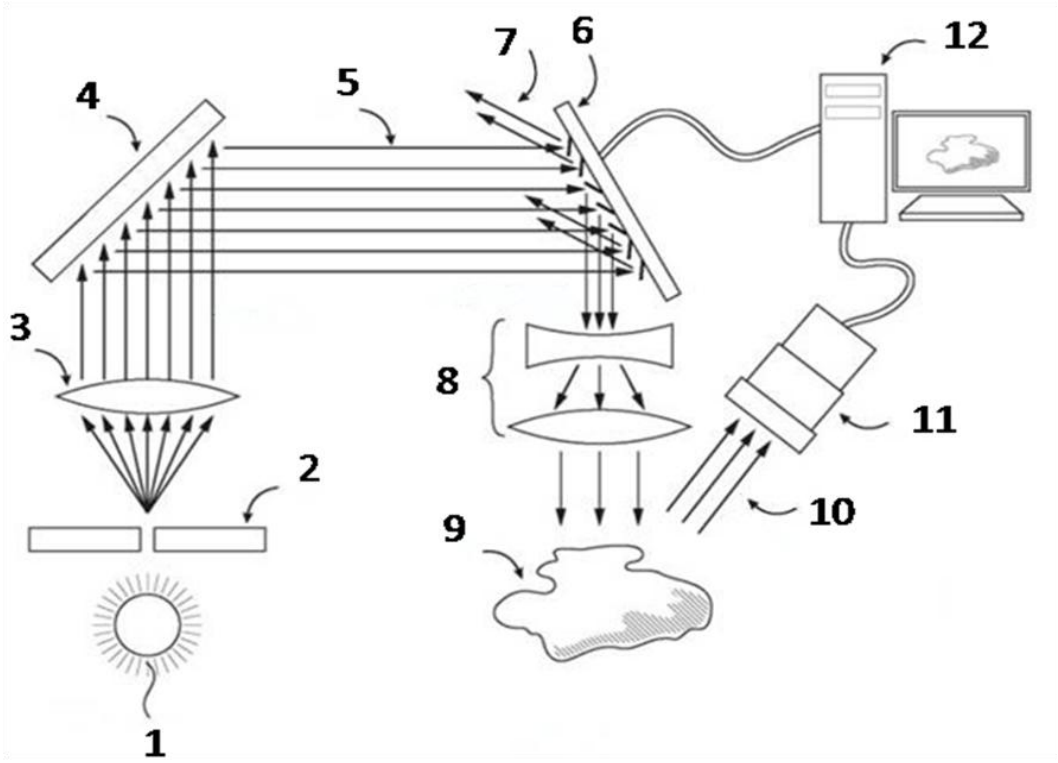

Figure 3.1: Schematic of a DLP hyperspectral imaging system, showing the light path from the broadband lamp to its ultimate collection and analysis by a computer system. Light produced by a broadband source (1) passes through a slit (2) to be collimated and projected onto a dispersion grating (4) which simultaneously illuminates wavelengths of light (5) onto the DLP micromirror device (6). The DLP chip is controlled by a computer (12) to either turn the mirrors "on" or "off, which controls both wavelength and intensity. The "off" mirrors direct the light aimed at them to a heat sink (7), while the "on" mirrors direct the light onwards through the system to a light guide and beam-shaping optic (8) where it illuminates an imaging subject (9). Light reflected from the imaging subject (10) is focused onto a CCD detector (11) and recorded by a computer (12). [5]

The DLP technology utilizes a DMD chip consisting of thousands of tiny micro-mirrors in an array of columns, corresponding to wavelengths. Each column is controllable, so that we can program the number of mirrors in each column that are “turned on,” i.e. angled to reflect the

incident light toward the optics in the system rather than a heat sink. Minute control of the mirrors allows the modulation of both the wavelength and the intensity of light at once.[8,9] In the case of the NIR DLP system, the spectral resolution of the source is 5 nm while that of the visible-range system is 1 nm.

There are four possible slit sizes for use between the lamp and the grating (item (2) in Figure 3.1), ranging from 150 µm width to 750 µm width. Maximum intensity and minimum bandwidth are both directly proportional to slit width, yet spectral resolution is inversely proportional. Lower intensity requires longer exposure times to collect meaningful data, thereby increasing the acquisition time required for smaller fine bandwidths. The maximum intensity of the 500 W Xe source is much lower in the NIR than it is for the visible spectral range, the degree of difference dependent on slit size,[229] therefore NIR acquisition time is greater than in the visible range. While the visible system can collect 126 frames in approximately 25 s to 30 s with a 350 µm slit size, the NIR system requires 65 s or more for 120 frames with the same slit size. Using the 750 um slit reduces the required acquisition time for 120 frames to a more acceptable 25 s. For the NIR system, the 750 µm slit is chosen for characterization and use in surgery in order to maximize the light intensity shown onto the subject, thereby reducing spectral data acquisition time.

Figure 3.2 shows the NIR DLP system as it would appear in the operating room, with the FLIR SC4000 (FLIR Systems, Boston, MA) camera, Nikon Nikkor 55 mm lens, and illuminator supported by a tripod (Moog Quickset, Inc., Northbrook, IL). The camera and OL490 light source (Optronic Laboratories, Inc., Orlando, FL) are synchronized and controlled through a specialized GUI on the controlling computer, which also analyzes the data to produce a real-time image a surgeon can observe in the operating theater.

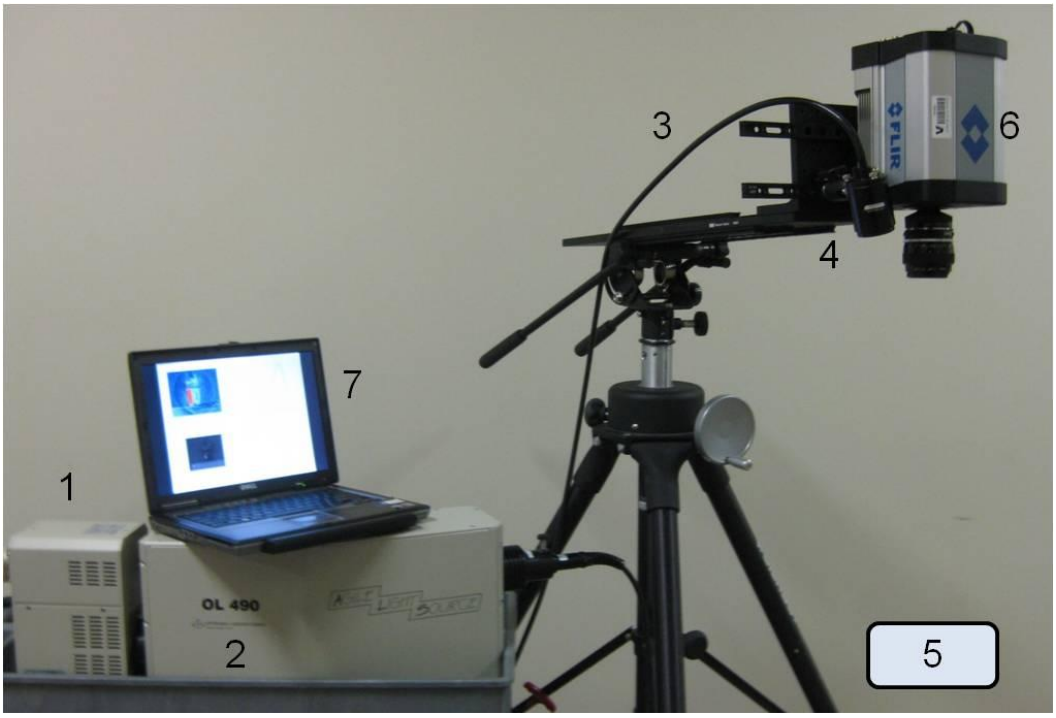

Figure 3.2: The NIR DLP hyperspectral imaging system. Light comes from the Xe lamp (1), through the NIR DLP source (2), through the liquid light guide (3) to the illuminating optic (4) where it shines upon the subject area (5). Reflected light is then collected by the FLIR SC4000 CCD camera (6) and sent to the controlling computer (7).

3.2 Illumination Characterization

The NIR (780 nm to 1600 nm) DLP system is able to illuminate using two different methods, controlled by the OL490 Agile Light Source software. One of these is bandpass illumination, when the projection scheme consists of a series of contiguous bandpasses. Figure 3.3 shows the individual bandpass illuminations with all mirrors turned on and stepped by 10 nm increments for visible and NIR spectrometer ranges. Each bandpass was set to the manufacturer-stated minimum bandwidth of 40 nm for the 750 µm slit.

3.2.1 Illumination Spectral Profile

Illumination spectral characterization is performed by connecting the OL490 light source to a computer with USB cable and controlling it via the installed OL490 software. The 760 nm to 1600 nm LLG was then coupled to the OL490 on one end and a NIR fiber optic cable leading to a spectrometer on the other. Two spectrometers were used to cover the entire range of the system, an Ocean Optics USB2000+ (Dunedin, FL) with a range of 400 nm to 1000 nm for the lower wavelengths and an Ocean Optics NIR512 spectrometer with a range of 850 nm to 1600 nm. Each bandpass illumination was defined by a selected center wavelength and a full-width half-maximum (FWHM) bandpass range then incremented from 760 nm to 1600 nm by 10 nm. The manufacturer reported minimum bandpass for the system while using a 750 um slit size is 40 nm, so that was the FWHM range used. The illumination from each bandpass was recorded individually and plotted (Figure 3.3). To avoid repeating information from the overlap between the two spectrometer ranges, data derived from the NIR spectrometer only will be shown.

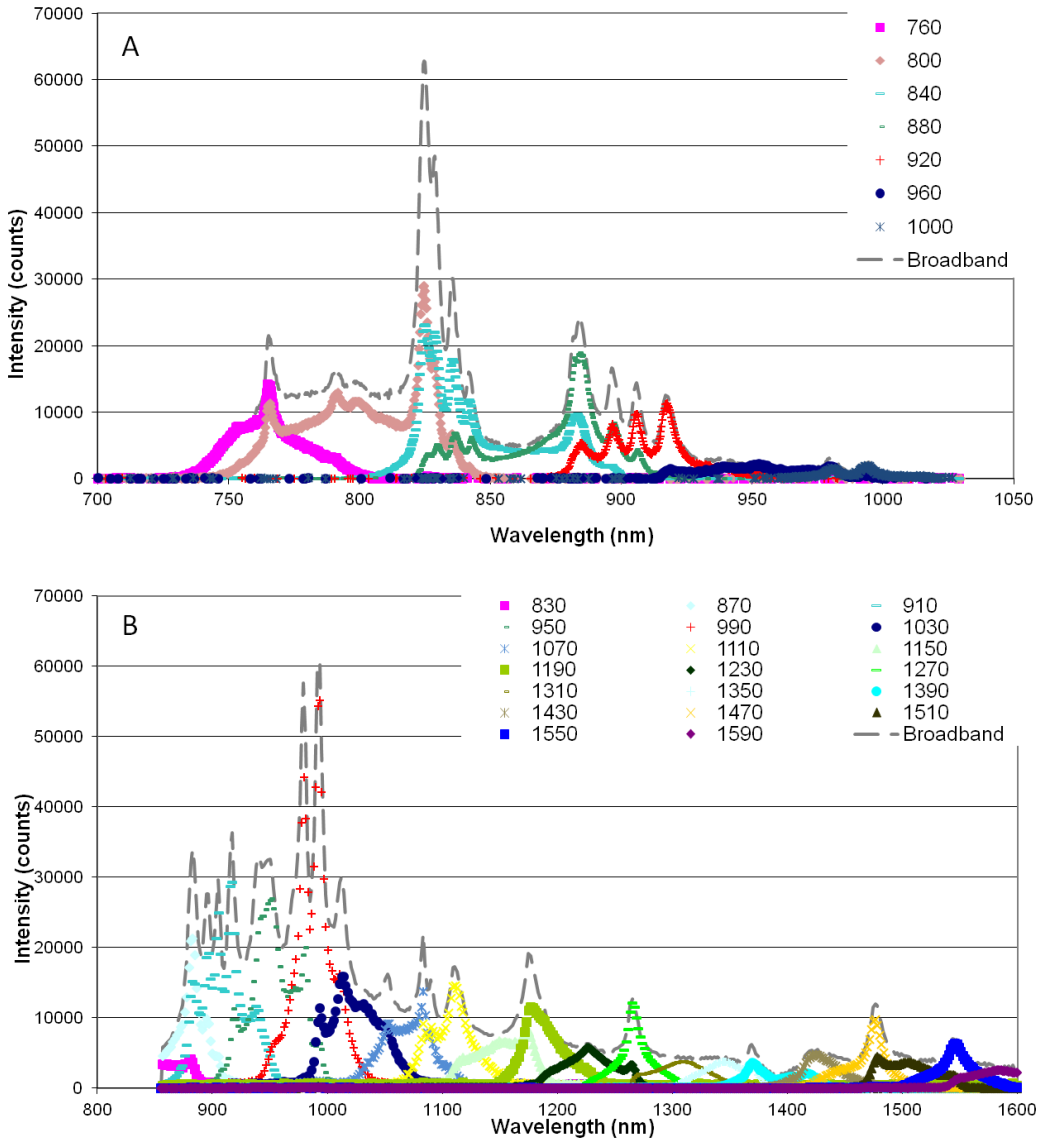

Figure 3.3: Spectral output of the NIR DLP system collected at 10 nm increments using visible and NIR spectrometers and displayed at 40 nm increments. The visible range (700 nm to 1030 nm) spectral profile (A) is collected at 42 ms integration time with a USB2000+ spectrometer (Ocean Optics, Dunedin, FL) while the NIR range (830 nm to 1600 nm) is collected at 400 ms integration time with a NIR512 spectrometer (Ocean Optics). The grey dashed line indicates the broadband spectral profile in each spectral range.

For the purposes of this characterization, the spatial profile of the illumination is excluded, since the spatial portion of the illumination is factored out in every data set through use of the brightfield 99.9% reflectance background data. This background data is taken prior to every data set in order to factor out differences in the field of view dependent on the particulars of the imaging scene, such as distance from target, and to calibrate exposure time and aperture f-stop to ensure saturation does not occur. The primary use of the background data, though, is to calculate absorbance images for every wavelength. Background data is factored out as follows:

$$A_{xy}(\lambda_i) = \log_{10} \frac{R_{xy}(\lambda_i)_{bkg}}{R_{xy}(\lambda_i)_{data}}$$

where $A_{xy}(\lambda_i)$ is the apparent absorbance, $R_{xy}(\lambda_i)_{bkg}$ is the reflectance data from the 99.9% reflectance target, and $R_{xy}(\lambda_i)_{data}$ is the reflectance data of the subject of interest at wavelength λ_i and image coordinates x and y.

3.2.2 Wavelength Tuning Accuracy

From the spectral profiles in Figure 3.3, we can determine the calibration curve for the tuning accuracy of the light source. This is done simply by plotting the expected center wavelength programmed into the illumination software against the actual center wavelength that was detected by the spectrometer for each recorded bandpass. This curve shows the highly linear relationship between the wavelength programmed into the source and the center wavelength determined by the spectrometer. This calibration curve (Figure 3.4) can be used to create more spectrally accurate illumination schemes.

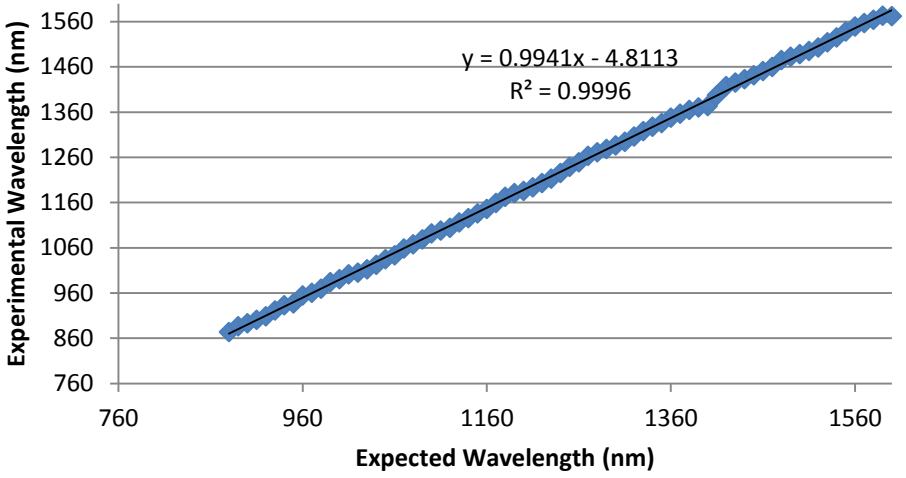

Figure 3.4: Source wavelength calibration curve for 750 µm slit light source tuning.

3.2.3 Bandwidth Characterization

Further information can be derived from the sequential spectral bandpass profile. After normalizing each of the individual bandpasses in Figure 3.3, we can determine an accurate plot of the FWHM bandwidths at each tuned wavelength, as in Figure 3.5. From this measurement of bandwidth by wavelength, we can determine the accuracy of the programmed FWHM bandwidth. The black line represents the manufacturer-specified minimum FWHM at 40 nm.

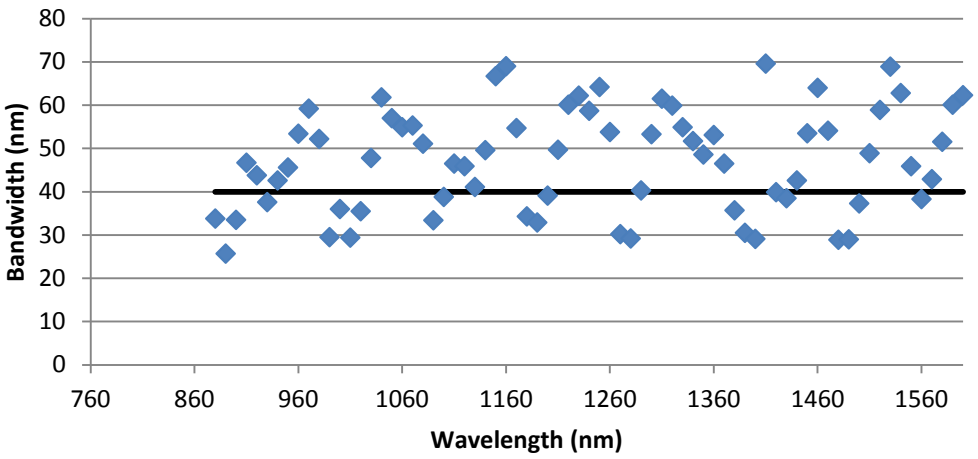

Figure 3.5: FWHM Bandwidth characteristics for NIR DLP system using the 750 µm slit.

The spread of these bandwidths is quite wide, ranging from 25 nm to 70 nm, whereas the manufacturer-stated minimum programmable bandwidth for this slit is 40 nm. The average FWHM recorded is 47.34 nm with a standard deviation of 11.84 nm.

3.2.4 Source Discussion

The spectral profile of the Xe lamp in the NIR range is not as uniform as it is in the visible range.[11, 229] The visible XE lamp profile has a smooth curve to it from 380 nm to 780 nm with a peak at 500 nm. The NIR lamp profile is characterized by numerous spikes, making bandwidth readings for these bandpasses highly non-uniform, which will likely skew reflectance readings with sequential bandpass illumination toward the responses from the intense spikes. This skew is supported by the slight deviation from the linear model in the tuning accuracy curve in Figure 3.4. This is most likely due to the sharp intensity spikes and non-Gaussian behavior of the NIR lamp profile.

The wide spread of FWHM bandwidth is also likely due to the spiky nature of the lamp profile at this range.[229] While some wavelengths have an associated sharp peak in intensity, causing a narrow FWHM bandwidth, others contain two or more sharp peaks at either end of the

bandpass, which increase the FWHM bandwidth. The spread seen here is unlike the visible DLP system, which shows a more tightly controlled bandwidth often below the manufacturer's stated minimum,[5,14,228] allowing for great spectral accuracy. While a smaller bandwidth allows more precise control of the spectral illumination and sharper cutoffs, a larger bandwidth allows more light to reach the subject. With more light, exposure time needed is reduced, thereby increasing the overall speed of data collection, however the bandwidth must still be precisely controlled for spectral accuracy. While smaller slit sizes allow illumination adequate for fast data acquisition for the visible DLP system, the Xe lamp's lower output in the NIR range limit reasonable data acquisition times to use the largest slit size possible. While there appears to be no maximum permissible bandwidth for hyperspectral imaging, spectral accuracy demands the smallest resolution possible. This dubious accuracy issue makes collecting data with the NIR system less advisable than with the visible DLP source, which has more predictable and reliable bandwidth characteristics.

3.3 Detector Characterization

To fully characterize the NIR DLP system, more than just the light source needs to be characterized. The FLIR SC4000 VisGaAs CCD is an Indium Gallium Arsenide detector which collects data in synch with the DLP illumination schemes controlled by a computer system and proprietary software. For the purposes of the FLIR SC4000 characterization, the hyperspectral control GUI is used to collect the image output from the camera, and the NIR DLP light source characterized in the previous section is used for illumination. For this camera, two main characterizations are of interest: the spatial and spectral accuracy of the camera.

3.3.1 Spatial Resolution

To characterize the spatial resolution of the FLIR SC4000 camera, the NIR DLP system illuminated a USAF 1951 quartz resolution target with broadband light spanning the 760 nm to 1600 nm range of the NIR system and images were taken. The images were ratioed against a

background image of a 99.9% reflectance target (Labsphere) taken concurrently with the resolution target data, and an absorbance image was obtained by ratioing the data vs. the background in order to remove any artifacts that may be introduced by the 2-D field of view illumination profile. The absorbance image was then used to determine the spatial resolution of the camera.

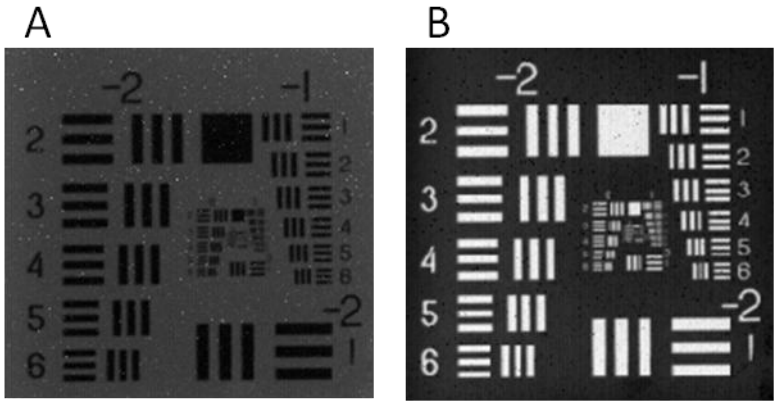

Figure 3.6: Image of USAF 1951 target (A) and absorbance image (B) used to determine spatial resolution of the FLIR SC4000 VisGaAs camera.

The USAF 1951 target (Figure 3.6) consists of a series of equal-length black bars in groups of three arranged in a specific pattern of decreasing size from exterior to interior of the target. By collecting the maximum and minimum intensity of the image pixels in a line across the black bars and the blank (white) space between them, a percent contrast can be calculated.

$$\%\ Contrast = \frac{I_{max} - I_{min}}{I_{max} + I_{min}} * 100$$

where I_{max} and I_{min} are the maximum and minimum pixel values recorded across a set of bars. Different sizes of bars correspond to different levels of resolution. Minimum spatial resolution is defined by previous characterizations of DLP systems as the size of an object identified with at least 20% contrast.[228]

This procedure was performed for two different lenses, a 55 mm focal length Nikon Nikkor lens and a wide angle 18 mm focal length Nikon lens, since both are used frequently with this system, depending on the field of view needed. Figure 3.7 shows a plot of the spatial resolution vs. percent contrast of the camera for both lenses.

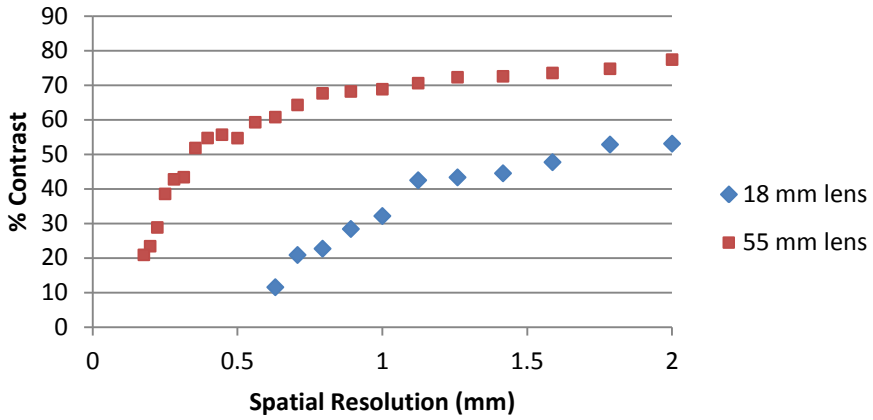

Figure 3.7: FLIR SC4000 spatial resolution characteristics with 55 mm and 18 mm focal length lenses.

For a broadband light percent contrast cutoff of 20% as used in previous works,[2,5,9] the 18 mm lens offers a minimum resolution of 0.70 mm while the 55 mm lens offers a minimum resolution of 0.18 mm. Predictably, for a constant chip size, the 18 mm lens offers less percent contrast at the same resolution versus the 55 mm lens, which is the trade-off for the larger field of view.

3.3.2 Standard Spectral Reference 2065

The NIR512 spectrometer used to collect the illumination data was calibrated using a standard reference material (SRM 2065) characterized by the National Institute of Standards in Technology (NIST). Broadband light from a 250 W QTH source was collected as a brightfield spectrum, and then the reference material was placed in the light path and the reflectance response recorded. SRM has 8 documented peaks. Six are displayed in Table 2 since the extreme peaks, 1

and 8, are beyond the range of the NIR512 spectrometer. Table 2 shows the experimental and published values.

Table 2: NIR Spectrometer Characterization with SRM 2065

Peak locations		5nm spectral resolution			Difference from expected (nm)
Number	Found (nm)	Expected (nm)	Tolerance (nm)	Fit?	
7	976.03	976	0.2	Yes	-0.03
6	1074.6	1075.8	0.9	No	1.2
5	1150.77	1151.3	1	Yes	0.53
4	1221.78	1222.2	0.3	No	0.42
3	1367.3	1366.8	0.5	Yes	-0.5
2	1469.46	1469.1	1.7	Yes	-0.36

The collected transmission spectrum was compared to the published NIST peak values for the material. The spectrometer accuracy was found to be completely on target, with a few exceptions due to the limitation in resolution from only having 512 detector pixels to cover its 700-plus nm range. All of these exceptions were barely outside of the published tolerance, therefore we accept the spectrometer's accuracy.

We used this same SRM 2065 sample to characterize the spectral accuracy of the FLIR SC4000 VisGaAs detector. In order to do this, the FLIR SC4000 camera and the illumination optic were mounted on a tripod as shown in Figure 3.2 approximately 24 inches from the target. A brightfield reflectance, or background, image was taken of a 99.9% reflectance target (Labsphere), then the reference material was placed on top of the reflectance target in the center of the field of view in order to acquire a reflectance spectrum. Data was taken with bandpass increments of 2nm for the entire range of the system as described above, and spectra were ratioed with the background and sampled from the middle of the material to produce an apparent absorbance spectrum.

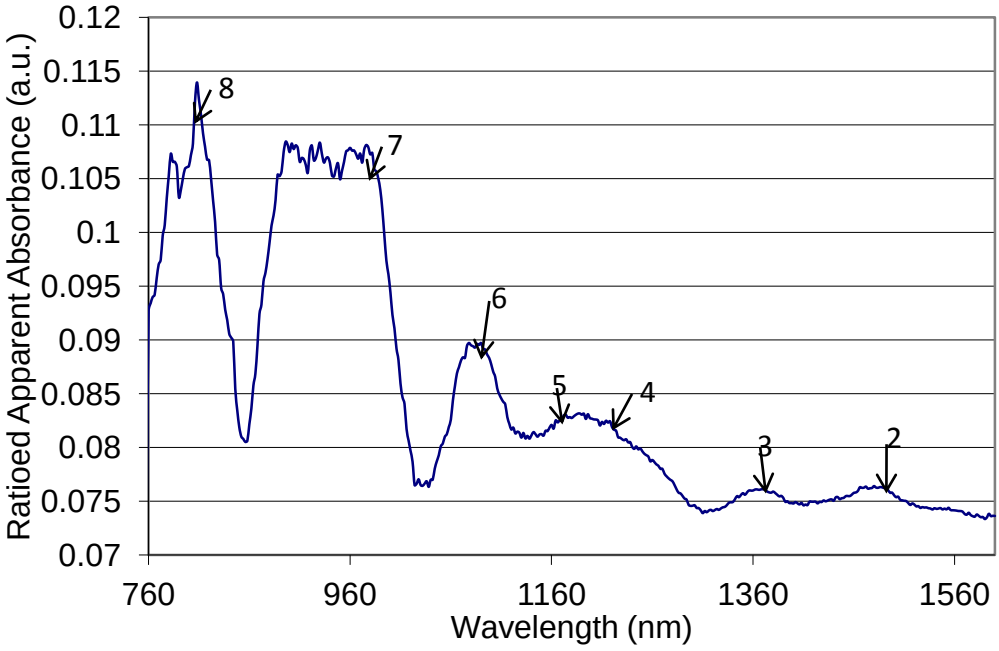

Figure 3.8: Spectral characterization of the FLIR SC4000 camera collected at 2 nm increments using NIST Standard Reference Material (SRM) 2065 absorbance peaks with numbered locations according to SRM 2065 literature.

Table 3: SRM 2065 peak locations as found with FLIR SC4000

Peak Locations		10 nm Spectral Resolution		Difference from expected (nm)	Fit?
Peak #	Peak found (nm)	Wavelength (nm)	Tolerance (nm)		
7	976	976	0.6	0	yes
6	1078	1075.9	2.2	2.1	yes
5	1148	1151.1	3.4	-3.1	yes
4	1222	1222.2	0.9	-0.2	yes
3	1366	1367.1	0.2	-1.1	no
2	1470	1469.2	3.7	0.8	yes

The peaks are mostly within tolerance, with only peak 3 outside of tolerance by 0.9 nm, but as before with the NIR spectrometer, the spectral resolution isn't quite fine enough to detect all peaks within tolerance, since the tolerances aren't quite broad enough to allow for the 2 nm

increment of the illumination scheme. Another interesting feature of this spectrum is the two distinct peaks characterized by NIST at 5 and 4 merge together to form one ostensible peak.

The experimental vs. expected wavelengths at the SRM 2065 peaks for the FLIR SC4000 camera and NIR512 spectrometer are plotted on the same graph for easy comparison in Figure 3.9.

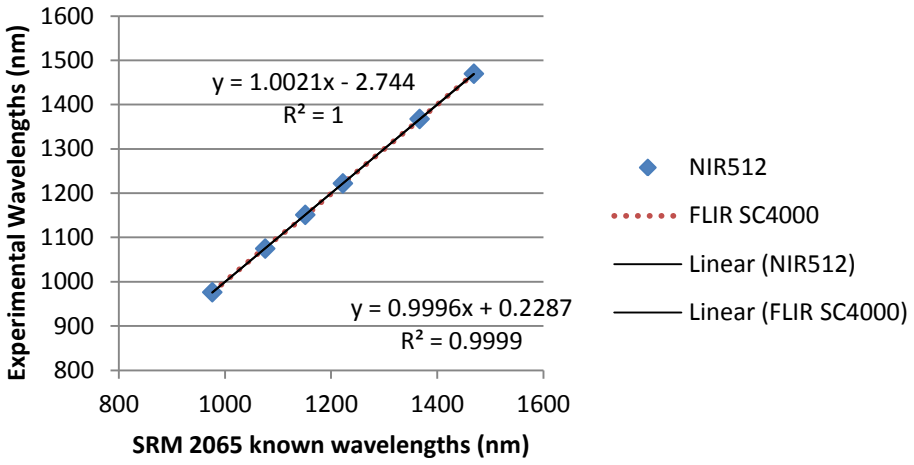

Figure 3.9 FLIR SC4000 VisGaAs NIR calibration curve using SRM 2065 as reference.

Both detectors exhibit linear spectral responses, with R-squared values of 0.9999 or better. The NIR512 spectrometer shows a slight shift from the expected with an intercept value of -2.74 nm while the FLIR SC4000 has an even smaller intercept of 0.23 nm. This indicates that both spectrometer and camera are accurate spectral detectors in the NIR range.

3.4 NIR Laparoscope

In order to extend the clinical utility of the NIR hyperspectral system, laparoscopes were tested for transmittance in the NIR spectral range (755 nm to 1600 nm). Laparoscopes were coupled to a QTH light source with steady output in the NIR range. The light propagated through the laparoscope through the optics to be reflected off a 99.9% reflectance target and then back through the optics for collection by the detector (Ocean Optics NIR512 USB spectrometer). Two laparoscopes were evaluated for this purpose: a 10 mm Karl Storz 0-degree laparoscope routinely

used for visible-range hyperspectral laboratory diagnostics and a 10 mm 0-degree Stryker NIR laparoscope on loan for evaluation purposes. Both Laparoscopes use glass optical elements, but the Stryker NIR laparoscope has an anti-reflection coating on the glass elements which allow for better transmission in the near NIR (wavelengths <950 nm). Transmittance percentages are illustrated in Figure 3.10 below.

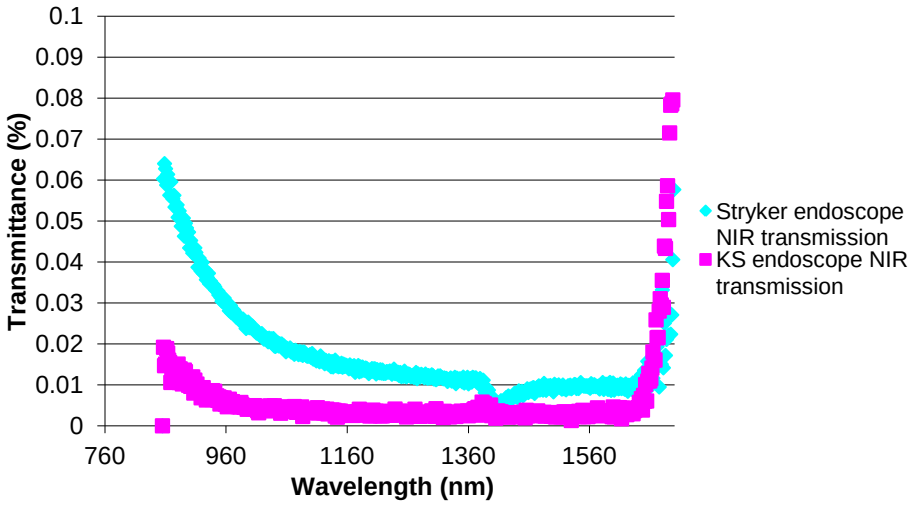

Figure 3.10 Endoscope transmittance for two endoscopes in the NIR range. Brightfield was recorded with a QTH source powered by a current-controlled radiometric power supply.

While the Stryker NIR laparoscope shows a mean increase in transmittance of 73% over the Karl Storz visible laparoscope, that is only an objective difference of a maximum of 0.05% overall transmittance. This is an unacceptable transmittance level for timely data acquisition in the range of 760 nm to 1600 nm. Since the Stryker endoscope is rated for wavelengths closer to the visible range, it seems likely that there is a coating in place on both endoscopes meant to block NIR wavelengths over 800 nm. In order to improve this transmittance, any such coatings would have to be eschewed and optics with a better NIR transmittance than glass would ideally be used, such as quartz. This would require a custom laparoscope to be manufactured, and since this item can't be readily ordered for use by a hospital, it is currently outside the scope of this project.

Chapter 4

Detecting the Common Bile Duct

As stated previously, cholecystectomies are one of the most frequently performed surgeries in America. Most of the complications from cholecystectomies arise due to injury to the CBD rising from a misidentification of anatomy.[2] If an imaging technique can be used to help a surgeon identify specific *in vivo* anatomical features, such as the CBD, the injury rate from this common surgery can be reduced. Once proven for one tissue type, the same method can be applied to many other tissue types, so long as a characteristic spectrum can be found to adequately describe that type across many subjects. This chapter describes the derivation of an average CBD spectrum and the use of several hyperspectral analysis methods to determine the location of the CBD in 13 *in vivo* human subjects.

4.1 Preliminary and Previous Findings

This section summarizes the preliminary studies performed. Included here are *in vivo* human NIR DLP hyperspectral data collection, and visible to NIR LCTF hyperspectral data collection.

4.1.1 Preliminary NIR DLP Data: Under an IRB at UT Southwestern, the FLIR NIR DLP hyperspectral imaging system was taken to St. Paul University Hospital in Dallas, TX to collect hyperspectral reflectance data of the gall bladder and CBD of three human patients during open surgery. It was hypothesized that there would be spectral differences between the tissues in the NIR region of 760 nm to 1600 nm.

Data was collected with a FLIR SC4000 VisGaAs camera on a tripod overlooking the subject in open surgery and illuminated with sequential narrow bandpasses of light from 760 nm to 1600 nm at 5 nm intervals. Each image cube took approximately 20 to 30 seconds to collect. Once filtered and normalized using specialized Matlab scripts, the data appeared to have no appreciable spectral difference between biliary and non-biliary tissue in this wavelength range.

Each data pair of bile duct and surrounding tissue correlate highly to each other, returning correlation coefficients of >0.90 in every case (Figure 4.1).

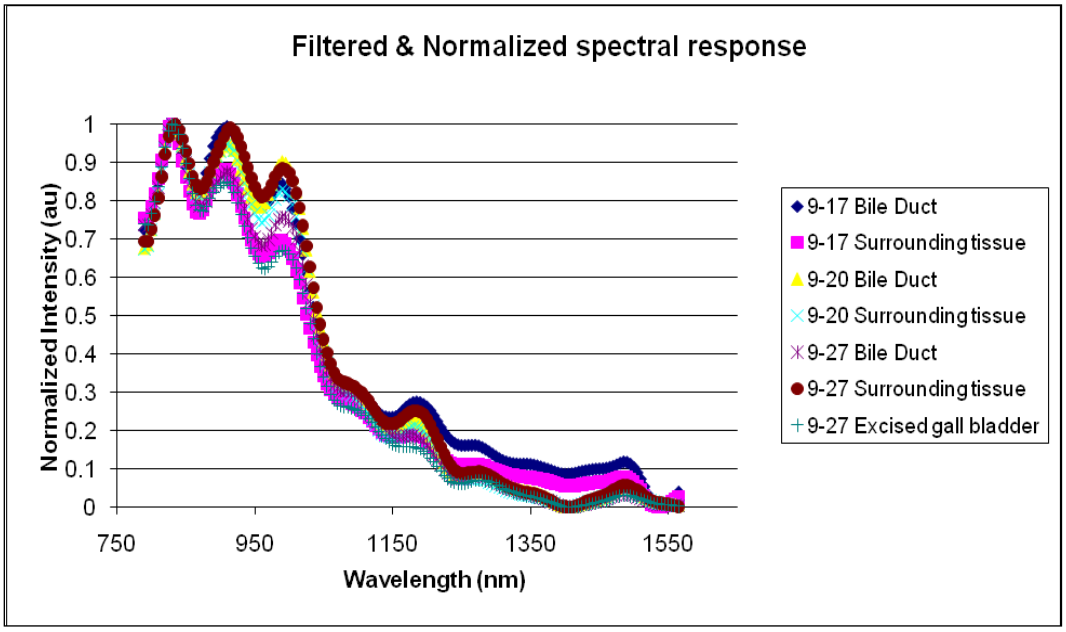

Figure 4.1: Plot of the spectra from three different bile ducts and their surrounding tissues.

Principle components analysis (PCA) images of the hyperspectral data set support this, with only the first in a series of PCA images showing any appreciable variance in the spectra of the field of view for all three data sets, as shown in Figure 4.2. Since the first PCA image in a hyperspectral data set is commonly held to represent the overall brightness (intensity) variance of an image scene,[235] the lack of much distinction in following PCA images indicates that all the spectra in that wavelength range are very alike. The shapes of the collected spectra in this wavelength range correspond understandably to fat,[236] so it is highly likely that the spectrum of fat dominates this imaging region.

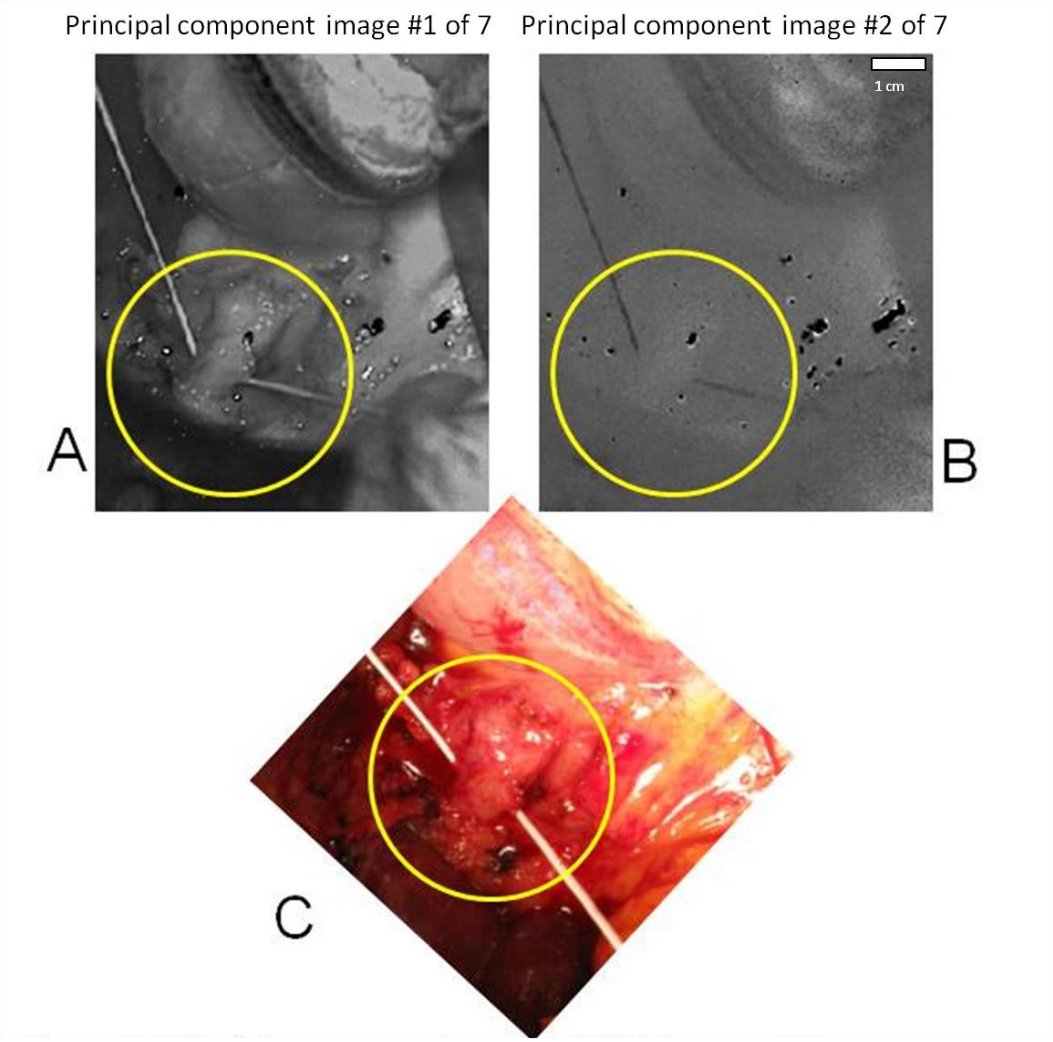

Figure 4.2 Principal component analysis (PCA) images of the common bile duct and surrounding tissues (A and B) and the normal digital photograph (C). The area with the common bile duct raised by string is denoted by the yellow circle.

From this brief foray into the 760 nm to 1600 nm region, it is concluded that there is little to no difference in the spectra of tissues in this wavelength range. There are several approaches in this method which can be modified, such as sectioning the spectral illumination into two separate ranges and adjusting the camera exposure time accordingly to increase the signal acquired in the

wavelengths beyond 1100 nm. Imaging opportunities for open surgery in this area of the body are quite limited, however, and collection with a better-understood wavelength range (380 nm to 780 nm) subsequently proceeded.

4.1.2 LCTF Revisited Data:

Previous studies have shown that spectra taken with the visible DLP system and LCTF systems, characterized in the same way as described in Chapter 3, produce nearly identical data cubes when imaging the same *in vivo* subject.[6] Both these systems acquired data in a sequential bandpass pattern between 520 nm and 645 nm with an increment of 1 nm for a total of 126 bands in the data cube. Both systems also used a CoolSNAP HQ2 visible CCD camera for detection.

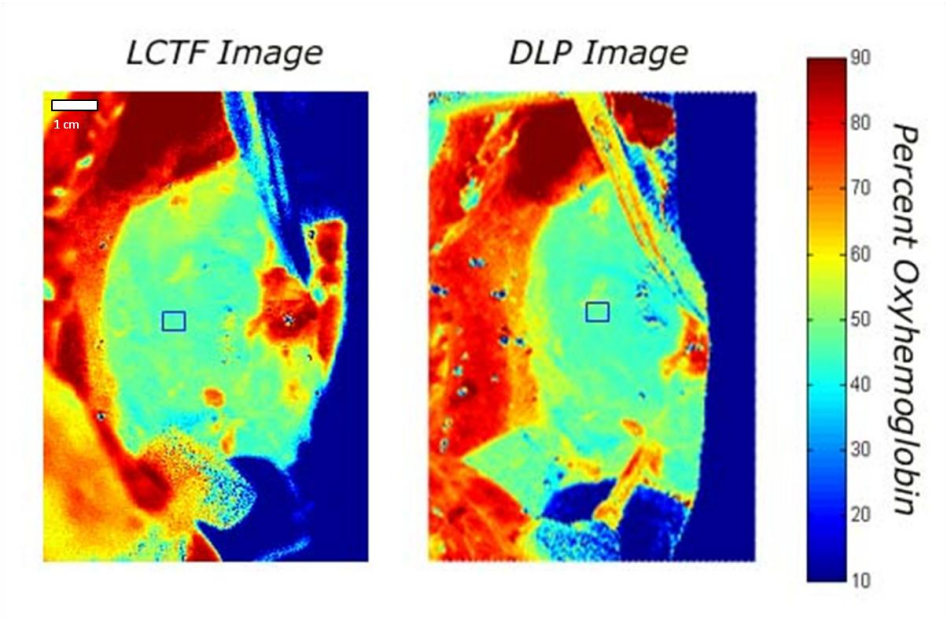

Figure 4.3: LCTF and DLP images of the same subject, a pig kidney under 60 minutes of blood vessel occlusion, encoded for percent oxyhemoglobin concentration in the same range viewed side by side. Red areas indicate a higher concentration of HbO_2 while blue areas indicate higher deoxy-Hb concentration.

Both images in Figure 4.3 are of the same subject, a deoxygenated pig kidney that had been the subject of arterial occlusion for 60 minutes. The normalized average spectra taken from

the boxed areas cover the same 520 nm to 645 nm range and show a RMS difference of only 0.018, as shown in figure 4.4. The spectra recorded are consistent with the reference spectrum of deoxyhemoglobin, which is to be expected for a kidney which has been occluded for 60 minutes.

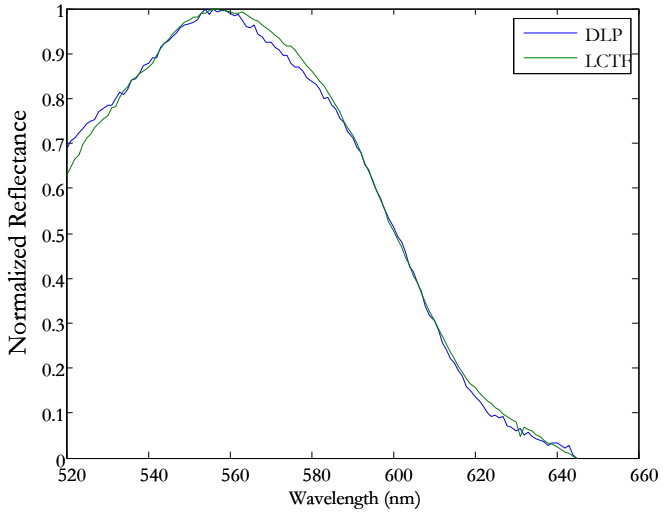

Figure 4.4: Comparison of a DLP system acquired spectrum to one acquired via LCTF. The spectra have an RMS difference of 0.018.[228]

The main apparent difference in the spectrum acquired with the DLP unit vs. the LCTF system seems to be the smoothness of the acquired spectrum, with the LCTF system producing a slightly smother output. This is due to the difference in sources, since the detector ends of the system used the same camera. The LCTF uses a 250 W QTH lamp with a constant current radiometric power supply, which offers a very stable illumination necessary for the LCTF to acquire meaningful data. The DLP source, by contrast, depends on a 500 W Xenon lamp source, which is essentially an arc source with an inherent flicker. The DLP system's more powerful source enables a faster acquisition time, however, cutting the acquisition time of a full 126 band data cube from 35 seconds to approximately 25 seconds. Considering the very small difference in output spectra, data acquired with the LCTF system and the DLP system are therefore arguably

identical, and data acquired with an LCTF system could be used as a reasonable expectation of a DLP system that collects in the same range.

In previous years, LCTF hyperspectral reflectance data was taken of the gall bladder and common bile duct of several subjects *in situ*.[3,4] This data was taken in the range of 650 nm to 1050 nm using a NIR liquid crystal tunable filter attached to a PIXIS 1024BR CCD camera and a QTH broadband light source.[237]

The spectrum for pure bile in the 650 nm to 1050 nm range is distinctive, exhibiting the characteristic water peak around 970 nm and a gentle slope from less than 700 nm to a nadir around 900 nm unlike other common biological signals in the area such as oxy- or deoxyhemoglobin shown in Figure 4.5.

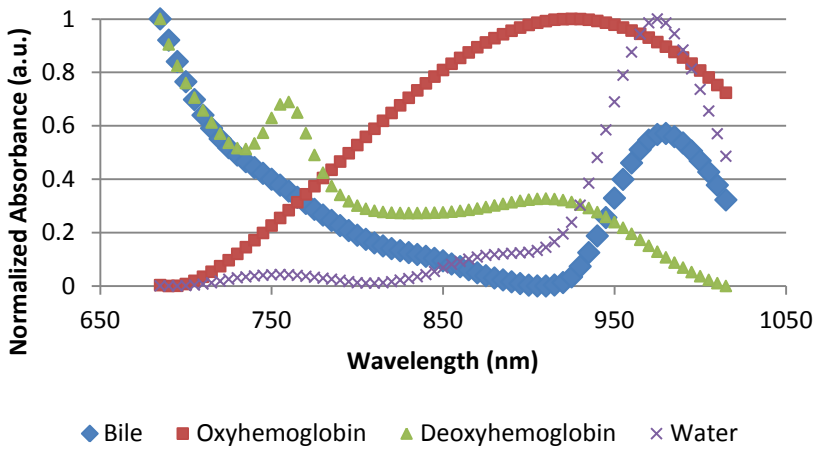

Figure 4.5 Filtered and normalized in vitro bile, oxyhemoglobin, deoxyhemoglobin, and water absorbance spectra in the 650 nm to 1050 nm wavelength range. Spectra are filtered and windowed by 7 data points with a Savitsky-Golay filter.

The longer-wavelength NIR DLP system completely misses the distinctive slope prior to the 760 nm start of its own range, and this could be a reason that the spectra of the bile duct and surrounding tissue in that range showed no distinction between each other. The peak at approximately 980 nm is shared with water, and since most biological tissues (including bile) have

high contributions of water, this peak does not help make bile distinctive in this range. Additionally, PCA images of the 650 nm to 1050 nm LCTF data show much more variance in their detail than the DLP images of the 760 nm to 1600 nm range, as in Figure 4.6.

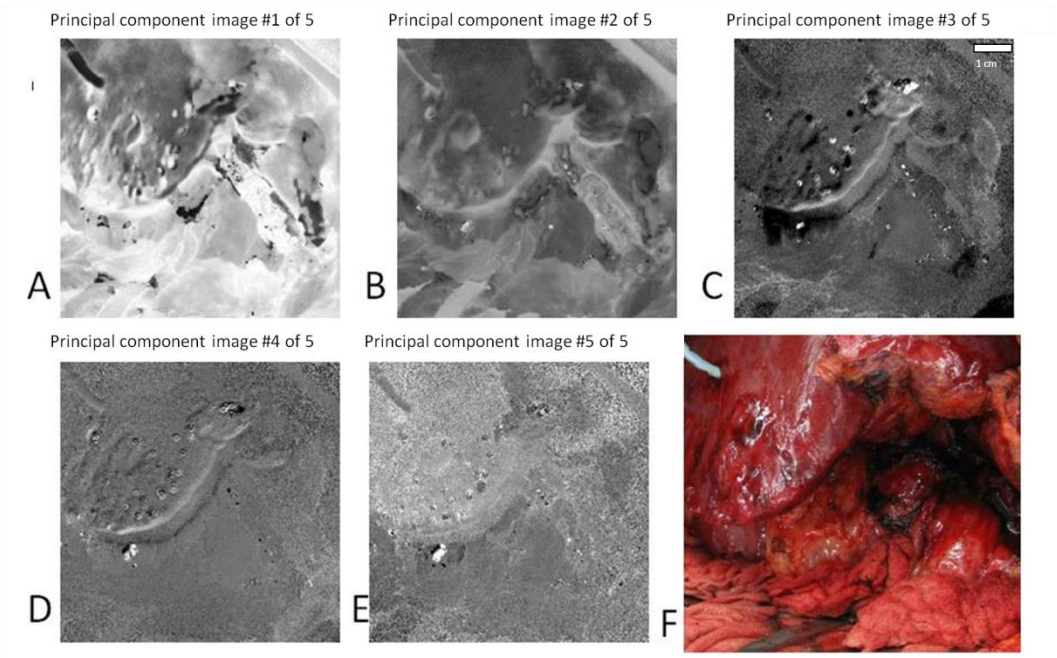

Figure 4.6: Principal component images of the pig biliary tract and surrounding tissue with fat and connective tissue excised. A through E represent PCA images 1-5, and F is the corresponding digital photograph from approximately the same angle.

The fact that the PCA images show variance beyond the first image indicates that there are several varied spectra in the scene. Upon sampling data in different areas of the field of view, this is shown to be accurate, and the spectra correspond to the known tissue types. For example, data from the liver shows a combination of deoxyhemoglobin and bile spectra whereas data from the hepatic artery shows a strong oxyhemoglobin spectrum. We can conclude from the evident spectral differences that taking hyperspectral data in the 650 nm to 1050 nm wavelength range may provide the differences needed and imaging with the 525 nm to 1050 nm or 380 nm to 780 nm DLP hyperspectral imaging system should be explored.

4.2 Bile Transmission Experiments

In order to better spectrally understand the common bile duct, bile was extracted from patients undergoing cholecystectomies and measured over a range of 350 nm to 1700 nm using two spectrometers (Ocean Optics USB2000+ at 40 ms integration time and NIR512 at 300 ms integration time) for different concentrations of bile. As samples were sparse and objective characteristics of the samples ranged from green-tinted apple juice to used motor oil with large solid particulates, the clearest example with least particulates is shown in figure 4.5.

Bile samples were placed in a 10 mm by 10 mm clear quartz cuvette in 800 μL increments with an Eppendorf Repeater Plus pipette. A neutral density (ND) filter of 3.0 optical density was put in the light path to avoid brightfield saturation in the spectrometers. Both the cuvette and ND filter were placed in an Avantes cuvette holder which was attached by wavelength range-appropriate Avantes fiber optic light guides to an Avantes fiber optic output light source and the spectrometers. Bile transmission characteristics were recorded for four concentrations: undiluted, two parts bile to three parts water, two parts bile to four parts water, and one part bile to three parts water, where each part is 800 μL.

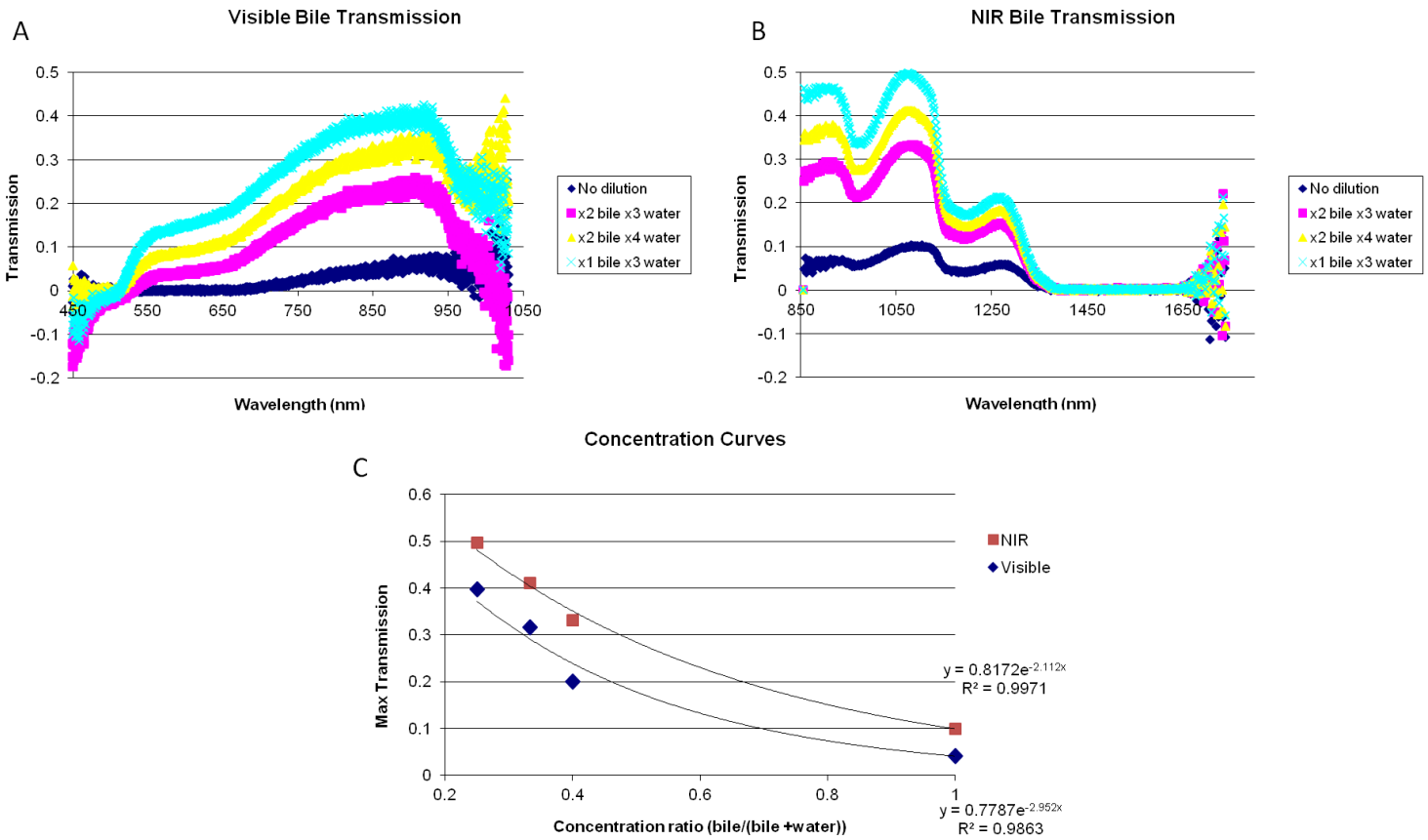

Figure 4.7: Bile transmission spectra using visible (USB2000+, 340 nm to 1030 nm) and NIR (NIR512, 855 nm to 1735 nm) Ocean Optics spectrometers at different concentrations of bile to water. (A) shows the visible range, (B) shows the NIR range, and (C) shows the concentration curves for both ranges.

Spectral attenuation near the edges of the spectrometer detection ranges make the transmission spectra appear slightly unstable, but this is merely an artifact of noise collected at those small numbers at the extreme ends of the range where the signal-to-noise ratio is relatively poor. The reflectance spectra of the CBD in the NIR range are similar to the transmittance spectrum in the figure above, except for the fact that there are three peaks between 760 nm and 1100 nm in the reflectance spectrum and only two local valleys in that range for the transmission spectrum.

Dilution with water seems to change the shape of the bile transmission spectrum slightly, shifting the peak near 1100 nm closer to 1050 nm with further dilution. This makes sense, since water has strong absorption near 1000 nm. Other peaks don't seem to be much affected by the addition of water other than increasing the amplitude of transmission. The local minimum around 1000 nm at all concentrations also makes sense, considering water comprises about 85% of bile.

From this transmittance data, it should be simple to calculate an absorbance spectrum based on Beer's Law. With this, the contribution of bile in the CBD spectrum can be calculated.

4.3 Average *In Vivo* Bile Duct Spectrum

Just as no person is exactly the same, there is variance in biological spectra from person to person, especially if those people suffer from different diseases. There are many different diseases in different interior organs that can affect bile or irritate the CBD. In order to make a bile duct algorithm practical so that it may detect the CBD across many individual biologies and disease states, an average spectrum must be found.

4.3.1 Human Data Collection

In order to produce an average CBD spectrum, data was taken of open surgeries which exposed the common bile duct. Surgeries took place at UT Southwestern Medical Center under the supervision of Drs John Mansour and Roderich Schwarz in accordance with IRB study STU 082010-299. 13 human subjects were imaged with the visible DLP hyperspectral imaging system

in the range of 380 nm to 780 nm at 4 nm intervals over the course of 12 months. The three preliminary cases collected with the 760 nm to 1600 nm NIR system in order to determine its viability for this project are not included in the calculation of an average visible spectrum.

Procedure: Human subjects were first identified for data collection by the supervising surgeon. Suitable subjects were open surgeries during which the common bile duct area would be exposed during the course of the surgery, such as pancreaticoduodenectomies, pancreatectomies, duodenectomies, and other surgical oncology procedures in the area which would necessitate the anatomy surrounding the CBD to become exposed. Of particular interest were Whipple procedures, where several organs may be cut and sutured (http://www.surgery.usc.edu/divisions/tumor/pancreasdiseases/web pages/pancreas resection/whipple operation.html) and therefore make laparoscopic procedures inadvisable. Three open procedures were recorded with the NIR HSI system, and 13 with the visible system. The 13 visible data sets are used for subsequent analysis.

Before the patient enters the room, the OR is darkened as much as possible and a background reflectance image is taken with a 99% reflectance target (Spectralon) at the same approximate distance that the subject is predicted to be from the camera (approximately 22 inches) in order to determine an accurate lamp and ambient light profile. The lamp is allowed to warm up for 15 minute to 20 minutes prior to taking a background to allow it to reach steady-state illumination. During this time, the camera is also focused and the aperture adjusted, and those values recorded.

After the patient enters the OR and the surgeon has exposed the target anatomy, the tripod is wheeled to the patient so that the camera overlooks the field of view. Since the surgeon does not always need to uncover the CBD from its surrounding tissues, the target anatomy is not always apparent to the untrained eye. The supervising surgeon or an assistant indicates the location of the CBD and takes color digital photographs. The OR lights are turned off and

ambient sources blocked as well as they were for the background. Three to four data cubes of 104 frames each (380 nm to 780 nm at 4 nm intervals) are collected over the course of two minutes for later analysis.

Reflectance data is sampled from the CBD areas indicated by the surgeon to produce an average CBD spectrum for each case. These case-by-case averages are normalized from 0 to 1 according to unity-based normalization and shown in Figure 4.8. An overall average of these normalized spectra is also displayed. Unity-based normalization is used in this study for consistency with other spectra, such as oxy- and deoxyhemoglobin collected and analyzed previously by this lab,[3-14, 232-234] for the eventuality of inter-tissue spectral comparisons. Other normalization methods, such as the total area under the curve calculation of Total Ion Current (TIC) or median area-based methods may produce spectra of greater similarity,[238] but are currently outside the scope of this study.

The average CBD spectrum shows a strong qualitative similarity to the known spectrum for oxygenated hemoglobin. This observation prompts the question of how much of the CBD spectrum is comprised of the spectrum for oxyhemoglobin. An application of the linear mixing model (LMM) can provide an answer to this question. As stated in Chapter 2, the LMM equation is as follows:

$$r_i = \mathrm{M}\alpha_i + n_i$$

where r_i is the mixed spectrum, M is the matrix which contains the absorbance spectra of the components (i.e. endmember spectra), α_i is the vector of the abundance fractions of each component, and n_i is the residual. In this case, the abundance fractions are the unknowns, and the number of them to solve for depends on the number of components assumed. Least Squares unmixing is one of the simplest methods to solve this problem. Since materials cannot realistically have negative abundance fractions, LS with the non-negativity abundance constraint forces the abundance matrix to make physical sense.

For this case, I assume the presence of three spectra: oxyhemoglobin, deoxyhemoglobin, and bile. The absorbance of bile is derived from the transmission spectra collected, while oxy- and deoxyhemoglobin are modified from known references to conform to the spectral intervals of the CBD data. Unmixing the average CBD spectrum in Matlab with these three endmembers over a spectral range of 528 nm to 600 nm returns abundance fractions of 0.59 for oxyhemoglobin, 0.07 for deoxyhemoglobin, and 0.20 for bile with a mean square error of 0.02. This indicates that oxygenated blood comprises about 59% of the CBD spectrum while bile only contributes about 20%. This makes logical sense, since the CBD tissue is fed by oxygenated blood, and whatever bile could be visible to the HSI system would be inside the CBD and therefore obscured by the oxygenated tissue.

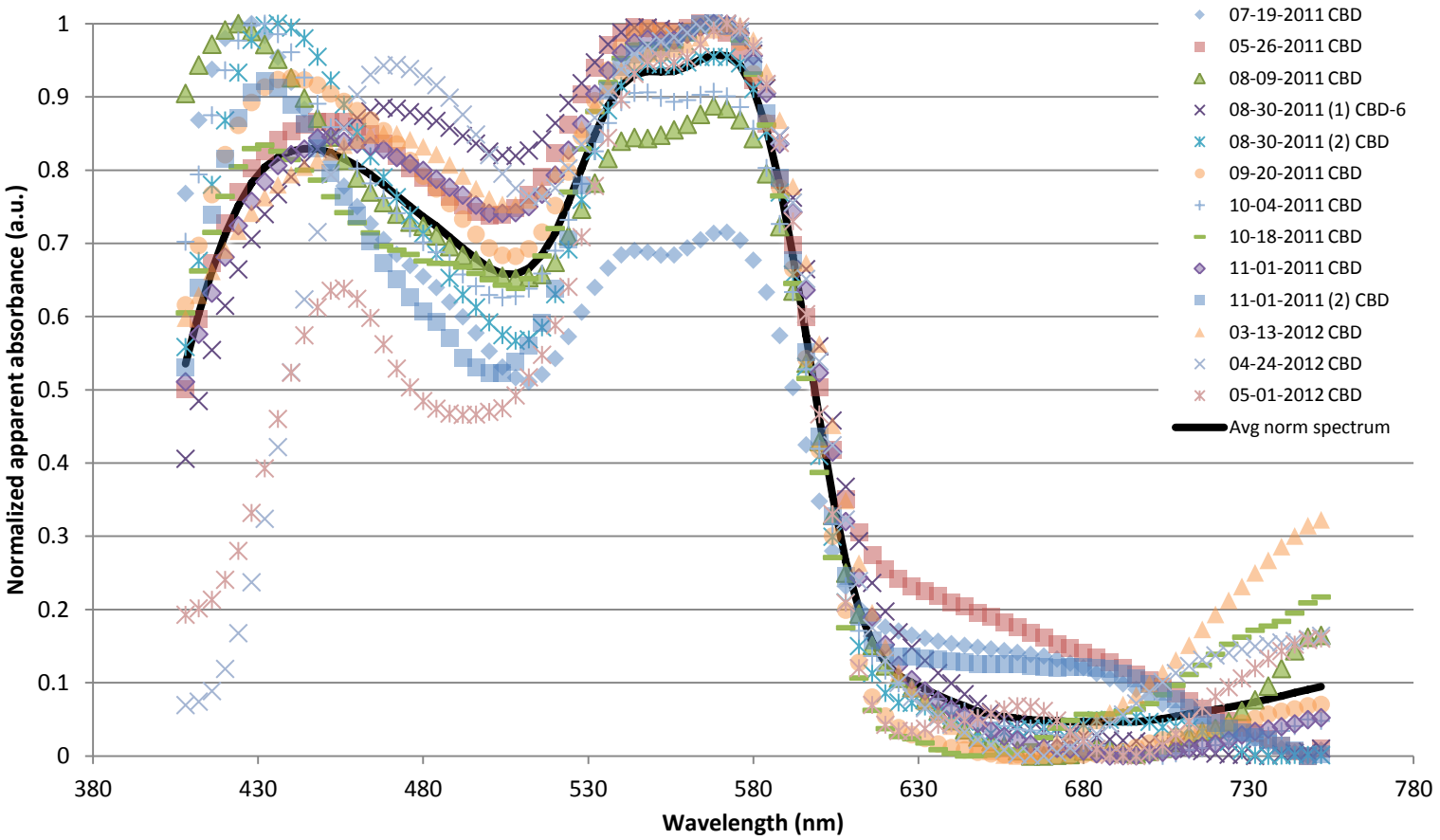

Figure 4.8 All 13 collected CBD filtered and normalized spectra with the average CBD spectrum over the visible range. The data is cropped as part of the Savitsky-Golay filtering process to help eliminate attenuation errors.

4.4 Bile Duct Analysis

Spectral analysis of CBD data was performed with a combination of MatLab and ENVI software. MatLab is strong for matrix manipulation and also aids in the recording of the data, so it is easiest to continue using it for certain algorithms, such as PCA and two-component deconvolution.[5,6,13,14] ENVI specializes in analysis of whole images, with many hyperspectral analysis algorithms coming standard in the software package, from benchmarks such as N-FINDR and PPI to SVMs and kernels.

4.4.1 Band Subtraction

CBD spectra from cases 1 through 7 and arterial spectra from three cases where arterial vessels were obvious were collected from the images and averaged to determine 1) where the differences in average spectra are most pronounced and 2) where they are most the same.[11] Figure 4.9 displays these two spectra.

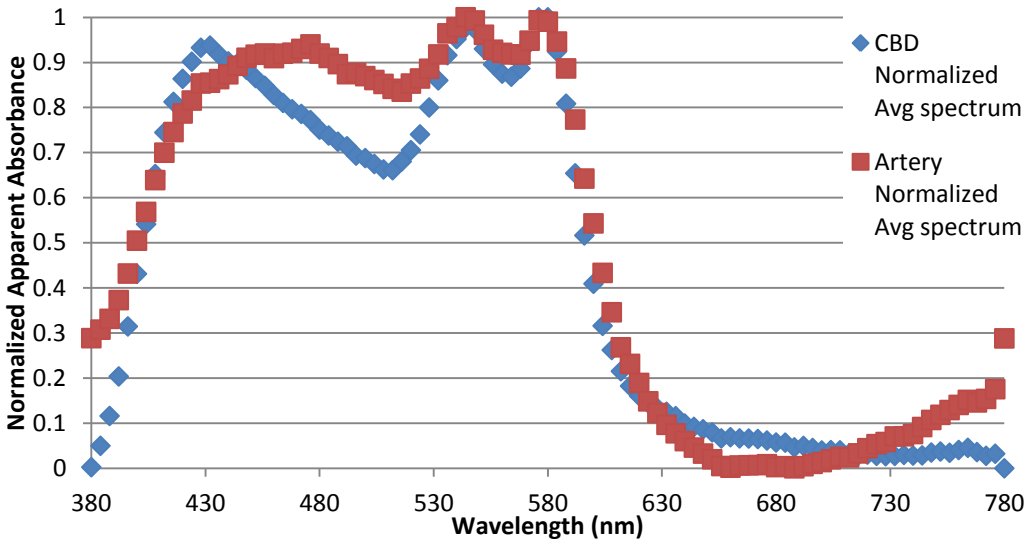

Figure 4.9 Normalized average common bile duct and arterial spectra from CBD cases 1 through 7 for the full range of data collection.

From this information, an algorithm to subtract one hyperspectral image bandwidth from another can be used to highlight areas of high CBD spectral presence. Finding the best bands to subtract can eventually lead to the creation of a simplified system that only illuminates for the needed bands, thereby increasing acquisition speed.

Through empirical experimentation, it was determined that adding four peak bands of difference (580 nm, 576 nm, 573 nm, and 548 nm) and subtracting four bands of nadir difference (500 nm, 504 nm, 508 nm, and 512 nm) produced the clearest images that highlighted the area of the common bile duct. This method only requires 8 bands for illumination, much less than the total 101 bands collected. This method was then applied to all 13 cases with some success.

Adding the bandwidths corresponding with the most spectral difference and subtracting the ones with the least spectral difference produces contrasting image as those seen in Figure 4.10. This technique succeeded in highlighting the common bile duct area in approximately 9 out of a total of 13 cases. Analysis with other, more conventional techniques, such as Spectral Angle Mapper (SAM) and Spectral Information Divergence (SID) (discussed later) also identify the common bile duct when given the average CBD spectrum to search for.

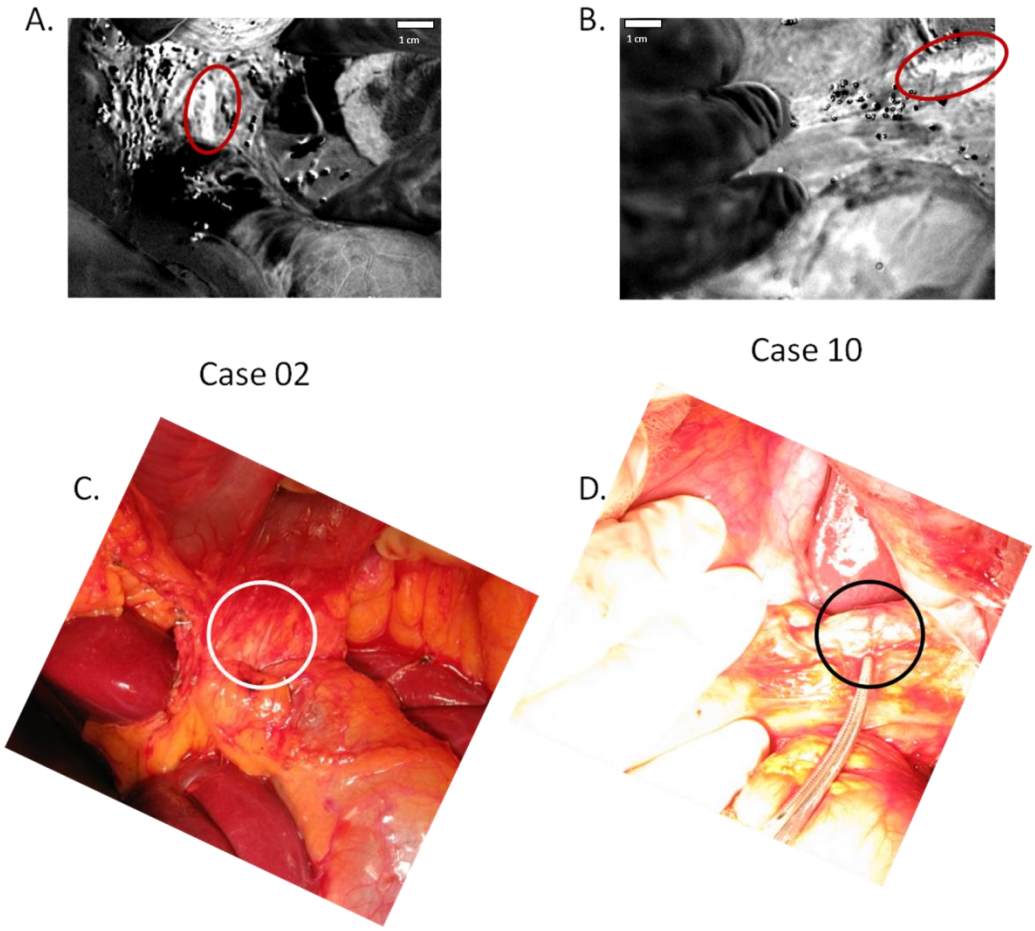

Figure 4.10 Example images and digital comparisons for 8 band subtraction. Brighter areas in (A) and (B) indicate areas which are more likely to be CBD than artery based on spectral bands of high difference vs. spectral bands of low difference. (C) and (D) show the equivalent scenes as photographed with a color digital camera. CBDs are circled.

4.4.2 Algorithms Attempted

The comprehensive review presented in Chapter 2 was performed with the intent of learning what hyperspectral analysis algorithms existed and which would likely be most effective

for an *in vivo* surgical imaging application. The following table summarizes the algorithms attempted for the purposes of differentiating the CBD from its surrounding tissues.

Table 4: Summary of Attempted Algorithms, Failure, and Success. Successful algorithms are highlighted in yellow. Pink names indicate data transform methods. Blue names indicate classification algorithms.

Algorithm	Inadequate for Mixed Spectrum Target	Requires Training Data	Inconsistent	Success Rate	Important References
LS				10/13	19, 27, 51
PPI	X				19, 108
SMACC	X		X		130, 131
SVMs		X			31, 150
NN		X			153, 158
ICA			X		161, 168
EM/ML		X			222, 226
MF/MTMF				5/9	203, 137
SAM				12/13	43, 58, 130
SID				12/13	43, 58
Mahalanobis Dist		X			239
Minimum Dist		X			79
Parallelepiped Dist		X			240
K-Means	X				22, 106
IsoData	X				105
PCA			X		18, 120
MNF			X		18

Most of the algorithms tried failed to adequately differentiate the CBD from its surrounding tissues. PPI, when used for unmixing data, looks for "pure" spectra, which it sets as endmembers, and outputs classification maps for each "pure" endmember it finds. PPI has been used to good effect on geologic data sets such as the AVIRIS data of the Cuprite mining area[75,83,107] where the endmember spectra are highly distinct. It is also used as a standard to measure the effectiveness of other endmember extraction algorithms with simulated data[75,83]

where pixel purity can be controlled. Since the CBD is a highly mixed spectrum, PPI fails to distinguish the CBD area. SMACC sees a similar problem, since it also works on the "pure" pixel assumption and has shown to work effectively with geologic data.[129] It seeks endmembers and then outputs abundance maps denoting the locations and abundances of each endmember. When the number of endmembers to seek is specified in the SMACC algorithm, even a number of endmembers as low as 4 does not produce an image which distinguishes the CBD on its own. Likewise, none of the endmembers identified resemble the CBD spectrum. Instead, a combination of abundance maps with red-green-blue overlay must be used to distinguish the CBD fully. Since SMACC derives its EMs from each data cube individually, the number of endmembers and their spectra differ from case-to-case, with the number of endmembers which show any part of the CBD remaining inconsistent.

SVMs and NNs are decision-tree algorithms that have been used successfully to unmix real geological[56,86] and simulated[73,158] mixtures where all the statistics are well understood. They are unable to seek a spectrum when they know only the average reference target spectrum and not further statistics attached to a specific data set. In other words, they need a region of interest (RoI) from the data set in order to find the target features. This is akin to asking how to spell a word when you already see it in text before you. It defeats the purpose of identifying the CBD location without knowing anything prior about the specific case anatomy. These algorithms will only work in this application when the CBD has already been located in the image, and would only be of use if there was more than one CBD of interest in one data set.

EM/ML, Mahalanobis distance, Minimum distance, and Parallelepiped distance are all classification algorithms readily available in ENVI which require RoI data from the hyperspectral data cube to be analyzed in order to calculate higher-order statistics on the target spectra. EM/ML has seen success with simulated[182] and real geological[183] and urban[227] data. Minimum distance as a spectral measurement has been used on simulated data[79] and real data.[240] Mahalanobis distance

in hyperspectral imaging has been robustly explored with simulations and aerial data.[239] Parallelepiped distance and other classification algorithms have been used in determining contamination in food products.[240] Since these algorithms require higher-order statistics, as with SVMs and NN, if the position of the CBD is already known well enough to attain a RoI for these algorithms, they are of little use. That said, when they are given the RoIs from a data set, they do identify the CBD in that data set with very few false positives. They are unable to use the average CBD spectrum data derived earlier to find the CBD in each individual hyperspectral image cube.

K-Means and IsoData are two unsupervised classification methods. The user inputs the number of endmembers to search for or lets the algorithm attempt to calculate them on their own, and the algorithm returns a classification map. While they work well on geological[106] and simulated data,[105] unfortunately as with PPI and SMACC, these two algorithms search for the most spectrally independent, "pure" pixel endmembers. With the CBD being a demonstrably mixed spectrum, these two classification methods cannot distinguish the CBD from its surroundings in any of the collected data sets.

ICA, PCA, and MNF are all data transform methods, described in Chapter 2. They take the data and transform it to create unique grayscale output images ordered in terms of spatial coherence. The noise-whitening effect of MNF is essential for the use of some other algorithms, such as MF and MTMF (discussed later). These transforms are often used to reduce the dimensionality of the data and thus reduce the complexity of the algorithms which follow and not usually as spectrum-seeking or anomaly detection algorithms by themselves. In the case of searching for the CBD without knowing much prior information about it, the transformed images often highlight areas of interest, such as ones which exhibit strong spectral similarity. It is in these images that interesting areas often show themselves, such as the area of the CBD. When these transform images do show the CBD, it is often not just in one image. These images can be

overlaid upon each other and tinted in red/green/blue (RGB) fashion so that the areas that show brightly in each of the grayscale transform images show whiter in the full overlay.

Without further analysis, the data transform images can display the CBD with good definition, especially if several bands are overlaid in a RGB display. Figure 4.11 shows the MNF outputs of the 3rd, 4th, and 5th MNF images from three different cases in which the CBD appeared in some or all of those images. Of the 9 cases which did not produce singularities in any part of the data, the CBD appeared the most in the 3rd MNF image with 5 times, and second most often in the 4th MNF image with 4 times. In only one of these data sets did both the 3rd and 4th MNF output image both show the CBD clearly.

Another failing of the data transforms are that they do not remain stable when attempting to process data which contains singularities. These singularities arise when pixels in the collected data are more intense than the corresponding background data collected on a 99.9% reflective target. This is always a possibility in biological data collected with the current DLP HSI systems due to backscatter effects from the moist scene. It is possible to circumvent this problem by using a spatial subset of the data, but in order for that to be a viable option and still give data on the CBD, prior information must be known about the arrangement of the field of view, particularly the location of the CBD. Additional preprocessing may also be possible to exclude or replace problematic bands or pixels.

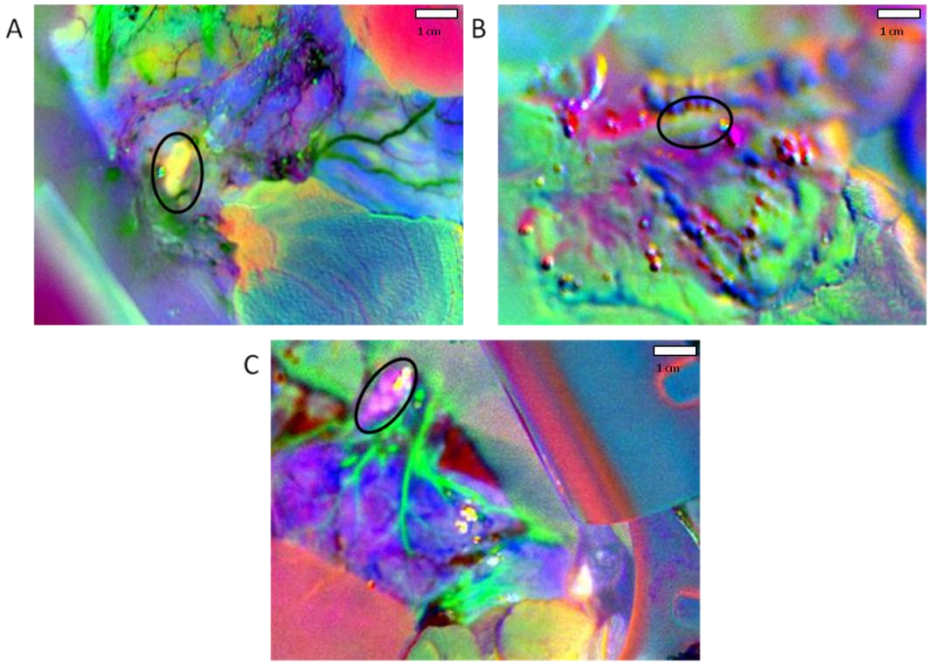

Figure 4.11 MNF RGB overlay images from (A) case 07, (B) case 11, and (C) case 13 using MNF bands 3, 4, and 5.

Since specific chemistry between people and the precise anatomical area recorded vary slightly from subject to subject, especially with disease states, the bands at which the CBD is highlighted with MNF does not always remain consistent between cases, so using this method to detect the CBD is not advised. Using MNF and counting the number of meaningful bands produced from this data transformation is one way to estimate the number of endmembers in a data set (See Appendix A).

The reason that the transform methods fail in the purpose of finding the CBD is due to the inconsistency of which output images show the CBD, and how many of them do for each data cube. For the purpose of reliably discerning the CBD from its surroundings, it would be best to find it consistently in the same transform image across data sets, otherwise a CBD could be misconstrued as an artery or vein, or vice versa. It is also quite difficult to quantify these images, as the images which show the CBD change between data sets.

The successful algorithms were able to detect the CBD through the use of average reference spectra determined across all cases, rather than spectra derived on a case-by-case basis, such as with unsupervised classification. They also output reliable, consistent abundance images or classification maps. SAM, SID, MF, and LS using two reference spectra were considered successful based on these criteria.

4.4.3 SAM and SID

Spectral Angle Mapper (SAM) and Spectral Information Divergence (SID) are two methods used to measure the similarity between spectra. They can both be expanded into classification methods which produce maps of an image scene that indicate pixels with the closest similarity to input reference spectra, i.e. supervised classification. SAM and SID are simple and similar in design, comparing each pixel spectrum in a hyperspectral image to target spectra using different metrics. SAM uses a maximum spectral angle threshold, while SID uses a maximum divergence threshold. This makes SAM a deterministic measure, while SID is a statistical measure.[58]

SAM determines spectral similarity by taking the inverse cosine of the angle between two spectra

$$SAM(s_i, s_j) = \cos^{-1}\left(\frac{\langle s_i, s_j \rangle}{\|s_i\|\|s_j\|}\right)$$

$$\|s_i\| = \left(\sum_{l=1}^{L} {s_{il}}^2\right)^{1/2}, \|s_j\| = \left(\sum_{l=1}^{L} {s_{jl}}^2\right)^{1/2}$$

where s_i and s_j represent the spectra being compared, and $\langle s_i, s_j \rangle$ is the dot product of the two spectra.

SID is slightly more complicated than SAM, measuring the discrepancy between two spectra based on their probability mass functions.[43,58,240] This is ultimately the sum of the average

relative entropy (also called cross entropy, Kullback-Leibler information measure, or directed divergence) of s_i with respect to s_j and s_j with respect to s_i, respectively.

$$p_l = \frac{s_{il}}{\sum_{l=1}^{L} s_{il}}$$

$$q_l = \frac{s_{jl}}{\sum_{l=1}^{L} s_{jl}}$$

where $p = (p_1, p_2, \dots, p_L)^T$ and $q = (q_1, q, \dots, q_L)^T$ are the probability mass functions generated by s_i and s_j respectively. The self-information of s_i and s_j for band l is defined by

$$I_l(s_i) = -\log(p_l)$$

$$I_l(s_j) = -\log(q_l)$$

The discrepancy of the self-information of s_i with respect to s_j is

$$D_l(s_i \| s_j) = I_l(s_j) - I_l(s_i) = \log\left(\frac{p_l}{q_l}\right)$$

which leads to the average discrepancy of s_i with respect to s_j over all bands

$$D(s_i \| s_j) = \sum_{l=1}^{L} D_l(s_i \| s_j) p_l = \sum_{l=1}^{L} p_l \log\left(\frac{p_l}{q_l}\right)$$

$$D(s_j \| s_i) = \sum_{l=1}^{L} D_l(s_j \| s_i) q_l = \sum_{l=1}^{L} q_l \log\left(\frac{q_l}{p_l}\right)$$

SID is thus the sum of these average discrepancies or relative entropies.

$$SID(s_i, s_j) = D(s_i \| s_j) + D(s_j \| s_i)$$

Both of these classification methods have been used to measure similarity in biological,[58] food contamination,[240] simulated mixture, and geological[43] data with good success.

For target spectra, the average spectra from cases 1 through 7 are used on all 13 cases to classify the image. It is hypothesized that unity-based normalized average spectra may give better classification results than a non-normalized reference spectrum, so both are tested. Additionally,

preliminary tests demonstrate better spectrum sensitivity if a spectral subset of the data is used due to large variability beyond 600 nm. The following figure shows the two reference spectra used.

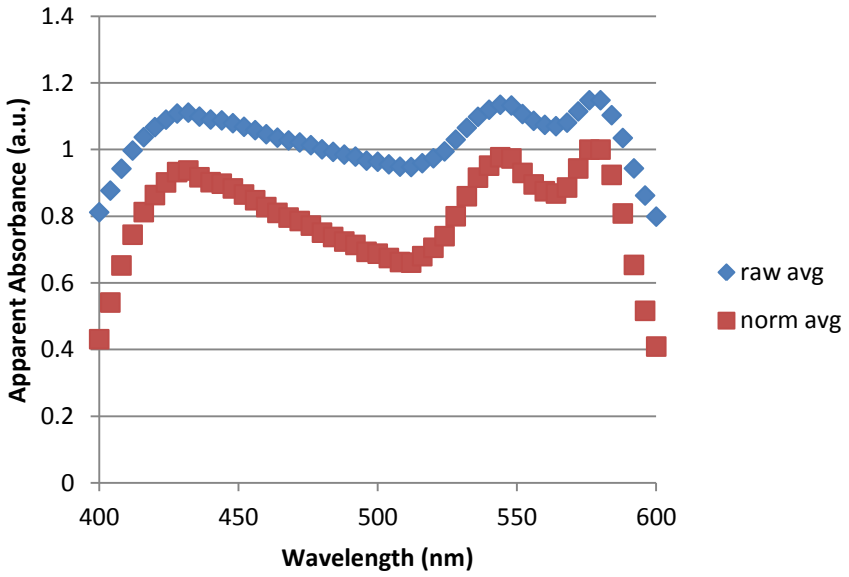

Figure 4.12 Cropped CBD reference spectra used for analysis algorithms. The unity-based normalized average was calculated from the raw average and then cropped to 400 nm to 600 nm range.

Regions of interest (RoIs) denoting the location of the common bile duct were mapped for each case, then the SAM and SID classification algorithms were applied to the data cubes for different spectral angle and divergence thresholds. False positive and false negative pixels are then counted and percentage values were then calculated.

$$N_R - C_R = F_{neg}$$

$$C - C_R = F_{pos}$$

$$\frac{F_{neg}}{N_R} = \%F_{neg}$$

$$\frac{F_{pos}}{C} = \%F_{pos}$$

where N_R is the number of RoI pixels, C is the number of pixels classified, C_R is the number of pixels classified in the RoI, F_{neg} is the number of false negative pixels, and F_{pos} is the number of false positive pixels.

Both SAM and SID can identify the CBD in 12 out of 13 cases with both normalized and non-normalized reference spectra. The effect of using a normalized reference in SAM serves to increase the spectral angle threshold required to detect the CBD with good fidelity, shifting the curves seen in Figure 4.13 to the right by 0.05 rad. SID sees no difference in required thresholding between the two reference spectra, possibly owing to the fact that the difference is essentially one of amplitude, which SID is blind to. They both have trouble detecting the CBD only with Case 2 for unknown reasons. This case is peculiar in that both algorithms identify the periphery of the CBD region more readily than they do the center, where the spectrum for the CBD should be strongest. It is possible that this might a result of the 3-dimensional geometry of the CBD in this case, but if so, this is the only case in which too much CBD signal is a problem. Case 2 is also one of the cases in which the CBD is obscured by surrounding fatty connective tissue, so the difficulty in detection could precipitate from additive spectral behavior between the CBD and the interfering tissue.

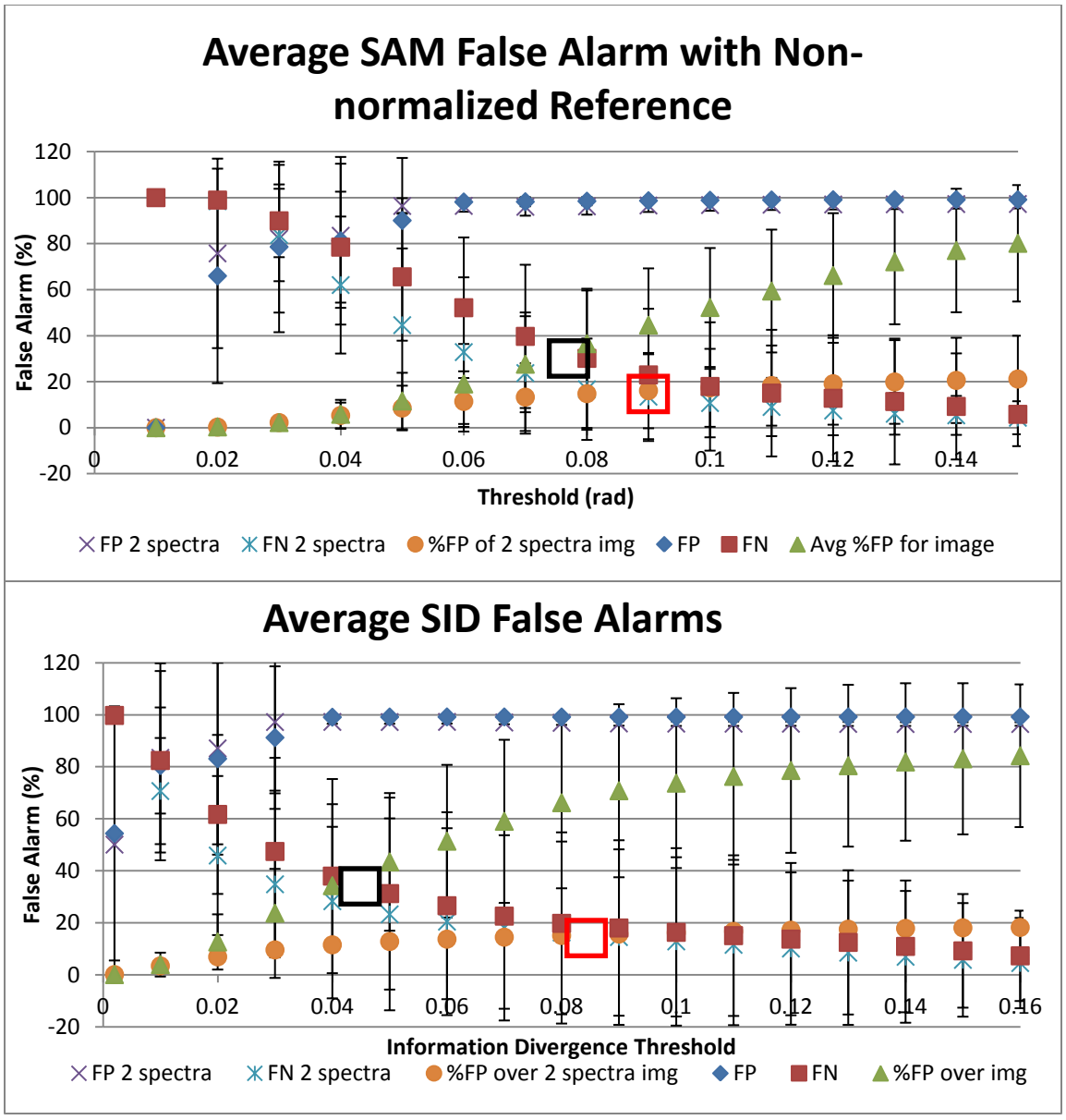

Figure 4.13: False alarm percentages for different SAM and SID thresholds using CBD reference spectra only and CBD and arterial reference spectra. The black boxes indicate optimum threshold locations for single-reference classification while red boxes indicate optimum threshold locations for two-reference classification.

Both SAM and SID produce large false positives and false negatives, percentage-wise, as shown in Figure 4.13. In order to reduce the false positives and negatives, an average arterial spectrum derived from the experimental data is added to the target spectra. The arterial spectrum has the advantage of being similar to the CBD spectrum over the spectrum subset, but still distinct. Ideally, there should be more arterial and less CBD spectrum similarity over the entire image, except for the actual location of the CBD. Indeed, when two target spectra are used, 10 out of 13 cases saw improvement over single-spectrum classification in identification by decreasing false positives and false negatives. Cases 4, 11, and 12, however, see detection interference due to the artery spectrum and a greater increase in false positives.

The optimal threshold for SAM and SID are those thresholds which minimize both false positives (FP) and false negatives (FN). For SAM, this threshold is around 0.078 radians. For SID, this threshold lies around 0.045. For both cases, this would produce an estimated false alarm percent of 30% and 35% respectively. These values are highlighted by black boxes in Figure 4.13. Both FP and FN are reduced when arterial and CBD spectra are used for classification instead of just the CBD spectrum. When calculated over the entire image instead of just the pixels classified, the reduction in percent false positive is even more obvious. This also allows for a higher optimum threshold for the minimization of false positive and false negative, particularly giving a smaller false negative, at 18% for SAM with a threshold of 0.09 radians and 15% for SID with a threshold of 0.085.

This allowance for a higher threshold can also be exemplified more obviously with the classification image, as seen in Figure 4.14. In the top row is an image that has been classified with the CBD and artery spectra and also with just the CBD spectrum. The addition of the arterial spectrum to the reference list greatly reduces the false positives in the image and allows for CBD detection at higher thresholds, since the CBD-only SAM classification image at the same threshold as the dual-classification image shows far less obvious CBD definition. SID

classification produces a very similar classification map, but there is no difference between maps produced with normalized vs. non-normalized reference spectra.

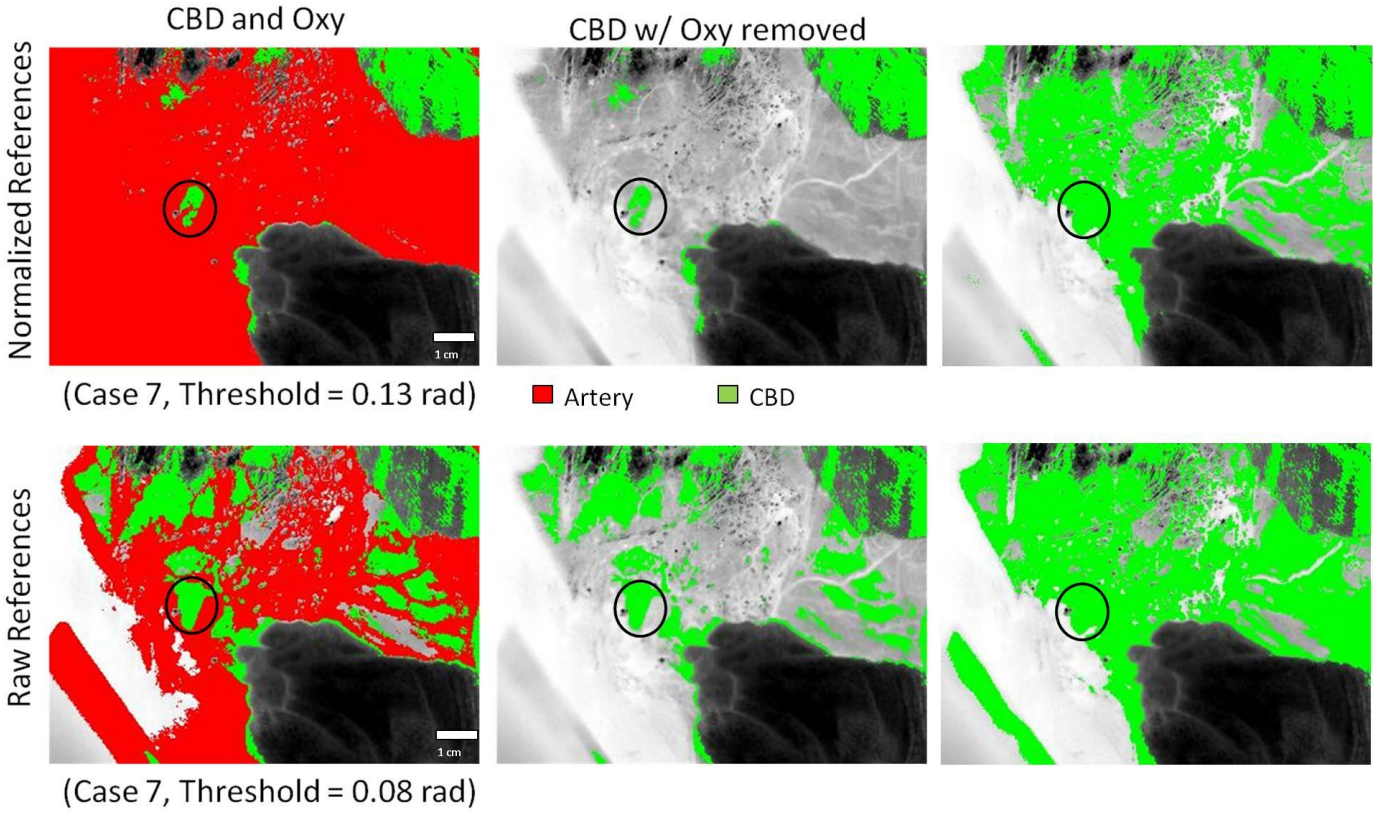

Figure 4.14 SAM images for an example case looking for the CBD spectrum only vs. the CBD spectrum plus an arterial spectrum. Normalized vs. non-normalized spectra are used. CBD locations are circled in black. The dark area in the bottom right is a surgical towel in the field of view.

4.4.4 Matched Filtering

As stated in Chapter 2, MF and its cousin MTMF are techniques for locating a target spectrum without any knowledge of the other spectra in the field of view. This can be very useful for cases in which there are many unknown spectra, but only one spectrum of importance, such as when looking for a specific vessel or organ type in a biological environment, where most spectra present are mixtures.

Unlike SAM and SID, MF and MTMF require a MNF transformation before processing. This transformation is unable to handle a data set with singularities, which are sometimes produced after ratioing the raw reflectance data with the full illumination background. Anomalous data of this sort is sometimes produced in biological data sets which encounter backscatter from the moist tissues in the field of view. Four data sets produced singularities of all the cases, so 9 out of 13 cases can be analyzed using MF and MTMF.

MF and MTMF use the MNF-transformed data and an MNF-transformed reference spectrum to seek out the target spectrum in the field of view.

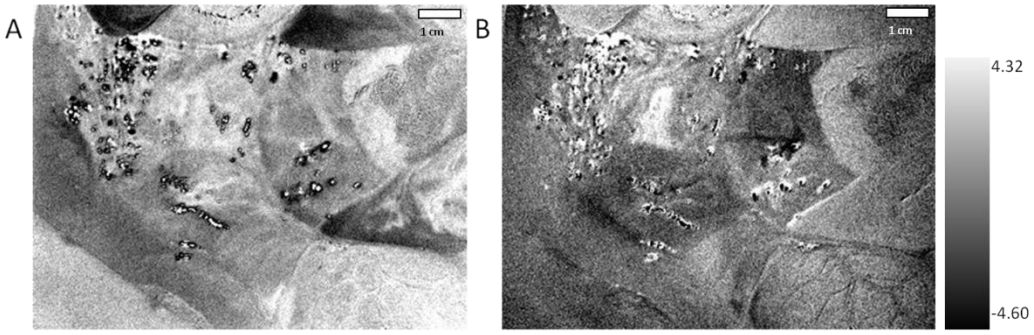

Figure 4.15 Case 2 processed with MF with normalization (A) and without normalization (B) of CBD reference spectra. A brighter area denotes better similarity to the target spectrum in arbitrary units.

As with SAM and SID, MF shows better performance when a cropped reference spectrum (400 nm to 600 nm) is used. Further improvement in detection is seen when the reference spectrum used is not a normalized one, presumably since it is closer to the non-

normalized data which is being analyzed. In addition, MF with the non-normalized reference detected the CBD in every case the normalized reference did, but with better definition. MF and MTMF also detect the CBD in Case 2 with no problem, a case with which both SAM and SID experienced difficulty. As this is the only example of MF succeeding when SAM and SID fail to properly classify the target area, no conclusion can truly be derived from that fact without more data. I would guess that the reason may be related to the 3-dimensional geometry of the scene and the obscuring fatty connective tissue somehow amplifying the CBD spectrum to a point that the differences between this CBD case and the CBD average spectrum used was no longer within the thresholds of the SAM and SID algorithms but not outside the considerations of MF.

MTMF detected the position of the CBD in 4 out of 9 cases with the non-normalized spectrum and 2 out of 9 with the normalized reference. This shows that MTMF, as with MF, generally performs better with the non-normalized reference spectrum than with a normalized reference, though in this case there was no overlap in case detection. MTMF with the non-normalized reference spectrum detected the CBD in more cases than with the normalized spectrum overall. This could indicate that MTMF is sensitive to multiplication effects, such as illumination intensity.

4.4.5 Least Squares Unmixing

Least Squares (LS) unmixing is one of the simplest methods available for unmixing hyperspectral data, as stated previously in Section 4.3.1. Based on the LMM, LS unmixes the data in a pixel-by-pixel fashion, with inputs of reference spectra and instead of single abundance values, outputs an abundance value for every pixel, creating grayscale abundance images for each reference and one image for RMS error. Higher abundance values indicate a higher presence of a reference spectrum in that pixel than other reference spectra. Lower RMS error indicates a better quality of fit associated with the reference spectra used as endmembers.

Constraints can be added to LS unmixing to improve detection characteristics, but these constraints also improve computation complexity. A fully-constrained LS analysis includes sum-to-one and non-negativity constraints. Of these two constraints, the sum-to-one is easiest to implement in ENVI and increases sensitivity and specificity over unconstrained LS, since it increases the number of pixels classified and number of true positive pixels detected while the RoI for detection remains unchanged, decreasing false negatives, but also increases RMS error. Adding a non-negativity constraint could further increase sensitivity and specificity, but due to its difficulty to implement is not explored here.

Sum-to-one constrained LS unmixing (CLS) is proven effective as a detection method when more than one reference spectrum is used to unmix the data, particularly the average CBD spectrum and the arterial spectrum used for SAM and SID. When both the average CBD and arterial spectra are used as reference, LS produced abundance images for the CBD average spectrum which vividly detected the CBD within 10 out of 13 data sets.

Detecting the CBD with classification methods, such as SAM and SID, requires only a threshold underneath which a spectrum is considered close enough to the target to be classified. It's analogous to using a searchlight, while detecting with algorithms which output abundance maps is more like using a window. There are many false positives which have too much abundance in the image to truly be the CBD. To quantify the true positives and negatives of the LS algorithm, it is empirically observed that the CBD most often falls within the 3rd quartile of the range of values over the entire abundance image. This filters out the regions with too little abundance and those with erroneously high abundance (mostly glare spots). This way of quantification produced lower false positives, but higher false negatives and lower true positives on average than SAM and SID. Further tweaking of the range of LS abundance values could change these numbers for greater accuracy. Closeness of fit was judged by RMS error values, which averaged to be 0.12 with a standard deviation of 0.07. Since most endmember estimation

algorithms estimate the number of endmembers to be in excess of 10 for each case, RMS error should decrease with the assumption of additional endmembers.

4.4.6 Detection Summary

Of the many detection methods mentioned in Table 3, most failed to be effective methods with consistent results from case to case. Four of those methods did meet with success over most cases, not including the band subtraction method, which did not require a reference spectrum for processing beyond finding the bands to add and subtract. With two options of CBD reference spectra to use, normalized and non-normalized, both were tested on the successful algorithms. These were compared with and without spectral subsets from 500 nm to 600 nm. Without the spectral subsets, only MF found the CBD location in one case.

Table 5: Detection Summary of Four Detection Algorithms with Reference Variations

CBD Identification	(out of 13)			(out of 9)
Processing	SAM	SID	LS	MF
Non-norm ref	0	0		1
Norm ref	0	0		0
Non-norm w/ spectral subset	12	12		5
Norm w/ spectral subset	12	12		2
CBD and Oxy subset refs	10	10		5
CBD and Oxy subset norm refs	5	10	10	2

False positives, false negatives, and true positives were quantified for LS and MF algorithms by counting the pixels in the CBD abundance images that fell within the third quartile of the overall range. It was observed that the CBD appeared most consistently in this range for

each image, even though the abundances vary drastically from image to image. The false alarms and true positives for SAM and SID between single-spectrum and two-spectrum are estimated from the optimal thresholds described in Figure 4.13. False alarms and true positives are displayed in the Figure 4.16.

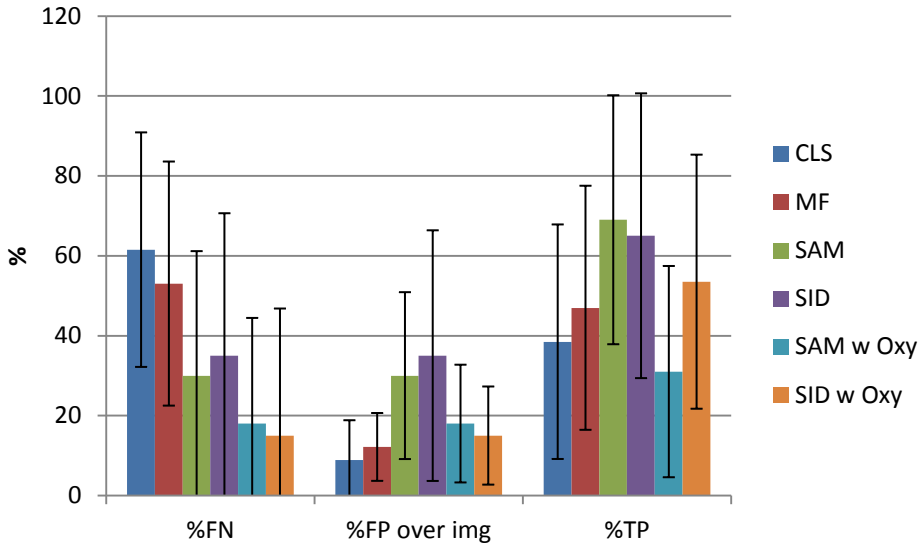

Figure 4.16: False alarms and true positives for successful algorithms averaged for every case. Error bars indicate standard deviations. SAM and SID values are from the optimal thresholds determined in Figure 4.13.

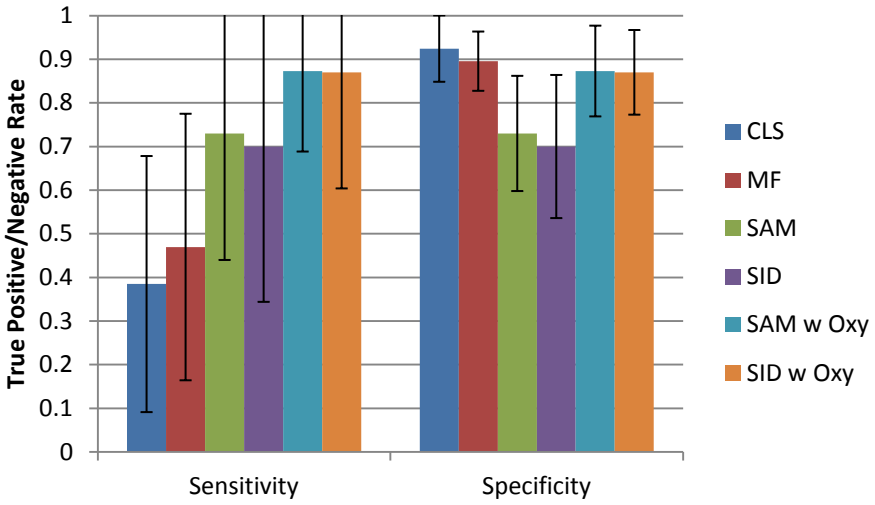

Figure 4.17: Sensitivity and specificity of all the successfully used algorithms. Error bars indicate standard deviation. SAM and SID values are taken from optimal thresholds for sensitivity and specificity.

Least Squares shows the lowest average false positive over the image at 8.9%, but the highest average false negative at 61.5%. SID with two spectral references shows the lowest false negative at 15%, but SID with only one spectrum shows the highest projected false positive at 35%. SAM with one spectrum shows the highest projected true positive at 69%. From the information in Figure 4.16, SID using two spectral references appears to be the best algorithm for high true positive and low false positive and negative.

Chapter 5

NIST Collaboration and Database Construction

As part of a collaboration with the National Institute of Standards in Technology (NIST) to validate the DLP HSI system, we've been sharing hyperspectral data with NIST for a number of years. Since not much hyperspectral data exists on *in vivo* biological tissues, we were asked to help build an optical hyperspectral database of biological tissues.

5.1 Tissue Subjects

All tissue subjects discussed in this section were collected with a DLP HSI system *in vivo* during surgery. All protocols regarding sterilization in the operating theater were followed, and the equipment and data collection caused no harm to the patient. All tissues are characterized for the visible light range, with CBD and liver data ranging from 380 nm to 780 nm at 4 nm increments, and kidney, renal cyst, and pig kidney data collected from 520 nm to 645 nm at 1 nm increments. Fat and gallbladder data were taken with both illumination schemes. All data was collected with a background brightfield image from a 99.9% reflectance target in order to calculate apparent absorbance of the tissues, as described in Chapter 3.

5.1.1 Human Tissues

Human data was collected during standard surgical procedures at UTSW in Zale and St. Paul medical centers in accordance with a general IRB (STU 082010-299) through the UTSW Department of Surgery. Every patient or their immediate family gave written consent for HSI data collection prior to imaging.

5.1.1.1 Kidney

In vivo data on oxygenated human kidneys was collected as part of a study at UTSW to determine the difference between two methods of clamping the blood vessels of a kidney prior to partial nephrectomy.[7-9,241-243] This study occurred from August 2008 to 2012 with both open and laparoscopic surgeries observed, and data on 72 human subjects collected. In the interests of time

during surgery, no deoxygenated kidney spectra were collected, so only oxygenated kidney spectra are observed here. Data was collected from 520 nm to 645 nm at 1 nm increments for the original purpose of determining tissue blood oxygenation during surgery. Since the cortical tissue of the kidney is the location of much capillary activity, the spectra collected appear to be primarily a mix of oxy- and deoxyhemoglobin.

Data taken with the laparoscopic system was collected during robotic-assisted partial nephrectomies and used sterilized 0-degree 10mm endoscopes and visible fiber optic light guides provided by the operating room. Background images of a 99.9% reflectance targets at a distance of 6 cm measured with a physical plastic tube affixed to the end of the laparoscope were taken in an enclosed, dark box. The range finder was removed and the endoscope and light guide were re-sterilized before data images were taken. Upon retrieval of the sterilized endoscope and light guide, the camera was attached to the endoscope and the assembly inserted through a sterilized plastic bag. This procedure requires two people: one to operate the computer end of the equipment, and one to remain sterilized to handle the endoscope, camera, and bag.

51 open partial nephrectomies were imaged, and 21 laparoscopic cases for a total of 72 *in vivo* human kidney data sets. The oxygenated kidney spectra appear consistent from visible to laparoscopic visible DLP systems for the purposes of determining the contribution of oxyhemoglobin during surgery.[243]

5.1.1.2 Fat

Fat is a very common component of human anatomy in the abdominal region, providing practical functions of temperature regulation and cushioning for vulnerable organs. Much fat is commonly removed during partial nephrectomies in order to reveal the kidney, either by burning or excision. Often, excess fat which does not obstruct the surgeon is left attached to or nearby the kidney when partial nephrectomy data is taken, and is therefore a common element in the field of view.

The fat spectrum, since the tissue is fed by blood vessels unassociated with the kidney shows a higher correlation to the spectrum for oxyhemoglobin than deoxyhemoglobin. It is characterized by two peaks between 545 nm and 580 nm, much like oxyhemoglobin. Fat spectral samples are taken from data sets with 520 nm to 645 nm and 380 nm to 780 nm illumination schemes.

5.1.1.3 Simple Renal Cysts

Simple Renal Cysts are collections of fluid inside the kidney, very analogous to blisters and, once the kidney and environs are exposed, quite obvious. Renal cysts develop commonly with age and are usually unthreatening, though they can contain cancerous tissue. They are usually discovered when a patient is undergoing imaging (such as CT or MRI) for some other purpose and monitored thereafter. If the cysts are deemed a problem, such as demonstrable kidney impairment by occluding collecting ducts, surgery is necessary to remove them.

With the common appearance and easy identify-ability of renal cysts, many were imaged as a byproduct of the kidney occlusion studies conducted with UTSW. Since they are comprised of mostly water and tissue, renal cysts have a very flat, deoxygenated spectrum in the region of 520 nm to 580 nm with a steep slope to 645 nm. Renal cyst spectral data is taken from 520 nm to 645 nm at 1 nm increments.

5.1.1.4 Liver

Liver data was taken as a byproduct of surgeries which targeted the CBD or gallbladder. Since the CBD enters the liver, this organ appears in several of the CBD data sets, and it is simple to sample the data from these regions. As the liver is one of the largest organs in the body and is positioned on the right side of the body, it also sometimes appears in laparoscopic kidney surgeries performed on the right kidney. Liver data is taken from 380 nm to 780 nm at 4 nm increments.

5.1.1.5 Gallbladder

Patients with gallbladders were specifically sought for the preliminary data of this study taken with the NIR DLP system, with the assumption that the gallbladder and CBD would exhibit similar spectra, since they both contain bile. Later subject targeting with the visible DLP system focused on acquiring CBD data, but occasionally caught the gallbladder in the field of view. In a few laparoscopic right partial nephrectomy surgeries, the laparoscope was positioned to capture the gallbladder in the field of view upon request. Gallbladder spectral data was primarily captured from 380 nm to 780 nm at 4 nm intervals, with one case collected from 520 nm to 645 nm at 1 nm intervals.

5.1.2 Animal Tissues

5.1.2.1 Pig

Due to the high similarity between pig anatomy and human anatomy, particularly with renal tissues, many kidney studies are performed on pigs before going forward to human trials. The open and laparoscopic partial nephrectomy cases performed with the UTSW Urology department mentioned earlier are no exception. In situ pig kidney data was collected from 520 nm to 645 nm at 1 nm intervals with the primary goal of determining percent contribution of oxyhemoglobin to deoxyhemoglobin during a period of blood vessel occlusion.[7] Spectral data collection was performed for 31 open and 19 laparoscopic cases for a total of 50 pig kidney data sets collected from 520 nm to 645 nm at 1 nm increments. 47 of these cases yielded good data.

Laparoscopic pig kidney data was collected with a very similar procedure to that used for the human data. Since the subjects were not part of survival studies, care was not taken to re-sterilize the endoscope and light guide after collecting background data. Instead of the fiber optic light guide, the liquid light guide standard to the system was used instead.

5.2 Data Formatting, Annotation, and Metadata

While most analysis at UTA was performed in MatLab, and the data is mostly stored in .dat files easily readable and manipulated by that software, other, simpler data formats are more easily read by other programs. Three-dimensional data cubes were translated from a series of .dat files to single two-dimensional ASCII files using a simple script. Assuming a few other details are known, such as the number of recorded spectral bands, these ASCII files are then easily read into the ENVI visual analysis environment for further manipulation.

To facilitate sharing of data with NIST, details about the circumstances of data collection, such as number of spectral bands, time stamps, exposure time, aperture size, spectral range of the light source, etc. are useful to know. Text files were attached to the data cubes in a standardized format containing the metadata about the data collection for ease of reading by computer scripts.

5.3 Heterogeneity and Variability for Tissue Subjects

Several characteristics were quantified for each tissue, including standard deviation of intra-subject and inter-subject spectra, characteristic peak positions and their standard deviations, number of subjects, number of data points, upper and lower wavelength limits, and the data increment. Table 6 shows the compilation of this data. Figure 5.1 shows the unity-based normalized average spectra for each tissue type.

Two illumination ranges and increments are used for tissue spectra collection. Human kidney, renal cyst, and pig kidney spectra are all collected from 520 nm to 645 nm at 1 nm increments. CBD and liver are collected over the full range of the visible DLP system from 380 nm to 780 nm at 4 nm increments. Fat and gallbladder tissue spectra were collected using both incremental imaging schemes. For fat and gallbladder, both collection ranges were averaged together for the overlapping wavelengths, and the resulting spectra have discrete breaks between the ranges between 516 nm and 520 nm and between 644 nm and 648 nm, which is an artifact of

the two collection ranges. These breaks don't appear to greatly affect the statistical differences between spectra.

Table 6: Tissue Database Statistics of Average Spectra. (H) indicates human tissue, (P) indicates pig tissue.

Tissue	Total # Subjects	N	Lower limit (nm)	Upper limit (nm)	Increment (nm)	Avg St Dev	Intra-subject St Dev	Peak 1 (nm)	Peak 1 Stdev	Peak 2 (nm)	Peak 2 Stdev	Peak 3 (nm)	Peak 3 Stdev
Kidney (H)	71	1518	520	645	1	0.176	0.080			548.215	2.140	578.651	0.846
Fat (H)	35	668	380	780	1 to 4	0.163	0.108	447.822	11.596	544.404	1.852	579.217	1.114
Renal Cyst (H)	15	231	520	645	1	0.210	0.091			549.568	4.518	577.944	2.960
CBD (H)	13	207	380	780	4	0.181	0.040	428.571	12.966	545.636	0.940	579.111	0.564
Kidney (P)	47	1109	520	645	1	0.274	0.094			547.206	3.181	578.923	1.000
Gallbladder (H)	9	169	380	780	1 to 4	0.257	0.068	475.714	1.518	545.500	1.423	577.796	0.904
Liver (H)	10	177	380	780	4	0.182	0.052	480.158	4.415	547.648	5.139	577.271	2.012

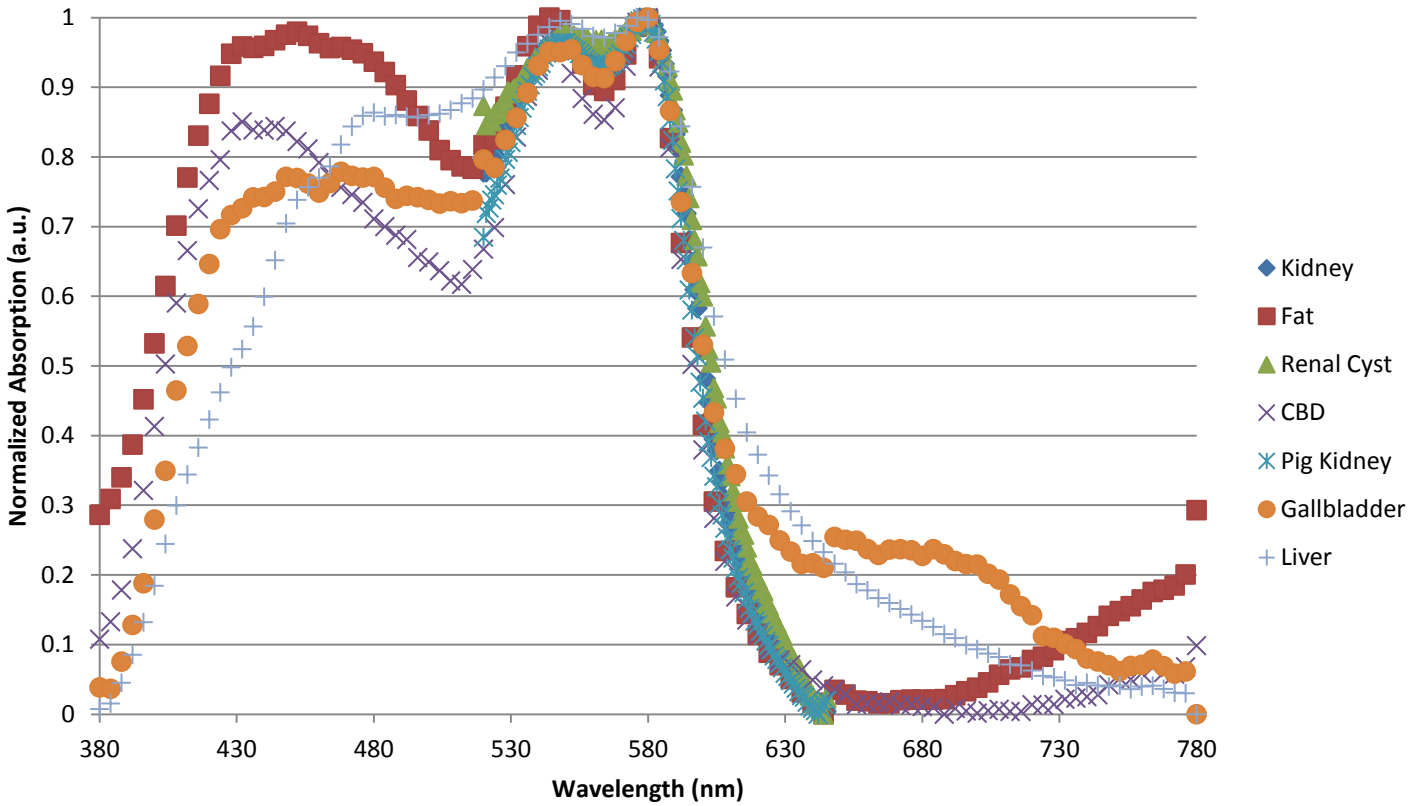

Figure 5.1: Normalized average spectra from different tissues for the range of the visible DLP HSI system. Fat, CBD, Gallbladder, and Liver spectra are collected from 380 nm to 780 nm, while Kidney, Renal Cyst, and Pig Kidney spectra are collected only from 520 nm to 645 nm.

To compute the similarity between the tissue spectra across the entire range at once, a spectral angle distance (SAD)[58] measure is used. SAD is essentially an angle value assigned to the dot product of two spectra, the basis for the SAM classification algorithm used in Chapter 4.

$$\mathrm{SAD} = \cos^{-1}\left(\frac{\langle r_i, r_j\rangle}{\|r_i\|\|r_j\|}\right)$$

where r_i and r_j represent two different spectra,

$$\langle r_i, r_j\rangle = \sum_{l=1}^{L} r_{il} r_{jl}$$

and

$$\|r_i\| = \left(\sum_{l=1}^{L} r_i^2\right)^{1/2}$$

SAD returns a single value in units of radians which represents the difference in the two input spectra. This technique was used on the spectra in Figure 5.1 on both the normalized and non-normalized versions of the average spectra (Table 7).

Table 7: SAD values for tissue database spectra comparisons

Non-Normalized Average Spectra						
	Fat	Cyst	CBD	Pig Kidney	Gallbladder	Liver
Kidney	0.0703	0.0306	0.0489	0.0159	0.0768	0.0911
Fat		0.0988	0.1109	0.0635	0.163	0.1765
Cyst			0.0458	0.0439	0.0579	0.0656
CBD				0.0494	0.0983	0.1152
Pig Kidney					0.082	0.0994
Gallbladder						0.0512
Normalized Average Spectra						
	Fat	Cyst	CBD	Pig Kidney	Gallbladder	Liver
Kidney	0.063	0.0421	0.0723	0.0361	0.1199	0.1631
Fat		0.0971	0.1191	0.0509	0.2487	0.3226
Cyst			0.1128	0.0762	0.1092	0.1361
CBD				0.0456	0.2204	0.2963
Pig Kidney					0.1352	0.1876
Gallbladder						0.163

For a SAD measure, the smaller the angle, the more similar the spectra compared are. The largest SAD in Table 7 is 0.1765 rad for the fat vs. the liver non-normalized average spectra. When the spectra are normalized, the largest angle is also between the fat and liver spectra at 0.3226 rad. The most similar spectra in Table 7 the human and pig kidney spectra at only 0.0159 rad non-normalized and 0.0361 rad with normalized spectra. This spectral similarity is to be expected, as pig kidneys behave similarly enough to human kidneys to be used for drug testing studies.

In 16 out of 21 comparisons, the SAD increased from non-normalized to normalized spectra, indicating that for most cases, normalizing the spectra magnifies the differences between spectra, in some cases doubling the SAD or more. For the other 5 spectral comparisons, such as kidney vs. fat spectra, the SAD decreases slightly, possibly indicating that the tissue spectra do not change much between their normalized and non-normalized forms for these cases, or that they both change in approximately the same way.

Spectral differentiation with SAD is based on a threshold rather than an absolute value, so depending on the variation in spectra, even spectra with a SAD as little as 0.0159 rad can be differentiated, providing the variation of the spectra around the average is small enough, so ideally a cutoff is arbitrary, and the sensitivity of it should be tested by having each compared spectra in the same field of view for several cases. The overall average standard deviations of the tissue spectra over all cases indicates a wide spread from case-to-case. Using the standard deviation of the normalized spectra, the overall standard deviations are smaller, but the maximum average standard deviation is still 16% (gallbladder), with human kidney and fat at 5%, renal cyst at 7%, CBD at 12%, pig kidney at 6%, and liver at 11%.

Using the optimal SAM threshold of 0.078 rad for non-normalized CBD spectra from Figure 4.13, it can be estimated that any spectral comparison with non-normalized spectra which produces a SAD of less than 0.078 rad can be considered similar. Since the use of a normalized

spectrum only appears to translate the SAM thresholds higher by 0.05 rad, the threshold with normalized spectra would correspondingly be 0.128 rad. By these criteria, 12 of 21 non-normalized spectral comparisons show the tissues to be similar by this measure, and 12 out of 21 comparisons using normalized spectra also fall below this threshold. If we instead use an alternate optimal SAM threshold for non-normalized spectra at 0.038 rad where the absolute false positives and negatives cross on Figure 4.13, 2 of the 21 non-normalized spectra comparisons have spectral angles below this threshold (human kidney vs. renal cyst and human kidney vs. pig kidney), and 7 out of 21 have spectral angles below the corresponding 0.088 rad threshold using normalized spectra.

Additional statistical difference measures can be performed on the tissue database spectra. P-values between two spectra can be calculated per wavelength, and the number of wavelengths that each is significantly different can be quantified. Additionally, SID measures can be used in the same way that SAD is used in this section.

Using the tissue spectra in Figure 5.1 in the same way the CBD and arterial spectra were used in Chapter 4 with SAM and SID would likely determine the tissue types in the fields of view with low false positive rates. LS and MF abundance images would be less absolute, but would likely still show the correct tissues in most cases if applied. Using cropped versions of the tissue spectra, as done with CBD in Chapter 4 may also have an impact on the comparability of spectra with SAD measures.

Using a student's T-test on the unity-based normalized spectra, with data points grouped by wavelength, a table similar to Table 7 can be made for significant p-value difference over the comparable data ranges (Table 8).

Table 8: Percent significant difference in normalized spectra ($p<0.05$) for each database tissue type.

	Fat	Renal Cyst	CBD	Pig Kidney	Gallbladder	Liver
Kidney	97.619	69.048	96.875	76.984	62.500	100.000
Fat		90.476	81.188	98.413	86.139	92.079
Renal Cyst			90.625	50.000	62.500	100.000
CBD				90.625	92.079	93.069
Pig Kidney					93.750	100.000
Gallbladder						90.099

According to the wavelength-by-wavelength t-test comparison, the tissue types with the greatest similarity (i.e. lowest percent significant difference) are human kidney and renal cyst at 69.048%, kidney and gallbladder and renal cyst and gallbladder at 62.5%, and renal cyst and pig kidney at 50% significant difference ($p< 0.05$). As renal cysts are essentially renal tissue swollen with water, kidney and renal cyst spectra are predictably similar in the visible spectrum. Human and pig kidneys are also fairly similar, but not the most similar of the spectra at 76.984% significant difference. As pigs are often used for drug testing, it was thought that human and pig kidney tissue types would be the most similar, or least significantly different, of the selected tissues, but this is not the case with this test, unlike with SAD. Besides being from different species, this is probably due to the fact that all human kidney spectra were collected under disease states (i.e. cancerous), often with some amount of lipid marbled into the fat, whereas pig kidney spectra are collected from otherwise healthy, young pigs. SAD also shows all of these spectra to be fairly similar to each other, though not in the same order of similarity.

The spectra with the least similarity, or most significantly different tissue spectra are human kidney, pig kidney, and renal cyst vs. human liver at 100% wavelengths showing significant difference at a p-value of 0.05. When looking at the average spectra, as shown in Figure 5.1, the liver spectrum does appear to be the most different from the other spectra, at least

for the ones collected from 380 nm to 780 nm, since the first peak occurs at approximately 50 nm beyond the first peaks for fat, CBD and gallbladder. Also, the liver contains a greater amount of deoxyhemoglobin than cortical kidney, which shows a capillary mix of oxy- and deoxyhemoglobin. These are also spectra which show a great difference between each other using SAD measures.

Overall, since the smallest statistical difference between tissue spectra is 50% and the largest is 100%, with most spectra falling at 62% statistical difference or greater, it is feasible that all of these tissue spectra can be adequately separated from each other in a surgical field of view, if the correct wavelength ranges are observed. Figure 5.2 shows the wavelength ranges at which each tissue spectrum exhibit statistical difference for a p-value of 0.05.

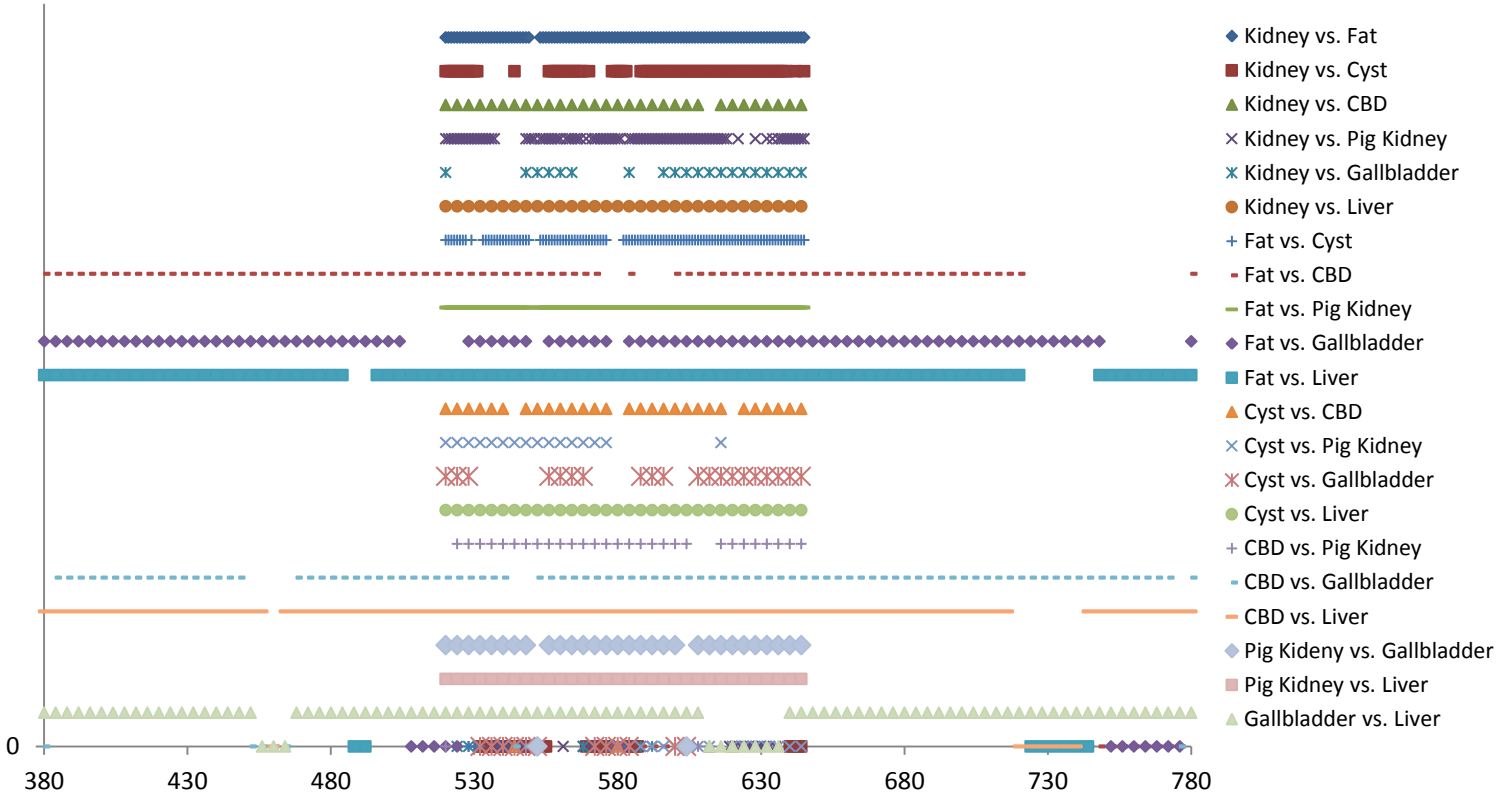

Figure 5.2: Ranges of wavelengths at which a t-test with a p-value of 0.05 indicates statistically significant difference between the normalized average tissue spectra shown in Figure 5.1. The bottom (0) line indicates the wavelengths of no significant difference.

The wavelength ranges for the least statistical significance between spectra appear to correspond most commonly to the areas around the peaks, with 7 out of 21 comparisons seeing similarity at peak 2 (approximately 545 nm) and 8 out of 21 comparisons with statistical similarity around peak 3 (approximately 578 nm). Similarity at the peaks is to be expected when comparing normalized spectra. The wavelength ranges from 380 nm to 452 nm and 644 nm to 716 nm show statistical difference for all statistical comparisons, and could therefore be the most important wavelength ranges for determining spectral differences in normalized spectra with supervised classification or unmixing hyperspectral analysis methods. Considering that those two ranges are outside the collected wavelength ranges of 3 of the 7 tissue spectra studied, they should be observed only for the tissue spectra collected for the full range.

Narrowing the wavelength range of interest from 520 nm to 645 nm, the range with the least statistical similarity appears to be between 555 nm and 568 nm, where only the human kidney vs. gallbladder spectrum shows any statistical similarity. As these two tissues are rarely in the same surgical field of view at a time, this is not a problem. Therefore the most important data range to compare spectra appears to be from 555 nm to 568 nm, so long as the total data collected falls between 545 nm to 645 nm or more in order to encompass both the maxima and minima of the spectra for proper unity-based normalization. Using non-normalized apparent absorbance spectra makes the statistical comparison subject to intensity variables which can vary wildly from case to case, making accurate tests less feasible.

Chapter 6

Conclusions and Future Directions

6.1 Overall Conclusions

In summary, this thesis has characterized an NIR DLP hyperspectral imaging system and determined its limitations, determined an average spectrum of *in vivo* human common bile duct tissue, conducted an extensive review of hyperspectral imaging analysis methods, determined which of those methods are appropriate to identify the human CBD *in vivo* using an average spectrum, and characterized many more *in vivo* biological tissue spectra for the purposes of inclusion in a biological tissue data base, a tool for future *in vivo* tissue classification.

First, the NIR DLP system needs much redesign before it can be as useful as the visible DLP system. The XE lamp, due to its spiky illumination profile and low output in the NIR range is a poor choice as a NIR source. Better options may include an incandescent QTH source or a collection of NIR LEDs. Furthermore, the OL490 tuning source has many optical elements which are not specifically designed for NIR light transmission. The only element changed from the visible OL490 to make the system NIR is the grating which illuminates the DLP chip. Many of the elements consist of glass, which is very permissible at visible wavelengths, but does not transmit well in the NIR range. These glass optics would have to be replaced by a material more tenable to NIR transmission, such as quartz or sapphire. Since these other materials are much more expensive than glass for optics (quartz cuvettes approximately 2x the price of glass (Newport.com)) plus the cost of having them replaced, the expense to make such radical changes was not justifiable for this study, especially since a visible DLP system was already in use at UTSW and showed promise for collecting results in the rest of the CBD study. An expensive price tag significantly more than the existing visible DLP system would also be unattractive to end users (surgeons), therefore the clinical relevance of data recorded in the NIR range would be less than that in the visible range. With all that in mind, I do think an appropriately developed NIR

hyperspectral imaging system for use in the operating theater should be pursued in order to better characterize in vivo tissues at wavelengths not visible to a surgeon's eye.

SID using two spectra was determined to be the best algorithm for detecting the CBD among the algorithms tested, due to good true positive and low false alarm rates. Unfortunately, the false alarms still exist and can be confusing when the anatomy in the field of view is unknown. This method may be improved if a spatial algorithm[244] can be implemented, since most CBDs in the observed cases have an oblong shape. Further confusion may also be avoided by the input of more tissue spectra of the field of view which are similar, yet distinct from the CBD.

Another drawback of the DLP HSI systems in general are that they assume computationally that the surgical field of view is a flat surface. This is an erroneous assumption, of course, since the field of view is a biological scene in open surgery with all the curved surfaces of the interior of the human body. This leads to spectral variations caused by shadow and curvature effects. Effects of shadow are a known problem in the wider field of hyperspectral imaging and is often dealt with by using a shadow spectrum in the unmixing process. In these biological fields of view, that shadow spectrum can still change from case to case, and it would have to be further characterized as with the tissue spectra in the database. To address the problem with curvature, there are many 3D modeling techniques available, such as LADAR[223,245] and grid projection[246] which could potentially be explored for use with the DLP HSI system.

6.2 Active Spectral Illumination

Sometimes referred to by a shorthand denoting how many image frames complete a data cube, i.e. the 3-shot method used to quantify oxygenated hemoglobin,[3-14, 232-234] active spectral illumination is a method for illuminating a subject area with one or more molded spectra of interest. The reflectance data gathered from each frame can then be used to calculate the presence or absence of a particular spectrum in the field of view. This method is so far unique to the DLP hyperspectral imaging platform, as its highly-configurable DMD chip is well suited to projecting

specialized, programmed spectra with high spectral resolution dependent on the spectral range of the system.

In the case of bile duct detection using active spectral illumination, three frames are recorded. The first frame is the positive component of the light profile of the difference between the average common bile duct spectrum and an arterial blood spectrum (HbO_2). The second frame is the negative component of the difference spectrum, flipped to be a positive illumination. The third frame is a brightfield illumination at 50% of the maximum intensity of the light source in order to help avoid saturation. These three frames are ratioed against each other in order to create a chemically encoded image such as the one displayed below.

$$\frac{\boldsymbol{ill_1 - ill_2}}{\boldsymbol{ill_{all}}}$$

where $\boldsymbol{ill_1}$ is the reflectance response from the first frame, $\boldsymbol{ill_2}$ is the reflectance response from the second frame, and $\boldsymbol{ill_{all}}$ is the 50% intensity brightfield illumination.

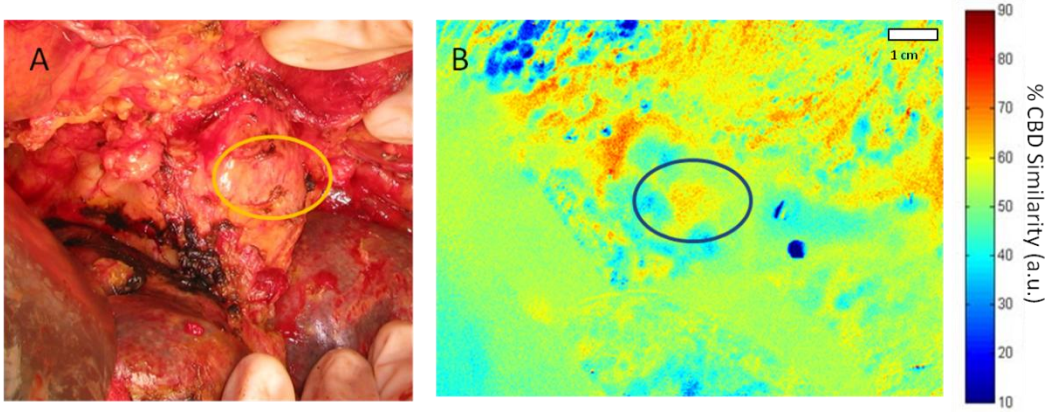

Figure 6.1 Digital photo (A) and chemically encoded image indicating the presence of CBD spectrum (B). Circled areas indicate location of the CBD as indicated by the surgeon. Images taken from Case 12. Red areas indicate a higher spectral correlation to the CBD reference spectrum.

The circled areas in the figures above denote the location of the CBD as indicated by the surgeon during data collection. Red areas in the encoded image indicate a higher correlation to the CBD spectrum, whereas blue areas indicate a spectrum closer to arterial blood. The circled area in the encoded image contains an area of high correlation to the CBD spectrum and a low correlation to the arterial spectrum, which is appropriate for a CBD obscured by other tissues and not covered in blood.

The above technique is not yet perfect, as the area of the CBD does not have the highest correlation score in the image. Time constraints of data collection and the infrequency of suitable collection opportunities limited the collection of bile duct 3-shot data to one case. With more experimentation and collection opportunities, it may be possible to further refine this technique and determine the best possible target spectra for real-time CBD detection using this method.

6.3 Future Studies

6.3.1 Expanding Spectral Database

The tissue database found here is only a foundation to a project with a much larger scope. If every tissue in the human body can be characterized in the same manner and that data made available to all hospitals, surgery risk due to misidentification of anatomy should decrease significantly. With enough subjects, patient-to-patient variability should average out, especially as the quirks and inter-subject variability becomes better understood.

The weaknesses of the spectral database as it stands is primarily the low number of subjects for several tissues, particularly liver and gallbladder for disease states undocumented past what the patient was in surgery for in the first place. Ideally, healthy tissue should also be imaged for true all-around understanding of the variation from subject-to-subject, but even without healthy tissue baseline spectra, disease state spectra are still very important to have. Further imaging of *in vivo* animal subjects may be an indicator of the healthy tissue spectra to expect, judging by the fact

that human and pig kidneys were shown to be spectrally similar by two very different similarity measures. Classification mapping by using these library absorbance spectra are hypothesized, but untested. The specific tissues are also imaged *in vivo* as opposed to *ex vivo* and exsanguinated and otherwise cleaned to separate the apparent absorbance spectra of the individual tissues from incidental other tissue spectra which dominate many *in vivo* tissue types. Taking hyperspectral data of the completely separated tissue material could serve to better understand the exact contribution of the tissue to the overall *in vivo* spectra vs. blood and other spectra which contribute to the *in vivo* spectra.

The tissue spectral database should also be extended to microscopy, particularly pathology, where the spectra potentially deviate from the macroscopic spectra studied here. I anticipate that when this spectral data is delivered in full to NIST that they can continue to add tissues to this database through contact with other collaborators.

6.3.2 Goggle Output

In early 2014, a pair of special glasses were developed to help surgical oncologists by displaying cancer tissue as a blue glow.[247] This system required the help of a contrast-enhancing fluorescence marker injected prior to surgery, which is more invasive than the discussed hyperspectral imaging systems. DLP HSI systems are no more invasive than the surgical procedure itself. If these glasses can be adapted and used in conjunction with a hyperspectral imaging output, the contrast agent can be eschewed, and the surgeon wouldn't be troubled to look at a computer screen for the output.

6.3.3 Other Clinical Studies

The visible DLP Hyperspectral Imaging System as it exists can continue to see use without alteration, as well. It has been used for studies with human retinas, burns, lower-limb neuropathy,[13] and DIEP skin flaps[229] in addition to the tissue studies presented in the database. With visible and mid-range (520 nm to 1050 nm) HSI systems in the custody of researchers at

UTSW, and a commercial system based on the current DLP HSI platform in development at Digital Light Innovations (DLi), HSI can potentially be applied to many more clinical applications. HSI is also not limited to the current system, with many other systems involving push-broom hyperspectral imaging and other data acquisition schemes in use[248] for clinical applications.

Appendix A

Estimating Number of Endmembers

Often in order to extract the endmembers from an image and unmix it correctly, the number of endmembers must be known prior to extraction. Estimating the number of endmembers is also referred to as identifying the signal subspace, with the subspace defined as the sub-set of hyperspectral data that is required for meaningful analysis. If the number of endmembers is incorrect, strongly contributing mixed spectra can be erroneously chosen as unique endmembers, and the results become unmeaningful. In the event that dimensionality reduction is required prior to data processing, estimating the number of endmembers can help determine how much to reduce the data.

Several self-contained algorithms can estimate the number of endmembers as well as the endmembers themselves, but they are computationally expensive or iterative. This section describes some popular techniques that can be used exclusively for the estimation of the number of endmembers, usually as a precursor to endmember extraction and unmixing.

Hyperspectral Signal Identification by Minimum Error (HySime)[63,249] uses a minimum mean squared error approach to infer signal subspace. This technique has several advantages including its lack of tuning parameters, computational efficiency, and the fact it requires no reference spectra (unsupervised). HySime starts by estimating the signal and noise correlation matrices using multiple regression. A subset of the eigenvectors of the signal correlation matrix which best represents the data in the minimum mean square error (MSE) sense represents the signal subspace. A two-term objective function that uses the sum of the signal projection error power (decreases with subspace dimension) and the noise projection power (increases with subspace dimension) is minimized.

Virtual Dimensionality (VD),[47, 63, 64, 135, 250] also called HFC method for the authors Harsanyi, Farrand, and Chang, is a subspace estimator which uses Neyman-Pearson detection theory-based thresholding. The eigenvalues of sample correlation and covariance matrices are

calculated and can be modified with noise whitening. Estimation is then done with the following equation,

$$\boldsymbol{S} = \frac{\mathbf{1}}{\boldsymbol{N}} \sum_{\boldsymbol{i=1}}^{\boldsymbol{N}} (\boldsymbol{x_i} - \bar{\boldsymbol{x}})(\boldsymbol{x_i} - \bar{\boldsymbol{x}})^{\boldsymbol{T}}$$

Where N is the number of pixels, $\bar{\boldsymbol{x}}$ is the mean spectral vector, and $\boldsymbol{x_i}$ is an incremental pixel spectrum. VD depends on a false alarm probability, and may underestimate the true number of endmembers when weak or anomalous endmembers are present.

VD appears to be the most popular subspace estimator, as it tends to be used with most algorithms which do not estimate the number of endmembers in the course of processing. When tested, it performs more reliably than most other methods as well.[250]

PCA uses a transform to output a set of images based off spectral variance. In order to estimate the number of endmembers, a value for the expected number must first be input. Each image has an associated eigenvalue that indicates its relevance, and the number of eigenvalues that exist above a certain threshold value should be the approximate number of endmembers present in the original image. SVD and MNF can be used for subspace size estimation in the same manner.

An Information Criterion (AIC) and Minimum Description Length (MDL)[250] are information theoretic criteria based on the logarithms of likelihood functions. The endmember number estimate is the value which minimizes the functions. These two functions depend heavily on the assumption that the noise is both independent identically distributed (iid) and Gaussian. These noise assumptions are impractical for most real-world hyperspectral data.

Eigen-based Energy[250] equations for virtual dimensionality estimation sums accumulated eigenvalues to account for the energy provided by signal sources.

$$esum(p) = \sum_{l=1}^{P} \lambda_l$$

$$energy(p) = {\sum_{l=1}^{P} \lambda_l} \Big/ {\sum_{l=1}^{L} \lambda_l}$$

where λ_l denotes the eigenvalues of the sample covariance matrix. By specifying the percent energy ($\%a$), one can find the signal subspace by finding the smallest number l which satisfies a minimum energy expression.

$$VD(\%a) = arg\left\{\min_{1\le l\le L}\left[energy(l) \ge \frac{a}{100}\right]\right\}$$

Gershgorin Radii (GR)[250] based endmember number estimation involves calculating the Gershgorin radii of the covariance and correlation matrices. For any LxL matrix X, for each row i, the Gershgorin radius is found by:

$$\rho_i = \sum_{j=1, j\neq i}^{L} |x_{ij}|$$

The eigenvalues of the sample covariance matrix and correlation matrix are registered into two classes with their corresponding eigenvectors based on their radii: signal class and noise class, where the signal class has nonzero radii and the noise class have zero radii. Only the signal classes are counted for estimating the number of endmembers.

In general, the correlation eigenvalues are greater than their corresponding covariance eigenvalues, and this holds true for the corresponding radii. The virtual dimensionality is found by finding the smallest number p that causes the difference between these two radii to be below a threshold.

Signal Subspace Estimation (SSE)[250] is based on OSP, finding the subspace spanned by the fewest sources in the mean squared error sense.

Reversible-Jump MCMC (RJ-MCMC)[177] finds the number of endmembers in parallel with finding the endmembers themselves. See the MCMC section above.

Random Matrix Theory[64] is a technique primarily used for chemical mixtures. It requires only eigenvalues robust to a confidence interval, where the largest observed eigenvalue is thought of as the largest eigenvalue of a random matrix which fulfills the following condition:

$$\nu \le \sigma^2(\mu + s(\alpha)\sigma)$$

where σ is the variance, α the significance level, μ the mean, and $s(\alpha)$an inverted Tracy-Widom distribution, and the eigenvalues ν are of a non-centered observed covariance matrix sorted in descending order. The number of endmembers K is defined so that ν_j for all pixels from 1 to K are greater than the right hand of the equation above. This technique falls short with its assumption of Gaussian noise but holds promise if the noise assumptions are revised.

Appendix B

List of Abbreviations

2-DWT: 2-Dimensional Wavelet Transform

AD: Anomaly Detection

AGES: Abundance Guided Endmember Selection

AMEE: Automated Morphological Endmember Extraction

AMM: Associative Morphological Memories

ANNs: Artificial Neural Networks

AVMAX: Alternating Volume Maximization

CAP: Competitive Agglomeration P-COMMEND

CCA: Convex Cone Analysis

CSUnSAL: Constrained Sparse Unmixing algorithm via variable Splitting and Augmented Lagrangian

DECA: Dependent Component Analysis

FCLS: Fully-Constrained Least Squares

GA: Genetic Algorithm

GR: Gershgorin Radii

HySime: Hyperspectral Signal Identification by Minimum Error

ICA: Independent Component Analysis

ICE: Iterated Constrained Endmembers

IEA: Iterative Error Analysis

KF: Kalman Filtering

Lasso: Least Absolute Shrinkage and Selection Operator

LS: Least Squares

Max-D: Maximum Distance

MCMC: Markov Chain Monte Carlo

MF: Matched Filtering

MLD: Multi-Level Detection

MLE: Maximum Likelihood Estimation

MNF: Minimum Noise Fraction

MRF: Markov Random Field

MTMF: Mixture-Tuned Matched Filtering

MVES: Minimum Volume Enclosing Simplex

MVSA: Minimum Volume Simplex Analysis

MVT: Minimum Volume Transforms

N-FINDR

NMF: Nonnegative Matrix Factorization

ORASIS: Optical Real-time Adaptive Spectral Identification System

OMP: Orthogonal Matching Pursuit

OSP: Orthogonal Subspace Projection

PCA: Principle Component Analysis

PCE: Piecewise Convex Endmember Detection

P-COMMEND: Piecewise Convex Multiple Model Endmember Detection

PMF: Positive Matrix Factorization

PP: Projection Pursuit

PPI: Pixel Purity Index

RJ-MCMC: Reversible Jump Markov Chain Monte Carlo

SAM: Spectral Angle Mapper

SFF: Spectral Feature Filtering

SID: Spectral Information Divergence

SISAL: Simplex Identification via Split Augmented Lagrangian

SMACC: Sequential Maximum Angle Convex Cone

SPICE: Sparsity-Promoting Iterated Constrained Endmembers

SPP: Spatial Pre-Processing

SSEE: Spatial-Spectral Endmember Extraction

SUnSAL: Sparse Unmixing algorithm via variable Splitting and Augmented Lagrangian

SVD: Singular Value Decomposition

SVMs: Support Vector Machines

VCA: Vertex Component Analysis

VD: Virtual Dimensionality

References

1. Fox SI. *Human Physiology*. 10th ed. McGraw-Hill, NY. 2008.
2. Kapoor VK. Bile duct injury repair: when? what? who? *J. HBP Surj.* 2007; 14(5): 476-479.
3. Zuzak KJ, Naik SC, Alexandrakis G, Hawkins D, Behbehani K, Livingston EH. Intraoperative bile duct visualization using near-infrared hyperspectral video imaging. *Anal Chem*. 2007; 79: 4709-4715.
4. Zuzak K, Naik S, Alexandrakis G, Hawkins D, Behbehani K, Livingston E. Characterization of a Near-Infrared Laparoscopic Hyperspectral Imaging System for Minimally Invasive Surgery. *Am. J. Surg.* 2008; 195: 291-497.
5. Zuzak KJ, Francis RP, Wehner EF, Litorja M, Cadeddu JA, Livingston EH. Active DLP® Hyperspectral Illumination: A Noninvasive, In Vivo, System Characterization Visualizing Tissue Oxygenation at Near Video Rates. *Anal Chem*. 2011; 83(19); 7424–7430.
6. Zuzak KJ, Francis RP, Wehner EF, et al. Hyperspectral imaging utilizing LCTF and DLP technology for surgical and clinical applications. *Proc. SPIE*. 2009; 7170.
7. Tracy CR, Terrel JD, Francis RP, et al. Characterization of Renal Ischemia Using DLP® Hyperspectral Imaging: A Pilot Study Comparing Artery-Only Occlusion Versus Artery and Vein Occlusion. *J. Endourology.* 2010; 24(3): 321-325.
8. Olweny EO, Tan YK, Faddegon S, et al. Evaluation of a novel laparoscopic camera for characterization of renal ischemia in a porcine model using digital light processing (DLP) hyperspectral imaging. *Proc. SPIE*. 2012; 8254; 82540.
9. Best SL, Thapa A, Holzer MS, et al. Assessment of renal oxygenation during partial nephrectomy using DLP hyperspectral imaging. *Proc. SPIE*. 2011; 7932.

10. Mangum ML, Saint-Cyr M, Wehner EF, Thapa A, Livingston E, Zuzak KJ. Visible to NIR DLP hyperspectral imaging system for surgical utility using inherent chromophores and fluorescent probes. *Proc. SPIE.* 2011; 7932.

11. Wehner E, Thapa A, Livingston E, Zuzak K. NIR DLP hyperspectral imaging system for medical applications. *Proc. SPIE*. 2011; 7932.

12. Allen DW, Rice JP, Wehner E, et al. An examination of spectral diversity of medical scenes for hyperspectral projection. *Proc. SPIE*. 2011; 7932.

13. Zuzak KJ, Wehner E, Rao S, et al. The robustness of DLP hyperspectral imaging for clinical and surgical utility. *Proc. SPIE.* 2010; 7596: 759604.

14. Zuzak KJ, Francis RP, Wehner EF, et al. DLP hyperspectral imaging for surgical and clinical utility. *Proc. SPIE*. 2009; 7210, 721006.

15. Jia S, Qian Y. Constrained nonnegative matrix factorization for hyperspectral unmixing. *IEEE Trans Geosci Remote Sens.* 2009;47(1):161-173.

16. Ifarraguerri A, Chang C. Projection pursuit analysis of hyperspectral scenes. *Proc SPIE.* 1998;3372 51-59.

17. Ifarraguerri A, Chang C. Unsupervised hyperspectral image analysis with projection pursuit. *IEEE Trans Geosci Remote Sens.* 2000;38(6).

18. Winter ME. N-FINDR: An algorithm for fast autonomous spectral end-member determination in hyperspectral data. *Proc SPIE.* 1999;3753(226).

19. Winter ME. Comparison of approaches for determining end-members in hyperspectral data. *Aerospace Conference Proceedings, 2000 IEEE.* 2000;3:305-313 vol.3.

20. Le Mouelic S, Combe J-, Sarago V, et al. An iterative least squares approach to decorrelate minerals and ices contributions in hyperspectral images: Application to cuprite (earth) and mars. *Hyperspectral Image and Signal Processing: Evolution in Remote Sensing, 2009 WHISPERS '09 First Workshop on.* 2009:1-4.

21. Combe J-, Le Mouélic S, Sotin C, et al. Analysis of OMEGA/Mars express data hyperspectral data using a multiple-endmember linear spectral unmixing model (MELSUM): Methodology and first results. *Planet Space Sci.* 2008;56(7):951-975. doi: DOI: 10.1016/j.pss.2007.12.007.

22. Maerker J, Huber J, Middelmann W. Unmixing and anomaly detection in hyperspectral data due to cluster variation and local information. *Proc SPIE.* 2010;7695. doi:10.1117/12.850293.

23. Szu HH, Ren H. Unified lagrangian neural network method for subpixel classification in hyperspectral imagery. *Proc SPIE.* 2001;4391(1):314-329. http://link.aip.org/link/?PSI/4391/314/1.

24. Broadwater J, Chellappa R, Banerjee A, Burlina P. Kernel fully constrained least squares abundance estimates. *Geoscience and Remote Sensing Symposium, 2007 IGARSS 2007 IEEE International.* 2007:4041-4044.

25. Barducci A, Mecocci A. Theoretical and experimental assessment of noise effects on least-squares spectral unmixing of hyperspectral images. *Opt Eng.* 2005;44(8):087008. http://link.aip.org/link/?JOE/44/087008/1.

26. Keenan MR, Timlin JA, Van Benthem MH, Haaland DM. Algorithms for constrained linear unmixing with application to the hyperspectral analysis of fluorophore mixtures. *Proc SPIE.* 2002;4816(1):193-202. http://link.aip.org/link/?PSI/4816/193/1.

27. Ren H, Fang JP, Chang YL. Signature reduction methods for target detection in multispectral remote sensing imagery. *Proc SPIE.* 2006;6378(1):63781E. http://link.aip.org/link/?PSI/6378/63781E/1.

28. Scholl JF, Hege EK, Lloyd-Hart M, Dereniak EL. Figure of merit calculations for spectral unmixing and classification algorithms. *Proc SPIE.* 2006;6315(1):63150H. http://link.aip.org/link/?PSI/6315/63150H/1.

29. Scholl JF, Hege EK, Lloyd-Hart M, Dereniak EL. Hyperspectral feature classification with alternate wavelet transform representations. *Proc SPIE.* 2006;6315(1):63150G. http://link.aip.org/link/?PSI/6315/63150G/1.

30. Sirkeci B, Brady D, Burman J. Restricted total least squares solutions for hyperspectral imagery. *Acoustics, Speech, and Signal Processing, 2000 ICASSP '00 Proceedings 2000 IEEE International Conference on.* 2000;1:624-627 vol.1.

31. Villa A, Chanussot J,Benediktsson J, Jutten C. Supervised super-resolution to improve the resolution of hyperspectral images classification maps. *Proc SPIE.* 2010;7830(78300J). doi: 10.1117/12.864938.

32. Winter EM, Schlangen MJ, Hill AB, Simi CG, Winter ME. Tradeoffs for real-time hyperspectral analysis. *Proc SPIE.* 2002;4725(1):366-371. http://link.aip.org/link/?PSI/4725/366/1.

33. Zavaljevski A, Dhawan AP, Kelch DJ, Riddell III J. Multilevel detection method for multispectral and hyperspectral images. *Proc SPIE.* 1995;2484(1):604-614. http://link.aip.org/link/?PSI/2484/604/1.

34. Zhao L, Zhang K. A new least squares subspace projection approach to unmix hyperspectral data. *Intelligent Systems, 2009 GCIS '09 WRI Global Congress on.* 2009;4:350-354.

35. Haaland D, Melgaard D. New augmented classical least squares methods for improved quantitative spectral analyses. *Vibrational Spectroscopy.* 2002;29:171-75.

36. Tu T, Chen C, Chang C. A posteriori least squares orthogonal subspace projection approach to desired signature extraction and detection. *IEEE Trans Geosci Remote Sens.* 1997;35(1):127-139.

37. Miao L, Qi H, Szu H. A maximum entropy approach to unsupervised mixed-pixel decomposition. *IEEE Trans Image Process.* 2007;16(4):1008-1021.

38. Grana M, Moreno R, Albizuri FX. Convex coordinates based on lattice independent sets as pattern features. *Fuzzy Systems, 2006 IEEE International Conference on.* 2006:225-230.

39. Jia G, Zhao H, Li N. Automatic spectral unmixing of hyperspectral data before radiation correction: Application to PHI data. *Geoscience and Remote Sensing Symposium, 2006 IGARSS 2006 IEEE International Conference on.* 2006:932-935.

40. Barducci A, Mecocci A, Alamanno C, Pippi I, Marcoionni P. Multi-resolution least-squares spectral unmixing algorithm for subpixel classification of hyperspectral images. *Geoscience and Remote Sensing Symposium, 2003 IGARSS '03 Proceedings 2003 IEEE International.* 2003;3:1799-1801.

41. Bednarkiewicz A, Whelan MP. Microscopic fluorescence lifetime and hyperspectral imaging with digital micromirror illuminator. *Proc SPIE.* 2007;6630(1):66300A. http://link.aip.org/link/?PSI/6630/66300A/1.

42. Broadwater J, Meth R, Chellappa R. A hybrid algorithm for subpixel detection in hyperspectral imagery. *Geoscience and Remote Sensing Symposium, 2004 IGARSS '04 Proceedings 2004 IEEE International.* 2004;3:1601-1604 vol.3.

43. Chen J, Jia X, Yang W, Matsushita B. Generalization of subpixel analysis for hyperspectral data with flexibility in spectral similarity measures. *IEEE Trans Geosci Remote Sens.* 2009;47(7):2165-2171.

44. Chen X, Chen J, Jia X, Wu J. Impact of collinearity on linear and nonlinear spectral mixture analysis. *Hyperspectral Image and Signal Processing: Evolution in Remote Sensing (WHISPERS), 2010 2nd Workshop on.* 2010:1-4.

45. Du Q, Chang C. Linear mixture analysis-based compression for hyperspectral image analysis. *IEEE Trans Geosci Remote Sens.* 2004;42(4):875-891.

46. Endsley NH. Spectral unmixing algorithms based on statistical models. *Proc SPIE.* 1995;2480(1):23-36. http://link.aip.org/link/?PSI/2480/23/1.

47. Farzam M, Beheshti S, Raahemifar K. Calculation of abundance factors in hyperspectral imaging using genetic algorithm. *Electrical and Computer Engineering, 2008 CCECE 2008 Canadian Conference on.* 2008:000837-000842.

48. Gross HN, Schott JR. Application of spatial resolution enhancement and spectral mixture analysis to hyperspectral images. *Proc SPIE.* 1996;2821(1):30-41. http://link.aip.org/link/?PSI/2821/30/1.

49. Gu Y, Zhang Y, Zhang J. Integration of spatial-spectral information for resolution enhancement in hyperspectral images. *IEEE Trans Geosci Remote Sens.* 2008;46(5) 1347-1358.

50. Guo Z, Wittman T, Osher S. L1 unmixing and its application to hyperspectral image enhancement. *Proc SPIE.* 2009. doi: 10.1117/12.818245.

51. Heinz DC, Chang C. Fully constrained least squares linear spectral mixture analysis method for material quantification in hyperspectral imagery. *IEEE Trans Geosci Remote Sens.* 2001;39(3) 529-545.

52. Heinz DC, Chein-I Chang. Real-time processing of an unsupervised constrained linear spectral unmixing algorithm. *Geoscience and Remote Sensing Symposium, 2001 IGARSS '01 IEEE 2001 International.* 2001;1:372-374 vol.1.

53. Kempeneers P, De Backer S, Provoost S, Debruyn W, Scheunders P. Hyperspectral classification applied to the belgian coastline. *Proc SPIE.* 2005;5982(1):59820F. http://link.aip.org/link/?PSI/5982/59820F/1.

54. Kerekes J, Farrar K, Keshava N. Linear unmixing performance forecasting. *Geoscience and Remote Sensing Symposium, 2002 IGARSS '02 2002 IEEE International.* 2002;3:1676-1678 vol.3.

55. Li J, Bruce LM. Improving the accuracy of linear pixel unmixing via appropriate endmember dimensionality reduction. *Advances in Techniques for Analysis of Remotely Sensed Data, 2003 IEEE Workshop on.* 2003:157-162.

56. Mianji FA, Gu Y, Zhang Y, Zhang J. Enhanced self-training superresolution mapping technique for hyperspectral imagery. *Geoscience and Remote Sensing Letters, IEEE.* 2011;PP(99):671-675.

57. Jiao X, Chang CI. Unsupervised hyperspectral target analysis. *Proc SPIE.* 2008;7086(1):70860P. http://link.aip.org/link/?PSI/7086/70860P/1.

58. Kwan C, Ayhan B, Chen G, Jing Wang, Baohong Ji, Chein-I Chang. A novel approach for spectral unmixing, classification, and concentration estimation of chemical and biological agents. *IEEE Trans Geosci Remote Sens.* 2006;44(2):409-419.

59. Martin G, Gonzalez-Ruiz V, Plaza A, Ortiz J, Garcia I. Impact of JPEG2000 compression on endmember extraction and unmixing of remotely sensed hyperspectral data. *J Appl Remote Sens.* 2010;4(041796). doi: 10.1117/1.3474975.

60. Sánchez S, Martín G, Plaza A, Chang C. GPU implementation of fully constrained linear spectral unmixing for remotely sensed hyperspectral data exploitation. *Proc SPIE.* 2010;7810(78100G). doi: 10.1117/12.860775.

61. Winter ME, Lucey PG, Steutel D. Examining hyperspectral unmixing error reduction due to stepwise unmixing. *Proc SPIE.* 2003;5093(1):380-389. http://link.aip.org/link/?PSI/5093/380/1.

62. Zavaljevski A, Dhawan AP, Kelch DJ, Riddell III J. Adaptive multilevel classification and detection in multispectral images. *Opt Eng.* 1996;35(10):2884-2893. http://link.aip.org/link/?JOE/35/2884/1.

63. Bioucas-Dias J, Plaza A. Hyperspectral unmixing: Geometrical, statistical, and sparse regression-based approaches. *Proc SPIE.* 2010;7830(78300A). doi: 10.1117/12.870780.

64. Cawse K, Sears M, Robin A, et al. Using random matrix theory to determine the number of endmembers in a hyperspectral image. *Hyperspectral Image and Signal Processing: Evolution in Remote Sensing (WHISPERS), 2010 2nd Workshop on.* 2010:1-4.

65. Zare A, Gader P. Context-based endmember detection for hyperspectral imagery. *Hyperspectral Image and Signal Processing: Evolution in Remote Sensing, 2009 WHISPERS '09 First Workshop on.* 2009:1-4.

66. Zare A, Gader P. Sparsity promoting iterated constrained endmember dectection in hyperspectral imagery. *IEEE Geoscience and Remote Sensing Letters.* 2007.

67. Berman M. Some unmixing problems and algorithms in spectroscopy and hyperspectral imaging. *Applied Imagery and Pattern Recognition Workshop, 2006 AIPR 2006 35th IEEE.* 2006:15-15.

68. Dobigeon N, Achard V. Performance comparison of geometric and statistical methods for endmembers extraction in hyperspectral imagery. *Proc SPIE.* 2005;5982(1):598213. http://link.aip.org/link/?PSI/5982/598213/1.

69. Zymnis A, Kim S-, Skaf J, Parente M, Boyd S. Hyperspectral image unmixing via alternating projected subgradients. *Signals, Systems and Computers, 2007 ACSSC 2007 Conference Record of the Forty-First Asilomar Conference on.* 2007:1164-1168.

70. Roessner S, Segl K, Heiden U, Kaufmann H. Automated differentiation of urban surfaces based on airborne hyperspectral imagery. *IEEE Trans Geosci Remote Sens.* 2001;39(7):1525-1532.

71. McDonald S, Niemann KO, Goodenough DG. Development of hyperspectral biochemistry through the use of statistical modeling and spectral unmixing. *Geoscience and Remote Sensing Symposium, 2004 IGARSS '04 Proceedings 2004 IEEE International.* 2004;2:1007-1009 vol.2.

72. Jin J, Wang B, Zhang L. A novel approach based on fisher discriminant null space for decomposition of mixed pixels in hyperspectral imagery. *Geoscience and Remote Sensing Letters, IEEE.* 2010;7(4):699-703.

73. Villa A, Chanussot J, Benediktsson J, Jutten C. Spectral unmixing for the classification of hyperspectral images at a finer spatial resolution. *IEEE J Sel Top Signal Process*. 2010;PP(99):1-1.

74. Shoshany M, Kizel F, Netanyahu NS, Goldshlager N, Jarmer T, Even-Tzur G. An iterative search in end-member fraction space for spectral unmixing. *Geoscience and Remote Sensing Letters, IEEE.* 2011;PP(99):706-709.

75. Chan T, Chi C, Huang Y, Ma W. A convex analysis-based minimum-volume enclosing simplex algorithm for hyperspectral unmixing. *IEEE Trans Signal Process.* 2009;57(11):4418-4432.

76. Zare A, Gader P. PCE: Piecewise convex endmember detection. *IEEE Trans Geosci Remote Sens.* 2010;48(6):2620-2632.

77. Zare A, Bchir O, Frigui H, Gader P. Spatially-smooth piece-wise convex endmember detection. *Hyperspectral Image and Signal Processing: Evolution in Remote Sensing (WHISPERS), 2010 2nd Workshop on.* 2010:1-4.

78. Ifarraguerri A, Chang C-. Multispectral and hyperspectral image analysis with convex cones. *IEEE Trans Geosci Remote Sens.* 1999;37(2):756-770.

79. Chan T, Ma W, Chi C, ArulMurugan A. Hyperspectral unmixing from a convex analysis and optimization perspective. *Hyperspectral Image and Signal Processing: Evolution in Remote Sensing, 2009 WHISPERS '09 First Workshop on.* 2009:1-4.

80. Bi D, Zhao L, Gong Y. The mathematical model of the endmembers in hyperspectral data. *Environmental Science and Information Application Technology, 2009 ESIAT 2009 International Conference on.* 2009;2:609-613.

81. Ambikapathi A, Chan T, Ma W, Chi C. A robust alternating volume maximization algorithm for endmember extraction in hyperspectral images. *Hyperspectral Image and Signal Processing: Evolution in Remote Sensing (WHISPERS), 2010 2nd Workshop on.* 2010:1-4.

82. Ambikapathi A, Chan T, Ma W, Chi C. A robust minimum volume enclosing simplex algorithm for hyperspectral unmixing. *Acoustics Speech and Signal Processing (ICASSP), 2010 IEEE International Conference on.* 2010:1202-1205.

83. Nascimento JMP, Dias JMB. Vertex component analysis: A fast algorithm to unmix hyperspectral data. *IEEE Trans Geosci Remote Sens.* 2005;43(4):898-910.

84. Hendrix EMT, Garcia I, Plaza J, Plaza A. Minimum volume simplicial enclosure for spectral unmixing of remotely sensed hyperspectral data. *Geoscience and Remote Sensing Symposium (IGARSS), 2010 IEEE International.* 2010:193-196.

85. Heylen R, Burazerovic D, Scheunders P. Non-linear spectral unmixing by geodesic simplex volume maximization. *IEEE J Sel Top Signal Process.* 2010;PP(99):1-1.

86. Luo B, Chanussot J. Hyperspectral image classification based on spectral and geometrical features. *Machine Learning for Signal Processing, 2009 MLSP 2009 IEEE International Workshop on.* 2009:1-6.

87. Luo B, Chanussot J. Unsupervised classification of hyperspectral images by using linear unmixing algorithm. *Image Processing (ICIP), 2009 16th IEEE International Conference on.* 2009:2877-2880.

88. Luo W. Parallel VCA algorithm for hyperspectral remote sensing image in SMP cluster environment. *Image and Signal Processing (CISP), 2010 3rd International Congress on.* 2010;5:2216-2220.

89. Martín G, Plaza A. Spatial-spectral preprocessing for volume-based endmember extraction algorithms using unsupervised clustering. *Hyperspectral Image and Signal*

Processing: Evolution in Remote Sensing (WHISPERS), 2010 2nd Workshop on. 2010:1-4.

90. Parente M, Plaza A. Survey of geometric and statistical unmixing algorithms for hyperspectral images. *Hyperspectral Image and Signal Processing: Evolution in Remote Sensing (WHISPERS), 2010 2nd Workshop on.* 2010:1-4.

91. Zare A, Bchir O, Frigui H, Gader P. A comparison of deterministic and probabilistic approaches to endmember representation. *Hyperspectral Image and Signal Processing: Evolution in Remote Sensing (WHISPERS), 2010 2nd Workshop on.* 2010:1-4.

92. Bateson C, Asner G, Wessman C. Endmember bundles: a new approach to incorporating endmember variability into spectral mixture analysis. *IEEE Trans Geosci Remote Sens.* 2000;38(2) 1083-1094.

93. Craig M. Minimum-volume transforms for remotely sensed data. *IEEE Trans Geosci Remote Sens.* 1994;32(3) 542-552.

94. Haq N, Sarigul E, Alam MS. An automated method for pattern recognition using linear mixing model and vertex component analysis. *Proc SPIE.* 2006;6313(1):63130I. http://link.aip.org/link/?PSI/6313/63130I/1.

95. Winter EM. Requirements for anomaly detection in hyperspectral data using spectral unmixing. *Signals, Systems and Computers, 2000 Conference Record of the Thirty-Fourth Asilomar Conference on.* 2000;1:174-176 vol.1.

96. Winter EM. The development of a hyperspectral sensor: A data processing viewpoint. *Aerospace Conference, 2001, IEEE Proceedings.* 2001;4:4/1979-4/1984 vol.4.

97. Chowdhury A, Alam MS. Fast implementation of N-FINDR algorithm for endmember determination in hyperspectral imagery. *Proc SPIE.* 2007;6565(1):656526. http://link.aip.org/link/?PSI/6565/656526/1.

98. Chang C, Wu C, Tsai C. Random N-finder (N-FINDR) endmember extraction algorithms for hyperspectral imagery. *IEEE Trans Image Process.* 2010;PP(99):1-1.

99. Dowler S, Andrews M. Abundance guided endmember selection: An algorithm for unmixing hyperspectral data. *Image Processing (ICIP), 2010 17th IEEE International Conference on.* 2010:2649-2652.

100. Sánchez S, Martín G, Plaza A. Parallel implementation of the N-FINDR endmember extraction algorithm on commodity graphics processing units. *Geoscience and Remote Sensing Symposium (IGARSS), 2010 IEEE International.* 2010:955-958.

101. Zortea M, Plaza A. A quantitative and comparative analysis of different implementations of N-FINDR: A fast endmember extraction algorithm. *Geoscience and Remote Sensing Letters, IEEE.* 2009;6(4):787-791.

102. Bioucas-Dias JM. A variable splitting augmented lagrangian approach to linear spectral unmixing. *Hyperspectral Image and Signal Processing: Evolution in Remote Sensing, 2009 WHISPERS '09 First Workshop on.* 2009:1-4.

103. Iordache M-, Bioucas-Dias JM, Plaza A. Sparse unmixing of hyperspectral data. *IEEE Trans Geosci Remote Sens.* 2011;PP(99):1-26.

104. Iordache M, Plaza A, Bioucas-Dias J. Recent developments in sparse hyperspectral unmixing. *Geoscience and Remote Sensing Symposium (IGARSS), 2010 IEEE International.* 2010:1281-1284.

105. Iordache M-, Plaza A, Bioucas-Dias J. On the use of spectral libraries to perform sparse unmixing of hyperspectral data. *Hyperspectral Image and Signal Processing: Evolution in Remote Sensing (WHISPERS), 2010 2nd Workshop on.* 2010:1-4.

106. Kwong JD, Messinger DW, Middleton WD. Hyperspectral clustering and unmixing for studying the ecology of state formation and complex societies. *Proc SPIE.* 2009. doi: 10.1117/12.826354.

107. Schott J, Lee K, Raqueno R, Hoffmann G, Healey G. A subpixel target detection technique based on the invariance approach. *AVIRIS Airborne Geoscience workshop Proceedings.* 2003.

108. Bachmann M, Mueller A, Habermeyer M, Dech S. An iterative unmixing approach in support of fractional cover estimation in semi-arid environments. *Proc SPIE.* 2004;5574(1):205-213. http://link.aip.org/link/?PSI/5574/205/1.

109. Boisvert AR, Villeneuve PV, Stocker AD. Endmember finding and spectral unmixing using least-angle regression. *Proc SPIE.* 2010;7695(76951N). doi: 10.1117/12.850601.

110. Kruse FA. Predictive subpixel spatial/spectral modeling using fused HSI and MSI data. *Proc SPIE.* 2004;5425(1):414-424. http://link.aip.org/link/?PSI/5425/414/1.

111. Nikolakopoulos KG, Karathanassi V, Rokos D. Hyperspectral data and methods for coastal water mapping. *Proc SPIE.* 2006;6359(1):63590I. http://link.aip.org/link/?PSI/6359/63590I/1.

112. Ball JE, Kari S, Younan NH. Hyperspectral pixel unmixing using singular value decomposition. *Geoscience and Remote Sensing Symposium, 2004 IGARSS '04 Proceedings 2004 IEEE International.* 2004;5:3253-3256 vol.5.

113. Grana M, Gallego J, Hernandez C. Further results on AMM for endmember induction. *Advances in Techniques for Analysis of Remotely Sensed Data, 2003 IEEE Workshop on.* 2003:237-243.

114. Li J, Bioucas-Dias JM. Minimum volume simplex analysis: A fast algorithm to unmix hyperspectral data. *Geoscience and Remote Sensing Symposium, 2008 IGARSS 2008 IEEE International.* 2008;3:III - 250-III - 253.

115. Zare A, Gader P. L1-endmembers: A robust endmember detection and spectral unmixing algorithm. *Proc SPIE.* 2010;7695(76951L). doi: 10.1117/12.851065.

116. Sánchez S, Martín G, Paz A, Plaza A, Plaza J. Near real-time endmember extraction from remotely sensed hyperspectral data using Nvidia GPUs. *Proc SPIE.* 2010;7724. doi: 10.1117/12.854365.

117. Winter EM, Lucey PG, Winter ME. The analysis of data from a thermal infrared hyperspectral instrument. *Proc SPIE.* 2001;4151 256-264.

118. Wu CC, Chang CI. Automatic algorithms for endmember extraction. *Proc SPIE.* 2006;6302(1):63020E. http://link.aip.org/link/?PSI/6302/63020E/1.

119. Masalmah YM, Velez-Reyes M. Unsupervised unmixing of hyperspectral imagery. *Circuits and Systems, 2006 MWSCAS '06 49th IEEE International Midwest Symposium on.* 2006;2:337-341.

120. Marin JA, Brockhaus J, Rolf J, Shine J, Schafer J, Balthazor A. Assessing band selection and image classification techniques on HYDICE hyperspectral data. *Systems, Man, and Cybernetics, 1999 IEEE SMC '99 Conference Proceedings 1999 IEEE International Conference on.* 1999;1(1):1067-1072.

121. Mianji FA, Ye Zhang, Babakhani A. Superresolution of hyperspectral images using backpropagation neural networks. *Nonlinear Dynamics and Synchronization, 2009 INDS '09 2nd International Workshop on.* 2009:168-174.

122. Chang YCC, Ren H, Chang CI, Rand RS. How to design synthetic images to validate and evaluate hyperspectral imaging algorithms. *Proc SPIE.* 2008;6966(1):69661P. http://link.aip.org/link/?PSI/6966/69661P/1.

123. Plaza A, Chang CI, Plaza J, Valencia D. Commodity cluster and hardware-based massively parallel implementations of hyperspectral imaging algorithms. *Proc SPIE.* 2006;6233(1):623316. http://link.aip.org/link/?PSI/6233/623316/1.

124. Plaza J, Plaza A, Martín G. A fast sequential endmember extraction algorithm based on unconstrained linear spectral unmixing. *Proc SPIE.* 2009. doi: 10.1117/12.830734.

125. Plaza A, Martinez P, Gualtieri JA, Perez R. Automated identification of endmembers from hyperspectral data using mathematical morphology. *Proc SPIE.* 2002;4541(1):278-287. http://link.aip.org/link/?PSI/4541/278/1.

126. Plaza A, Plaza J, Cristo A. Morphological feature extraction and spectral unmixing of hyperspectral images. *Signal Processing and Information Technology, 2008 ISSPIT 2008 IEEE International Symposium on.* 2008:12-17.

127. Plaza A, Plaza J, Sanchez S. Parallel implementation of endmember extraction algorithms using NVidia graphical processing units. *Geoscience and Remote Sensing Symposium,2009 IEEE International,IGARSS 2009.* 2009;5:V-208-V-211.

128. Su H, Sheng Y, Wen Y. Jointed endmember extraction algorithm and hyperspectral unmixing analysis. *Proc SPIE.* 2009. doi: 10.1117/12.833187.

129. Santos-García A, Vélez-Reyes M, Rosario-Torres S, Chinea JD. A comparison of unmixing algorithms for hyperspectral imagery. *Proc SPIE.* 2009. doi: 10.1117/12.819486.

130. Knight J, Voth M. Mapping impervious cover using multi-temporal MODIS NDVI data. *Selected Topics in Applied Earth Observations and Remote Sensing, IEEE Journal of.* 2011;4(2):303-309.

131. Thompson DR, Mandrake L, Gilmore MS, Castaño R. Superpixel endmember detection. *IEEE Trans Geosci Remote Sens.* 2010;48(11):4023-4033.

132. Sun L, Zhang Y, Guindon B. Improved iterative error analysis for endmember extraction from hyperspectral imagery. *Proc SPIE.* 2008;7086(1):70860S. http://link.aip.org/link/?PSI/7086/70860S/1.

133. Yuen PWT, Bishop GJ. Adaptive feature extraction techniques for subpixel target detections in hyperspectral remote sensing. *Proc SPIE.* 2004;5613(1):99-110. http://link.aip.org/link/?PSI/5613/99/1.

134. Chang C. Further results on relationship between spectral unmixing and subspace projection. *IEEE Trans Geosci Remote Sens.* 1998;36(3):1030-1032.

135. Chang CI, Du Q. Noise subspace projection approaches to determination of intrinsic dimensionality of hyperspectral imagery. *Proc SPIE.* 1999;3871(1):34-44. http://link.aip.org/link/?PSI/3871/34/1.

136. Chang C, Ren H. An experiment-based quantitative and comparative analysis of target detection and image classification algorithms for hyperspectral imagery. *IEEE Trans Geosci Remote Sens.* 2000;38(2):1044-1063.

137. Harsanyi JC, Chang C. Hyperspectral Image Classification and Dimensionality Reduction: An Orthogonal Subspace Projection Approach. *IEEE Trans Geosci Remote Sens.* 1994;32(4). 779-785.

138. Liu K, Wong E, Chang C. Kernel-based linear spectral mixture analysis for hyperspectral image classification. *Hyperspectral Image and Signal Processing: Evolution in Remote Sensing, 2009 WHISPERS '09 First Workshop on.* 2009:1-4.

139. Martin G, Plaza A. Spatial preprocessing for endmember extraction using unsupervised clustering and orthogonal subspace projection concepts. *Geoscience and Remote Sensing Symposium (IGARSS), 2010 IEEE International.* 2010:959-962.

140. Settle JJ. On the relationship between spectral unmixing and subspace projection. *IEEE Trans Geosci Remote Sens.* 1996;34(4):1045-1046.

141. Wei C, Xu-chu Y, He W. Estimate the number of endmembers for hyperspectral imagery. *Environmental Science and Information Application Technology, 2009 ESIAT 2009 International Conference on.* 2009;1:391-394.

142. Plaza A, Martin G, Zortea M. On the incorporation of spatial information to endmember extraction: Survey and algorithm comparison. *Hyperspectral Image and Signal*

Processing: Evolution in Remote Sensing, 2009 WHISPERS '09 First Workshop on. 2009:1-4.

143. Tung C, Tseng D, Tsai Y. Mixed-pixel classification for hyperspectral images based on multichannel singular spectrum analysis. *Geoscience and Remote Sensing Symposium, 2001 IGARSS '01 IEEE 2001 International.* 2001;5:2370-2372 vol.5.

144. Bovolo F, Bruzzone L, Carlin L. A novel technique for subpixel image classification based on support vector machine. *IEEE Trans Image Process.* 2010;19(11):2983-2999.

145. Sun Z, Guo H, Li X, Lu L, Du X. Estimating urban impervious surfaces from Landsat-5 TM imagery using multilayer perceptron neural network and support vector machine. *J Appl Remote Sens.* 2011;5.

146. Wang L, Jia X. Integration of soft and hard classifications using extended support vector machines. *Geoscience and Remote Sensing Letters, IEEE.* 2009;6(3):543-547.

147. Wang D, Zhou Y, Zheng J. Binary tree of posterior probability support vector machines for hyperspectral image classification. *J Appl Remote Sens.* 2011;5.

148. Yang C, Du Q, Everitt JH, Goolsby JA, Younan NH. Spectral unmixing of airborne hyperspectral imagery for mapping giant reed infestations. *Hyperspectral Image and Signal Processing: Evolution in Remote Sensing (WHISPERS), 2010 2nd Workshop on.* 2010:1-4.

149. Melgani F, Bruzzone L. Classification of hyperspectral remote sensing images with support vector machines. *IEEE Trans Geosci Remote Sens.* 2004;42(8). 1778-1790.

150. Brown M, Lewis HG, Gunn SR. Linear spectral mixture models and support vector machines for remote sensing. *IEEE Trans Geosci Remote Sens.* 2000;38(5). 2346-2360.

151. Hsu C, Chang CC, Lin CJ. A practical guide to support vector classification. (2003). http://www.csie.ntu.edu.tw/~cjlin/papers/guide/guide.pdf.

152. Ayuso F, Setoain J, Prieto M, et al. Endmember extraction from hyperspectral imagery using a parallel ensemble approach with consensus analysis. *Geoscience and Remote Sensing Symposium,2009 IEEE International,IGARSS 2009.* 2009;5:V-88-V-91.

153. Corucci L, Masini A, Cococcioni M. Approaching bathymetry estimation from high resolution multispectral satellite images using a neuro-fuzzy technique. *J Appl Remote Sens.* 2011;5.

154. Crespo JL, Duro RJ, Pena FL. Gaussian synapse ANNs in multi- and hyperspectral image data analysis. *IEEE Trans Instrum Meas*. 2003;52(3):724-732.

155. Crespo JL, Duro R, Pena FL. Unmixing low ratio endmembers through gaussian synapse ANNs in hyperspectral images. *Computational Intelligence for Measurement Systems and Applications, 2004 CIMSA 2004 IEEE International Conference on.* 2004:150-154.

156. Grana M, Sussner P, Ritter G. Associative morphological memories for endmember determination in spectral unmixing. *Fuzzy Systems, 2003 FUZZ '03 The 12th IEEE International Conference on.* 2003;2:1285-1290 vol.2.

157. Grana M, Gallego J. Associative morphological memories for endmember induction. *Geoscience and Remote Sensing Symposium, 2003 IGARSS '03 Proceedings 2003 IEEE International.* 2003;6:3757-3759 vol.6.

158. Pena FL, Crespo JL, Duro RJ. Unmixing low-ratio endmembers in hyperspectral images through gaussian synapse ANNs. *IEEE Trans Instrum Meas.* 2010;59(7):1834-1840.

159. Mianji FA, Ye Zhang, Yanfeng Gu. Resolution enhancement of hyperspectral images using a learning-based super-resolution mapping technique. *Geoscience and Remote Sensing Symposium,2009 IEEE International,IGARSS 2009.* 2009;3:III-813-III-816.

160. Burman JA. Hybrid pattern recognition method using evolutionary computing techniques applied to the exploitation of hyperspectral imagery and medical spectral data. *Proc SPIE.* 1999;3871(1):348-357. http://link.aip.org/link/?PSI/3871/348/1.

161. Chiang S, Chang C, Ginsberg IW. Unsupervised hyperspectral image analysis using independent component analysis. *Geoscience and Remote Sensing Symposium, 2000. Proceedings. IGARSS 2000. IEEE 2000 International.* 2000; 7.

162. Bayliss JD, Gualtieri JA, Cromp RF. Analyzing hyperspectral data with independent component analysis. *Proc SPIE.* 1998;3240(1):133-143. http://link.aip.org/link/?PSI/3240/133/1.

163. Nascimento JMP, Dias JMB. On independent component analysis applied to unmixing hyperspectral data. *Proc SPIE.* 2004;5238. doi:10.1117/12.510652.

164. Robila SA. Investigation of spectral screening techniques for independent-component-analysis-based hyperspectral image processing. *Proc SPIE.* 2003;5093(1):241-252. http://link.aip.org/link/?PSI/5093/241/1.

165. Xia W, Wang B, Zhang L. Constrained independent component analysis for hyperspectral unmixing. *Geoscience and Remote Sensing Symposium (IGARSS), 2010 IEEE International.* 2010:1293-1296.

166. Jia S, Qian Y. Improved Stone's complexity pursuit for hyperspectral imagery unmixing. *Pattern Recognition, 2006 ICPR 2006 18th International Conference on.* 2006;4:817-820.

167. Jia S, Qian Y. Spectral and spatial complexity-based hyperspectral unmixing. *IEEE Trans Geosci Remote Sens.* 2007;45(12):3867-3879.

168. Du H, Qi H, Wang X, Ramanath R, Snyder WE. Band selection using independent component analysis for hyperspectral image processing. *Applied Imagery Pattern Recognition Workshop, 2003 Proceedings 32nd.* 2003:93-98.

169. Du H, Qi H, Peterson GD. Parallel ICA and its hardware implementation in hyperspectral image analysis. *Proc SPIE.* 2004;5439(1):74-83. http://link.aip.org/link/?PSI/5439/74/1.

170. Robila SA. Considerations on unsupervised spectral data unmixing and complexity pursuit. *Geoscience and Remote Sensing Symposium (IGARSS), 2010 IEEE International.* 2010:987-990.

171. Dobigeon N, Tourneret J-. Spectral unmixing of hyperspectral images using a hierarchical bayesian model. *Acoustics, Speech and Signal Processing, 2007 ICASSP 2007 IEEE International Conference on.* 2007;3:III-1209-III-1212.

172. Dobigeon N, Tourneret J-, IlI AOH. Bayesian linear unmixing of hyperspectral images corrupted by colored gaussian noise with unknown covariance matrix. *Acoustics, Speech and Signal Processing, 2008 ICASSP 2008 IEEE International Conference on.* 2008:3433-3436.

173. Dobigeon N, Tourneret J-, Chein-I Chang. Semi-supervised linear spectral unmixing using a hierarchical bayesian model for hyperspectral imagery. *IEEE Trans Signal Process.* 2008;56(7):2684-2695.

174. Dobigeon N, Moussaoui S, Coulon M, Tourneret J-, Hero AO. Joint bayesian endmember extraction and linear unmixing for hyperspectral imagery. *IEEE Trans Signal Process*. 2009;57(11):4355-4368.

175. Eches O, Dobigeon N, Tourneret J-. An NCM-based bayesian algorithm for hyperspectral unmixing. Hyperspectral Image and Signal Processing: *Evolution in Remote Sensing, 2009 WHISPERS '09 First Workshop on.* 2009:1-4.

176. Eches O, Dobigeon N, Mailhes C, Tourneret J-. Bayesian estimation of linear mixtures using the normal compositional model. application to hyperspectral imagery. *IEEE Trans Image Process.* 2010;19(6):1403-1413.

177. Eches O, Dobigeon N, Tourneret J-. Estimating the number of endmembers in hyperspectral images using the normal compositional model and a hierarchical bayesian algorithm. *IEEE J Sel Top Signal Process*. 2010;4(3):582-591.

178. Halimi A, Altmann Y, Dobigeon N, Tourneret J-. Nonlinear unmixing of hyperspectral images using a generalized bilinear model. *IEEE Trans Geosci Remote Sens*. 2011;PP(99):1-10.

179. Eches O, Dobigeon N, Tourneret J-. A reversible-jump mcmc algorithm for estimating the number of endmembers in the normal compositional model application to the unmixing of hyperspectral images. *Acoustics Speech and Signal Processing (ICASSP), 2010 IEEE International Conference on.* 2010:1222-1225.

180. Eches O, Dobigeon N, Tourneret J-. Markov random fields for joint unmixing and segmentation of hyperspectral images. *Hyperspectral Image and Signal Processing: Evolution in Remote Sensing (WHISPERS), 2010 2nd Workshop on.* 2010:1-4.

181. Landgrebe D. Hyperspectral image data analysis. *IEEE Signal Process Mag*. 2002:17-28.

182. Stein DWJ. Stochastic compositional models applied to subpixel analysis of hyperspectral imagery. *Proc SPIE.* 2002;4480(1):49-56. http://link.aip.org/link/?PSI/4480/49/1.

183. Nascimento J, Bioucas-Dias JM. Learning dependent sources using mixtures of dirichlet: Applications on hyperspectral unmixing. *Hyperspectral Image and Signal Processing: Evolution in Remote Sensing, 2009 WHISPERS '09 First Workshop on.* 2009:1-5.

184. Urcid G, Valdiviezo-N. JC, Ritter GX. Endmember search techniques based on lattice auto-associative memories: A case on vegetation discrimination. *Proc SPIE.* 2009. doi: 10.1117/12.834213.

185. Cui J, Li X. Unsupervised hyperspectral unmixing based on constrained nonnegative matrix factorization and particle swarm optimization. *Intelligent Systems (GCIS), 2010 Second WRI Global Congress on.* 2010;3:376-380.

186. Huck A, Guillaume M. Estimation of the hyperspectral tucker ranks. *Acoustics, Speech and Signal Processing, 2009 ICASSP 2009 IEEE International Conference on.* 2009:1281-1284.

187. Huck A, Guillaume M, Blanc-Talon J. Minimum dispersion constrained nonnegative matrix factorization to unmix hyperspectral data. IEEE Trans Geosci Remote Sens. 2010;48(6):2590-2602.

188. Huck A, Guillaume M. Robust hyperspectral data unmixing with spatial and spectral regularized NMF. *Hyperspectral Image and Signal Processing: Evolution in Remote Sensing (WHISPERS), 2010 2nd Workshop on.* 2010:1-4.

189. Jia S, Ji Z, Qian Y. Band selection based hyperspectral unmixing. *Imaging Systems and Techniques, 2009 IST '09 IEEE International Workshop on.* 2009:303-306.

190. Miao L, Qi H. A constrained non-negative matrix factorization approach to unmix highly mixed hyperspectral data. *Image Processing, 2007 ICIP 2007 IEEE International Conference on.* 2007;2:II - 185-II - 188.

191. Montcuquet A-, Herve L, Guyon L, Dinten J-, Mars JI. Non-negative matrix factorization: A blind sources separation method to unmix fluorescence spectra. *Hyperspectral Image and Signal Processing: Evolution in Remote Sensing, 2009 WHISPERS '09 First Workshop on.* 2009:1-4.

192. Parente M, Zymnis A, Skaf J, Bishop J. Spectral unmixing with nonnegative matrix factorization. *Proc SPIE.* 2006;6366(1):63660B. http://link.aip.org/link/?PSI/6366/63660B/1.

193. Qian Y, Jia S, Zhou J, Robles-Kelly A. L1/2 sparsity constrained nonnegative matrix factorization for hyperspectral unmixing. *Digital Image Computing: Techniques and Applications (DICTA), 2010 International Conference on.* 2010:447-453.

194. Robila SA. Spectral image processing using sparse linear transforms. *Geoscience and Remote Sensing Symposium,2009 IEEE International,IGARSS 2009.* 2009;4:IV-534-IV-537.

195. Yang Z, Chen X, Zhou G, Xie S. Spectral unmixing using nonnegative matrix factorization with smoothed L0 norm constraint. *Proc SPIE.* 2009.

196. Yu Y, Guo S, Sun W. Minimum distance constrained non-negative matrix factorization for the endmember extraction of hyperspectral images. *Proc SPIE.* 2007;6790(1):679015. http://link.aip.org/link/?PSI/6790/679015/1.

197. Lennon M, Mercier G, Mouchot MC, Hubert-Moy L. Spectral unmixing of hyperspectral images with the independent component analysis and wavelet packets. *Geoscience and Remote Sensing Symposium, 2001 IGARSS '01 IEEE 2001 International.* 2001;6:2896-2898 vol.6.

198. Plaza A, Plaza J, Paz A. Improving the scalability of parallel algorithms for hyperspectral image analysis using adaptive message compression. *Geoscience and Remote Sensing Symposium,2009 IEEE International,IGARSS 2009.* 2009;4:IV-196-IV-199.

199. Scholl JF, Dereniak EL. Fast wavelet based feature extraction of spatial and spectral information from hyperspectral datacubes. *Proc SPIE.* 2004;5546(1):285-293. http://link.aip.org/link/?PSI/5546/285/1.

200. Scholl JF, Dereniak EL, Hege EK. Fast feature extraction in hyperspectral imagery via lifting wavelet transforms. *Proc SPIE.* 2005;5915(1):59150N. http://link.aip.org/link/?PSI/5915/59150N/1.

201. Pinzon JE, Ustin SL, Castaneda CM, Pierce JF, Costick LA. Robust spatial and spectral feature extraction for multispectral and hyperspectral imagery. *Proc SPIE.* 1998;3372(1):199-210. http://link.aip.org/link/?PSI/3372/199/1.

202. Scholl JF, Hege EK, Lloyd-Hart M, O'Connell D, Johnson WR, Dereniak EL. Evaluations of classification and spectral unmixing algorithms using ground based satellite imaging. *Proc SPIE.* 2006;6233(1):623328. http://link.aip.org/link/?PSI/6233/623328/1.

203. Bernacki BE, Phillips MC. Standoff hyperspectral imaging of explosives residues using broadly tunable external cavity quantum cascade laser illumination. *Proc SPIE.* 2010;7665(76650I). doi: 10.1117/12.849543.

204. Scholl JF, Hege EK, Hart M, O'Connell D, Dereniak EL. Flash hyperspectral imaging of non-stellar astronomical objects. *Proc SPIE.* 2008;7075(1):70750H. http://link.aip.org/link/?PSI/7075/70750H/1.

205. Chang C, Brumbley C. Kalman filtering approach to multispectral/hyperspectral image classification. *IEEE Trans Aerosp Electron Syst.* 1999;35(1):319-330.

206. Wang S, Chang C, Jensen JL, Jensen JO. Spectral abundance fraction estimation of materials using kalman filters. *Proc SPIE.* 2004;5584(1):210-220. http://link.aip.org/link/?PSI/5584/210/1.

207. Wang S, Chang CI, Jensen JL, Jensen JO. Kalman filter-based approaches to hyperspectral signature similarity and discrimination. *Proc SPIE.* 2006;6302(1):63020J. http://link.aip.org/link/?PSI/6302/63020J/1.

208. Wang S, Wang C, Chang M, Tsai CT, Chang CI. Applications of kalman filtering to single hyperspectral signature analysis. *IEEE Sens J*. 2010;10(3):547-563.

209. Broadwater J, Banerjee A. A generalized kernel for areal and intimate mixtures. *Hyperspectral Image and Signal Processing: Evolution in Remote Sensing (WHISPERS), 2010 2nd Workshop on.* 2010:1-4.

210. Zortea M, Plaza A. Spatial preprocessing for endmember extraction. *IEEE Trans Geosci Remote Sens.* 2009;47(8):2679-2693.

211. Martin G, Plaza A, Zortea M. Analysis of different strategies for incorporating spatial information in the design of endmember extraction algorithms from hyperspectral data. *Geoscience and Remote Sensing Symposium,2009 IEEE International,IGARSS 2009.* 2009;4:IV-877-IV-880.

212. Zortea M, Plaza A. Improved spectral unmixing of hyperspectral images using spatially homogeneous endmembers. *Signal Processing and Information Technology, 2008 ISSPIT 2008 IEEE International Symposium on.* 2008:258-263.

213. Zortea M, Plaza A. Spatial-spectral endmember extraction from remotely sensed hyperspectral images using the watershed transformation. *Geoscience and Remote Sensing Symposium (IGARSS), 2010 IEEE International.* 2010:963-966.

214. Plaza A, Plaza J. Impact of vector ordering strategies on morphological unmixing of remotely sensed hyperspectral images. *Pattern Recognition (ICPR), 2010 20th International Conference on.* 2010:4412-4415.

215. Rivard B, Rogge DM, Feng J, Zhang J. Spatial constraints on endmember extraction and optimization of per-pixel endmember sets for spectral unmixing. *Hyperspectral Image and Signal Processing: Evolution in Remote Sensing, 2009 WHISPERS '09 First Workshop on.* 2009:1-4.

216. Denney BS, de Figueiredo RJP. A new technique for hyperspectral image analysis with applications to anomaly detection. *Proc SPIE.* 2000;4132(1):49-60. http://link.aip.org/link/?PSI/4132/49/1.

217. Crist EP, Thelen BJ, Carrara DA. CHAMP: A locally adaptive unmixing-based hyperspectral anomaly detection algorithm. *Proc SPIE.* 1998;3438(1):66-73. http://link.aip.org/link/?PSI/3438/66/1.

218. Duran O, Petrou M. Anomaly detection using spectral unmixing with negative and superunity abundance weights. *Geoscience and Remote Sensing Symposium, 2007 IGARSS 2007 IEEE International.* 2007:4029-4032.

219. Duran O, Petrou M. Spectral unmixing with negative and superunity abundances for subpixel anomaly detection. *Geoscience and Remote Sensing Letters, IEEE.* 2009;6(1):152-156.

220. Gomez-Chova L, Amoros J, Camps-Valls G, et al. Cloud detection for CHRIS/Proba hyperspectral images. *Proc SPIE.* 2005;5979(1):59791Q. http://link.aip.org/link/?PSI/5979/59791Q/1.

221. Moya MM, Taylor JG, Stallard BR, Motomatsu SE. Anomaly detection using simulated MTI data cubes derived form HYDICE data. *Proc SPIE.* 1998;3438(1):355-366. http://link.aip.org/link/?PSI/3438/355/1.

222. Beaven SG, Hoff LE, Winter EM. Comparison of SEM and linear unmixing approaches for classification of spectral data. *Proc SPIE.* 1999;3753(1):300-307. http://link.aip.org/link/?PSI/3753/300/1.

223. Dolce PF, Cain SC. Three-dimensional LADAR range estimation using expectation maximization. *J Appl Remote Sens.* 2011.

224. Gonzalez D, Sanchez C, Veguilla R, Santiago NG, Rosario-Torres S, Velez-Reyes M. Abundance estimation algorithms using NVIDIA CUDA technology. *Proc SPIE.* 2008;6966(1):69661E. http://link.aip.org/link/?PSI/6966/69661E/1.

225. Xu Z, Zhao H. A new spectral unmixing algorithm based on spectral information divergence. *Proc SPIE.* 2008;7127(1):712726. http://link.aip.org/link/?PSI/7127/712726/1.

226. Yu X, Hoff LE, Beaven SG, Winter EM, Antoniades JA, Reed IS. Generalized linear feature detection of weak targets in spectrally mixed clutter. *Proc SPIE.* 1997;3163(1):108-116. http://link.aip.org/link/?PSI/3163/108/1.

227. Segl K, Roessner S, Heiden U. Differentiation of urban surfaces based on hyperspectral image data and a multi-technique approach. *Geoscience and Remote Sensing Symposium, 2000 Proceedings IGARSS 2000 IEEE 2000 International.* 2000;4:1600-1602 vol.4.

228. Francis RP. *DLP hyperspectral imaging for surgical and clinical utility*. Master's Thesis, University of Texas at Arlington. 2009.

229. Mangum ML. *A multimodality DLP imaging system for clinical surgery*. Master's Thesis, University of Texas at Arlington. 2011.

230. Thapa A. *Post-operative renal function analysis using visible DLP hyperspectral imaging system.* Master's thesis, University of Texas at Arlington. 2010.

231. Fong A, Bronson B, Wachman E. Advanced photonic tools for hyperspectral imaging in the life science. *SPIE Newsroom.* 2008. doi: 10.1117/2.1200803.1051.

232. Zuzak KJ, Francis R, Wehner E, et al. DLP hyperspectral imaging for surgical and clinical utility. *Proc SPIE*. 2009.

233. Zuzak KJ, Naik SC, Alexandrakis G, Hawkins D, Behbehani K, Livingston E. Characterization of a near-infrared laproscopic hyperspectral imaging system for minimally invasive surgery. *Anal Chem.* 2007;79: 4709-4715.

234. Zuzak KJ, Schaeberle MD, Lewis EN, Levin IW. Visible reflectance hyperspectral imaging: characterization of a noninvasive, in vivo system for determining tissue perfusion. *Anal Chem.* 2002;74, 2021-2028.

235. Richards JA, Jia X. *Remote Sensing Digital Image Analysis: An Introduction, 4th ed.* Springer, Germany.

236. vanVeen RLP, Sterenborg HJCM, Pifferi A, Torricelli A, Cubeddu R. Determination of VIS-NIR absorption coefficients of mammalian fat, with time- and spatially resolved diffuse reflectance and transmission spectroscopy. *J Biomed Opt.* 2005, 10(5).

237. Naik S. *Characterization of a novel, in vivo, laparoscopic hyperspectral imaging system for minimally invasive surgery*. Master's Thesis, University of Texas at Arlington. 2006.

238. Haglund O. *Qualitative comparison of normalization approaches in MALDI-MS.* Master's Thesis, Royal Institute of Technology KTH CSC, Stockholm, Sweden. 2008.

239. Meidunas EC. *Robust Estimation of Mahalanobis Distances in Hyperspectral Images.* Dissertation, Air Force Institute of Technology. 2006.

240. Park B, Lawrence C, Windham WR, Smith DP. Performance of supervised classification algorithms of hyperspectral imagery for identifying fecal and ingesta contaminants. *Transactions of the ASABE.* 2006;49(6):2017-2024.

241. Best SL, Thapa A, Jackson N, et al. Renal Oxygenation Measurement During Partial Nephrectomy Using Hyperspectral Imaging May Predict Acute Post-Operative Renal Function. *J Urol*. 2013;8:1037-40.

242. Best SL, Thapa A, Holzer MJ, et al. Minimal arterial in-flow protects renal oxygenation and function during porcine partial nephrectomy: confirmation by hyperspectral imaging. *J Urol.* 2011.

243. Olweny EO, Best SL, Jackson N, et al. A novel laparoscopic camera for characterization of renal ischemia using DLP® hyperspectral imaging; initial experience in a porcine model. *EUS*. 2011.

244. Samarov D, Wehner E, Schwarz R, Zuzak K, Livingston E. Hyperspectral image segmentation of the commong bile duct. *Proc SPIE.* 2013;8618.

245. McManamon PF. Review of ladar: a historic, yet emerging, sensor technology with rich phenomenology. *Opt Eng.* 2012;51(6). doi:10.1117/1.OE.51.6.060901.

246. Lötjönen J, Magnin IE, Reinhardt L, Nenonen J, Katila T. Automatic reconstruction of 3D geometry using projections and a geometric prior model. *Medical Image Computing and Computer-Assisted Intervention–MICCAI'99.* Springer Berlin Heidelberg, 1999.

247. Goodwin J. Special glasses help surgeons 'see' cancer. *Washington University in St. Louis Newsroom.* Feb 2014.

248. Lu G, Fei B. Medical hyperspectral imaging: a review. *J Biomed Opt*. 2014;19(1).

249. Bioucas-Dias JM, Nascimento JMP. Hyperspectral subspace identification. *IEEE Trans Geosci Remote Sens*. 2008;46(8):2435-2445.

250. Wu CC, Liu W, Chang CI. Exploration of methods for estimation of number of endmembers in hyperspectral imagery. *Proc SPIE.* 2006;6378(1):63781C. http://link.aip.org/link/?PSI/6378/63781C/1.

Biographical Information

Eleanor Wehner received her Bachelor's degree in Mechanical Engineering from Rose-Hulman Institute of Technology in Terre Haute, Indiana in 2005, where she also minored in German. She completed 44 credit hours of graduate coursework in Biomedical Engineering at Rose-Hulman before entering the PhD program in Biomedical Engineering on the Medical Imaging Track at the University of Texas at Arlington in 2007. Her research interests include hyperspectral imaging, spectral analysis, and medical imaging. She has worked on three different spectral ranges of DLP Hyperspectral Imaging (HSI) systems since starting graduate research work in the laboratory of Dr. Karel Zuzak. She continued her research under the mentorship of Dr. Edward Livingston, then Dr. Georgios Alexandrakis. She has co-authored many papers and conference proceedings with Dr. Jeffrey Cadeddu and other members of the UTSW Urology department regarding oxygenated blood perfusion for various states of renal blood vessel occlusion for both open and laparoscopic surgical procedures. Her primary research focus has been the differentiation of the common bile duct from its surrounding tissues using reflectance HSI.